Experimental investigation of drag reduction by polymer additives in a turbulent channel flow

by

Sadek M. Ali Shaban

A thesis submitted in partial fulfillment of the requirements for the degree of

Master of Science

Department of Mechanical Engineering
University of Alberta

Abstract

The addition of a minute amount of long-chain polymer molecules to a turbulent flow can cause a significant reduction of skin-friction drag in both internal and external flows. The explanation of interaction between polymers and turbulence remains the most difficult area of polymer flow phenomena, although a considerable research has been carried out in this field. Time-resolved, two-dimensional particle Image velocimetry (PIV) and three-dimensional particle tracking velocimetry (PTV) based on the "Shake-the-box" method are employed to investigate turbulent structures of Newtonian and non-Newtonian polymeric channel flow. Characterization of polymer effects on the turbulent flow and detailed rheological measurements, including shear viscosity, extensional viscosity and relaxation time, are carried out.

The Reynolds number of the current investigation is 20,000 based on channel height and properties of pure water. The experimental investigations of the polymer flow are carried out over various concentrations of polymer solution, including dilute polymer solutions and shear thinning polymer solutions. The maximum drag reduction, 'Virk's asymptote', is also obtained. In comparison to Newtonian fluid (water), the measurements showed a significant modification of the near-wall turbulence structure of the polymeric solutions: The viscous sublayer and buffer layer thickens; and the log-region is shifted upwards toward higher velocities while it remains essentially parallel to water in dilute polymer solutions. In the case of shear thinning polymers with drag reduction, the profiles in the log-layer are not only shifted upward, but also have a higher slope than that of water and dilute polymer solutions. With respect to the Reynolds stresses, a monotonic decrease is observed as a function of drag reduction. The

Reynolds shear stress is close to zero in shear thinning flows, especially at maximum drag reduction. The power spectral density (PSD) of streamwise and wall normal velocity fluctuations in the buffer and log-layer showed a reduction over all frequencies. The reduction in the energy intensity increases as drag reduction increases and the significant reduction is observed at high frequencies, implying large reduction in the small eddies. The quadrant analysis indicated a significant attenuation of ejection and sweep events compared with water flow, consistent with a large reduction in production of turbulence kinetic energy in polymeric flows.

Polymer dynamics in channel flow is investigated through the deformation tensor along the Lagrangian trajectories, which is used to identify the role of extensional viscosity within the flow. The results showed that the main contribution to the elongation deformation comes from streamwise strain rate fluctuations while a larger contribution is observed in the buffer layer. Resistance of molecules to strong elongational deformation results in a significant increase in extensional viscosity in the buffer layer. The PSD of the streamwise, wall-normal and shear strain rate fluctuations for polymeric flows from Lagrangian method are suppressed compared with water flow and the magnitude of reduction increases with increasing drag reduction. In addition, the reduction in energy intensity in streamwise and shear strain rate fluctuations are higher in the buffer layer while the reduction in energy intensity in wall-normal strain fluctuations is almost the same in the buffer and log layer.

Preface

This thesis contains experimental investigation on influence of drag-reducing polymers on turbulence structure in channel flow using two and three-dimensional measurement techniques.

In chapter 3, preparation of polymer solutions and pressure measurements were carried out by me. I carried out all the 2D and 3D PIV and PTV measurements reported in this thesis. The extensional viscosity measurements were carried out and provided to us by Madhar Azad (PhD student) at the Department of Civil and Environmental Engineering of the University of Alberta, under supervision of Prof. Japan Trivedi.

All of the experiments, data analysis and interpretation presented in chapters 4 are conceived by the author under supervision of Dr. Sina Ghaemi.

In Chapter 5 and Chapter 6, PIV and PTV processing and data analysis were conceived by author under the supervision of Dr. Sina Ghaemi. The interpretation and discussion of the results were also developed by author under supervision of Dr. Sina Ghaemi.

Acknowledgement

It is a pleasure to thank those who made this thesis possible. First and foremost, I wish to express my deepest gratitude to my Supervisor Dr. Sina Ghaemi for his guidance, advice and discussions who provided me with respect to the turbulent flow measurements and specifically in area of drag reduction are very much valued. I express my sincere gratitude to the Libyan Ministry of Higher Education and Scientific Research for giving me a full scholarship which enabled me to study in Canada.

Furthermore, I am indebted to my dear family for their continuous inspiration and endless support. Thanks given to my colleagues (Wagih Abu Rowin, Masoud Ebrahimian and Farzad Ahmadi) at University of Alberta for their help and support.

Table of Contents

List of Figures

List of Tables

Chapter 1. Introduction

The friction between a wall and a flowing turbulent fluid can result in loss of energy because of turbulent dissipation. Numerous techniques have been applied to reduce skin friction drag (SFD) in order to improve efficiencies of industrial operations. Reduction of skin-friction in turbulent flow can be achieved using active and passive techniques. Passive methods includes microbubbles (Deutsch *et al*., 2004), superhydrophobic surfaces (Rothstein, 2010), and riblets (Walsh & Lindemann 1984). The addition of polymers (Warholic *et al*., 1999), surfactants (Kawaguchi *et al*., 2002) and fibers (McComb & Chan, 1985) are also considered as a passive method.

The phenomenon of drag reduction by adding small quantities of certain long-chain polymers to the solvent in turbulent pipe flow was discovered by Toms in 1947. Polymer additives in turbulent flow can significantly affect the turbulent structures of the flowing fluid. These additives decrease the energy consumption and increase the flow rate. Although considerable effort has been directed to study the drag reduction effect of polymer solutions including theoretical, experimental and numerical approaches over last 60 years, there is still a lack of understanding of how the polymers dynamically interact with turbulence. The experimental investigations have been carried out by various measurement techniques over the last few decades. For instance, flow visualization by Donohue *et al.* (1972), measurement of instantaneous velocity using hot-wire anemometry (P. S. VlRK, 1975), and laser Doppler anemometer (Reischman & Tiederman, 1975; Wei & Willmarth, 1992; Warholic *et al.,* 1999; Ptasinski *et al*. 2001; Escudier *et al.,* 2009). The instantaneous velocity fields measured using two-dimensional particle image velocimetry (2D-PIV) were also carried out by Warholic *et al*. (2001), White *et al*. (2004) and Hou, Somandepalli & Mungal (2008). The most significant findings from experimental work, by Virk *et al*. (1967) and Virk (1971), are the existence of a maximum drag reduction (MDR) and the onset of drag reduction. The experimental study of Warholic *et al*. (1999) showed that there are significant differences in the statistics of turbulence in channel flow between water and polymer solutions, and their work confirmed the existence of polymer stress. Ptasinski *et al*. (2001) showed that the decrease of the Reynolds stress is

mainly compensated by an increase in the polymer stresses. Oldaker and Tiderman (1977) studied homogeneous polymer channel flow. Their work focused on the spatial structure of the viscous sublayer in channel flow. Although a large amount of data has been produced, there is still a lack of success in providing insight into the drag reduction mechanisms.

Direct numerical simulations (DNS) have been employed to enhance understanding of the physical mechanism in the previous literature. Min *et al.* (2003) preformed DNS with an Oldroyd-B model, which describes the elasticity of the polymer solution in a turbulent channel flow at maximum drag reduction. Sureshkumar, Beris & Handler (1997), Ptasinski *et al*. (2003) and Stone *et al*. (2004) used the FENE-P (finitely extensible nonlinear elastic–Peterlin) model. Kim *et al*. (2007) employed linear stochastic estimation (LSE) technique to DNS data to study the effects of polymer stresses. The Oldroyd-B and FENE-P models are based on a continuum approach (solving a constitutive equation) in an Eulerian frame (Sureshkumar *et al*.,1997; Min *et al*., 2001). In case of Oldroyd-B or FENE-P model, the polymer is described by adding the polymer stress to the stress tensor, which can be calculated at each grid cell (Terrapon *et al*., 2003). The Oldroyd-B model is severely limited because it suffers from failure of energy stability (Doering *et al*. 2006). The polymer stretching in the FENE-P model is bounded, whereas it does not have an upper-bound in the Oldroyd-B model (Min *et al.* 2003). Baron and Sibilla (1997) and Sibilla and Baron (2002) used a finite difference method and the FENE-P model. They showed that drag reduction occurs only when the relaxation time of polymers is comparable to the characteristic time scale of the turbulent flow. However, investigation of the interaction between polymer molecules and turbulent flow still relies on experimental techniques.

The thesis aims to experimentally investigate the role of extensional viscosity in the mechanism of drag reduction by polymer additives using rheological measurements and time-resolved particle-image velocimetry measurements in channel flow. In previous studies, there is an absence of detailed rheological measurements along with turbulence measurement. No experimental work is available on the effect of polymers on the field of spatial velocity derivatives (strain rate) in pipe or channel flow along with extensional viscosity measurements. The rate of strain is used to identify regions with elongational strain within the flow. The previous experimental studies of turbulence flows with drag reducing polymers have been

mainly limited to two velocity components (e.g., Warholic *et al.* 1999; Escudier *et al*. 2009). The unique feature of the data presented in this thesis is the inclusion of all components of Reynolds stresses using time-resolved three-dimensional particle tracking velocimetry based on the "Shake-the-box" method. The experimental investigations of the structure of near-wall turbulence in channel are carried out over low and high drag reduction regime. The data presented in this work can be used to help in formulating and evaluation of models to simulate polymer-turbulence interactions in viscoelastic turbulent channel flow.

The chapters of this thesis are organized as follows:

Chapter 2: It starts with introducing the basic concepts of turbulent channel flow. Several drag-reducing additives are introduced with focus on polymer. The last section presents the previous efforts including analytical, computational and experimental studies.

Chapter 3: This chapter details the experimental setup of the flow loop. The polymer perpetration and rheological measurements including shear and extensional viscosity are discussed. In addition, the experimental methodology and the setup including time-resolved planar PIV and time-resolved three-dimensional particle tracking velocimetry are described.

Chapter 4: The results of the pressure measurements are presented. These experiments aim to investigate the effect of polymer concentration on drag reduction and compare the degradation of the polymer solution as a result of operating two different pumps: progressive cavity type and a centrifugal pump.

Chapter 5: In this chapter, spatio-temporal structure of near-wall turbulence is investigated in Newtonian and non-Newtonian flows using time resolved 2D-PIV.

Chapter 6: Time resolved three-dimensional measurement of channel flow is performed. Performance of time-resolved 3D-PTV based on the shake-the-box technique is evaluated through comparison with a DNS reference data.

Chapter 7: Conclusions of the study and recommendations for future work are presented.

Chapter 2. Literature review

2.1 Turbulent channel flow

Turbulence is generated due to fixed walls or different velocities between adjacent fluid layers. The latter is known as free turbulence, where the turbulence is generated in the absence of a fixed wall such as turbulent jet. Turbulence generated in the presence of fixed wall is known as wall turbulence, which can be divided in two categories; external flows (boundary layer) and internal flows (pipes, ducts and channels).

2.1.1 Wall Shear Stress

In this section, some basics of turbulent channel flow are described in detail for Newtonian flow, mainly based on Pope (2000). The flow is considered incompressible. A rectangular channel with height H (= 2δ), width W and length L is illustrated in Figure 2.1. A Cartesian coordinate system is adopted such that x, y and z are the streamwise, wall-normal and spanwise directions, respectively. The bottom and top walls are located at $y = 0$ and $y = 2\delta$, respectively, with the mid-plane being $y=\delta$. It is assumed that length of the channel, L is long enough ($L / H >> 1$) to form a fully developed flow. Thus, the velocity profile is independent of the streamwise distance, x (fully developed flow) with large aspect ratio ($W / H >> 1$) so the flow is statistically independent of the spanwise coordinate.

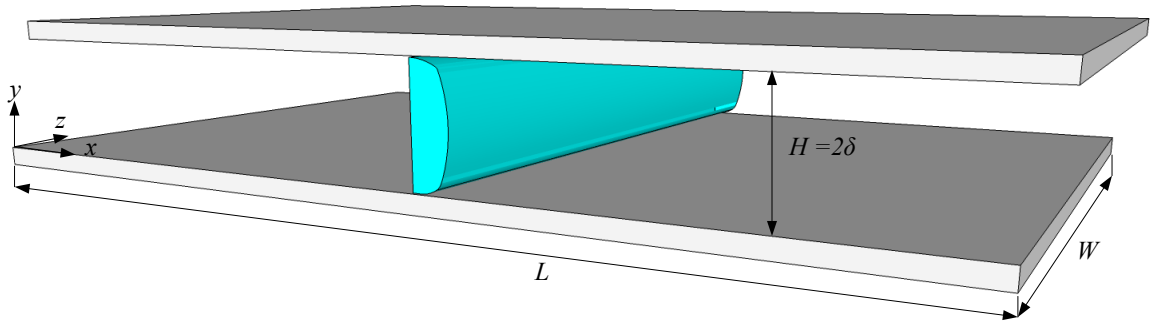

Figure 2.1. Configuration of the turbulent channel flow showing mean velocity profile, the coordinate system, and the main dimensions.

The components of instantaneous velocity vector $\boldsymbol{U}$ are defined as U (streamwise), V (wall-normal) and W (spanwise) and u,v and w denote their fluctuating values. This instantaneous velocity can be written using Reynolds decomposition as

$$u = U - \langle U \rangle, \tag{2.1}$$

where the angled brackets $\langle\ \rangle$ indicate an ensemble average of the quantity within. The Reynolds number of the Newtonian channel flow is defined based on the full channel height H and the bulk velocity U_b across the channel as

$$Re = \frac{\rho U_b H}{\mu^{(s)}}, \tag{2.2}$$

where ρ is the density and $\mu^{(s)}$ is the dynamic viscosity of the solvent (Newtonian flow).

The conservation of mass (continuity equation) is:

$$\frac{\partial \rho}{\partial t} + \frac{\partial U_i}{\partial x_i} = 0, \tag{2.3}$$

where t is the time and i denote the Cartesian coordinates. When the flow is steady and incompressible, the mean continuity equation can be written as

$$\frac{\partial \langle U \rangle}{\partial x} + \frac{\partial \langle V \rangle}{\partial y} + \frac{\partial \langle W \rangle}{\partial z} = 0. \tag{2.4}$$

As mentioned above, $\langle U \rangle$ is statistically independent of the streamwise direction and $\langle W \rangle = 0$. The mean continuity equation reduces to

$$\frac{\partial \langle V \rangle}{\partial y} = \text{constant}. \tag{2.5}$$

Applying the boundary condition $\langle V \rangle = 0$ at $y = 0$ which means that the average velocity has only a component in streamwise direction i.e., $\boldsymbol{U} = (\langle U \rangle_y , 0, 0)$.

$$\frac{\partial \langle V \rangle}{\partial y} = 0 \tag{2.6}$$

The streamwise momentum equation is:

$$\rho\left(\frac{\partial \langle U\rangle}{\partial t} + \langle U\rangle\frac{\partial \langle U\rangle}{\partial x} + \langle V\rangle\frac{\partial \langle U\rangle}{\partial y} + \langle W\rangle\frac{\partial \langle U\rangle}{\partial z}\right)$$
$$= -\frac{\partial \langle P\rangle}{\partial x} - \rho\frac{\partial \langle u^2\rangle}{\partial x} - \rho\frac{\partial \langle uv\rangle}{\partial y} - \rho\frac{\partial \langle uw\rangle}{\partial z} + \mu^{(s)}\left(\frac{\partial^2 \langle U\rangle}{\partial x^2} + \frac{\partial^2 \langle U\rangle}{\partial y^2} + \frac{\partial^2 \langle U\rangle}{\partial z^2}\right). \quad (2.7)$$

The wall-normal momentum equation is

$$\rho\left(\frac{\partial \langle V\rangle}{\partial t} + \langle U\rangle\frac{\partial \langle V\rangle}{\partial x} + \langle V\rangle\frac{\partial \langle V\rangle}{\partial y} + \langle W\rangle\frac{\partial \langle V\rangle}{\partial z}\right)$$
$$= -\frac{\partial \langle P\rangle}{\partial y} - \rho\frac{\partial \langle uv\rangle}{\partial x} - \rho\frac{\partial \langle v^2\rangle}{\partial y} - \rho\frac{\partial \langle vw\rangle}{\partial z} + \mu^{(s)}\left(\frac{\partial^2 \langle V\rangle}{\partial x^2} + \frac{\partial^2 \langle V\rangle}{\partial y^2} + \frac{\partial^2 \langle V\rangle}{\partial z^2}\right), \quad (2.8)$$

where P is the local pressure and $\langle uv\rangle$ is Reynolds shear stress. For simplifications of the momentum equation, flow is steady and all the components and gradients are independent of streamwise distance, x, except the pressure gradient in the streamwise direction which drives the flow through the channel. The flow is considered two-dimensional i.e., all gradients and mean velocity in spanwise are negligible. Therefore, equation (2.7 and 2.8) reduce to

$$-\frac{\partial \langle P\rangle}{\partial x} - \rho\frac{\partial \langle uv\rangle}{\partial y} + \mu^{(s)}\frac{\partial^2 \langle U\rangle}{\partial y^2} = 0, \text{ and} \quad (2.9)$$

$$-\rho\frac{\partial \langle v^2\rangle}{\partial y} - \frac{\partial \langle P\rangle}{\partial y} = 0. \quad (2.10)$$

Integrating last equation with respect to y with the boundary condition of $\langle v^2\rangle_{y=0} = 0$ yields

$$\langle v^2\rangle + \frac{\langle P\rangle}{\rho} = \frac{P_w(x)}{\rho}, \quad (2.11)$$

where P_w is the mean pressure at the channel wall, which can be written as

$$P_w = \langle P\rangle + \rho\langle v^2\rangle. \quad (2.12)$$

$$\frac{\partial \langle P\rangle}{\partial x} = \frac{dP_w}{dx}, \quad (2.13)$$

where $P_w = \langle P(x,0,0)\rangle$ and $\langle v^2\rangle$ is independent of x.

The equation (2.9) can be integrated along the y direction

$$- y\frac{\partial <P>}{\partial x} + \text{constant} = \rho <uv> - \mu^{(s)}\frac{\partial <U>}{\partial y} . \tag{2.14}$$

The first boundary condition for this flow is Reynolds shear stress $<uv> = 0$ and velocity gradient $\partial <U> / \partial y = 0$ at the center of the channel ($y = H/2 = \delta$). Therefore, the equation (2.14) evaluates as

$$-\frac{H}{2}\frac{\partial <P>}{\rho\, \partial x} = \text{constant}. \tag{2.15}$$

For the second boundary condition, turbulent velocity fluctuations must be zero at wall (to satisfy the no-slip condition) i.e., the Reynolds shear stress is zero. As a results, the equation (2.14) can be rewritten as

$$\mu^{(s)}\frac{\partial <U>}{\partial y} = \text{constant}. \tag{2.16}$$

The constant in equation (2.15) and (2.16) is the wall shear stress, τ_w. This indicates that there is a balance between the wall shear stress and pressure force acting on the fluid. As a result, the wall shear stress can be calculated in terms of measurement of pressure gradient along the channel.

$$\tau_w = - \frac{H}{2}\left(\frac{dP}{dx}\right). \tag{2.17}$$

Where the total shear stress for Newtonian flow ($\tau^{(s)}$) is

$$\tau^{(s)} = \mu^{(s)}\frac{d<U>}{dy} - \rho <uv>. \tag{2.18}$$

In a wall bounded turbulent shear flow in the vicinity of the wall, the important parameters that promote viscous characteristic are the viscosity and the wall shear stress. From these quantities, the inner scales (viscous scales) can be defined. The friction velocity (wall velocity scale) is

$$u_\tau = \sqrt{\frac{\tau_w}{\rho}} , \tag{2.19}$$

and the viscous length scale or wall unit is defined as

$$\delta_v = \nu\sqrt{\frac{\rho}{\tau_w}} = \frac{\nu}{u_\tau}, \tag{2.20}$$

where $v = \mu / \rho$ is kinematic viscosity.

The Reynolds number that characterizes the flow based inner scales is called the friction Reynolds number and is defined by

$$Re_\tau = \frac{u_\tau \delta}{v}. \tag{2.21}$$

The dimensionless wall-normal axis and velocity based on the inner scales for the distance from the wall and velocity can be denoted by

$$y^+ = \frac{y}{\delta_v} \text{ and} \tag{2.22}$$

$$u^+ = \frac{<U>}{u_\tau}, \tag{2.23}$$

In case of a non-Newtonian fluid (polymer solution), the shear viscosity does not remain constant. It decreases with increasing shear rate. Therefore, Reynolds number is defined based on the dynamic viscosity of polymeric flow ($\mu_w^{(p)}$) at the wall (Pinho and Whitelaw, 1990; Draad *et al.*, 1998; Ptasinski *et al*., 2001; Ptasinski *et al*. 2003).

$$Re_w = \frac{\rho U_b H}{\mu_w^{(p)}}, \tag{2.24}$$

The experimental studies by Gyr & Tsinober (1997), den Toonder *et al*. (1997) and Warholic *et al*. (1999) confirmed the existence of a polymeric stress (stress deficit) in polymer drag-reducing flow. Gyr & Tsinober (1997) and Warholic *et al*. (1999) found that the total shear stress in a fully developed two-dimensional channel flow is

$$\tau_{total} > \mu_s \frac{d<U>}{dy} - \rho<uv> \tag{2.25}$$

The total stress in polymeric flow is decomposed in a Newtonian part due to the solvent and a polymeric part (non-Newtonian). The total shear stress is then given as

$$\tau_{total} = \tau^{(s)} + \tau^{(p)} = \mu_s \frac{d<U>}{dy} - \rho<uv> + \tau^{(p)}, \tag{2.26}$$

where $\tau^{(p)}$ is the mean polymeric stress. Experimentally, it is found that mean polymeric stress is zero at the wall (Warholic *et al*., 1999; Ptasinski *et al*. 2001).

2.1.2 Mean velocity profile

The profile of turbulent boundary layer can be divided based on y^+ into different layers in the near-wall flow (Pope, 2000). The region $y^+ < 50$ is called viscous wall region where molecular viscosity significantly affects the shear stress. In the outer layer $y^+ > 50$, the effect of molecular viscosity is negligible. The velocity gradient $d\langle U\rangle/dy$ is considered a significant quantity. For instance, turbulent production and viscous stress are associated with a particular velocity gradient. The mean velocity gradient can be expressed in terms of two non-dimensional parameters, which are length scale in the viscous sublayer and outer layer. Hence,

$$\frac{d\langle U\rangle}{dy} = \frac{u_\tau}{y} F(\frac{y}{\delta_v}, \frac{y}{\delta}), \tag{2.27}$$

where F is a universal non-dimensional function.

The near wall region ($y / \delta < 0.1$) at high Reynolds numbers is called the inner layer. In this region, the mean velocity profile is dependent on viscous scales, therefore

$$\frac{d\langle U\rangle}{dy} = \frac{u_\tau}{y} F^*(\frac{y}{\delta_v}). \tag{2.28}$$

where F^* is applied instead of F because viscous scale dominates in this region. This function is described as

$$F^*(\frac{y}{\delta_v}) = \lim_{y/\delta \to 0} F(\frac{y}{\delta_v}, \frac{y}{\delta}). \tag{2.29}$$

With dimensionless units y^+ and u^+, equation 2.28 can be rewritten as

$$\frac{du^+}{dy^+} = \frac{1}{y^+} F^*(y^+). \tag{2.30}$$

Its integral leads to

$$u^+ = f_w(y^+), \tag{2.31}$$

which is known as the law of the wall that states that u^+ is dependent exclusively on y^+ and the function f_w is universal for pipe channel flow and boundary layer.

No-slip condition $\langle U\rangle = 0$ is used at the wall (y=0), therefore,

$$f_w(0) = 0. \tag{2.32}$$

And $f'_w = (du^+/dy^+) = 1$ can be obtained from wall shear stress equation as follows:

$$\tau_w = \rho\nu \left(\frac{d<U>}{dy}\right)|_{y=0} = \rho u_\tau^2, \text{thus} \tag{2.33}$$

$$\frac{d<U>/u_\tau}{u_\tau dy/\nu} = \frac{du^+}{dy^+} = 1. \tag{2.34}$$

The linear relation between the velocity profile and distance from the wall persists in a certain region in the vicinity of the wall which is called the viscous sublayer ($y^+<5$). The effect of viscosity decreases away from the wall. When δ_v is too small to control the dynamics of flow and δ is too large, this leads to

$$F^{**}\left(\frac{y}{\delta}\right) = \lim_{y/\delta_v \to 0} F\left(\frac{y}{\delta_v}, \frac{y}{\delta}\right) = \frac{1}{\kappa}. \tag{2.35}$$

Therefore,

$$\frac{d<U>}{dy} = \frac{u_\tau}{y} F^{**}\left(\frac{y}{\delta}\right) = \frac{u_\tau}{y}\frac{1}{\kappa}, \tag{2.36}$$

where κ is the von Karman constant which describes the exponent of the velocity profile.

Thus, the mean velocity gradient can be written based on dimensionless parameters as

$$\frac{du^+}{dy^+} = \frac{1}{\kappa y^+}. \tag{2.37}$$

Integration of equation 2.37 gives the logarithmic or von Karman law

$$u^+ = \frac{1}{\kappa} \ln y^+ + B, \tag{2.38}$$

where B is a constant. The variation of constants, B=5.2 and κ =0.41 are within 5% (Pope, 2000). This equation is applied to the log-law region in range of $y / \delta < 0.3$ and $y^+ > 30$. The transitional region is known as buffer layer which is between the viscous sublayer and the log-law region, i.e., $5< y^+ < 30$. The buffer layer is where the peak production and dissipation of turbulent kinetic energy occurs.

2.2 Drag reducing additives

Drag reduction additives can be classified into three major types, namely polymers, surfactants and fibers. These additives are discussed separately in this section. Surfactant additives are classified based on the electrical charge of the head group into anionic, cationic and nonionic. The drag reducing effectiveness of surfactant solution depends on the shape of micelles. Above a critical value of concentration, the surfactant molecules start to form aggregates which are micelles. However, formation of micelles is a reversible process, i.e., when the concentration fall below the critical value, micelles break up into molecules again. Anionic surfactants are relatively inexpensive, but can precipitate out by interaction with calcium, which reduces their effectiveness. Meanwhile, cationic surfactants have an advantage over anionic because they do not precipitate in the presence of calcium. Their drawbacks, on the other hand, are chemical degradation in aqueous solutions within a few days and expense. Due to their thermal instability, their practical use in industrial application is limited. The non-ionic surfactants have mechanical, chemical and thermal stability, which are not available together in cationic or anionic surfactants. Another advantage of non-ionic surfactants is that they do not precipitate in the presence of calcium ions in solution (Truong, 2001). The main feature of surfactant drag reducing additives is that they have an ability to self-repair after mechanical degradation. This gives them an advantage over polymers (Qi and Zakin, 2002). However, the major drawbacks of surfactants is their negative impact on the environment (Tamano *et al.,* 2014) and their need for much higher concentrations in order to achieve the same drag reduction that is achievable with small concentration of polymer.

The drag reduction by adding wood pulp fiber suspensions in turbulent pipe flow was first observed by Forrest and Grierson (1931). Mewis and Metzner (1974) found that fibers have high resistance to extensional deformations. In a later work, Kale and Metzner (1976) reported that drag reduction could be due to an interaction between viscous eddies and fibers in the region close to pipe wall. On the contrary, Lee and Duffy (1976) suggested that this interaction occurs in the core region. Radin *et al*., (1975) investigated different parameters including fiber concentration on drag reduction in dilute solid-liquid suspension. Their results showed that drag reduction increases with increasing concentration. The effectiveness of fibers increases with increasing their aspect ratio (Lee and Duffy, 1976). One major advantage of fiber over polymer

is that fibers have high resistance to mechanical degradation (Roy & Larson, 2005). However, the drawbacks of using fibers are that they can cause plugging problems in pipelines because of the high concentration of fibers required for drag reduction (Wang *et al*., 2011) and they are not as effective as polymer solutions. Among other fibers (Nylon, wood pulp) used in drag reduction, asbestos showed high drag reduction (Ellis 1970). However, this kind of fiber is not commercially used because asbestos fibers are hazardous to human health. The mixtures of fiber systems and polymers shows higher level of drag reduction than that of polymers or fibers alone (Lee *et al*., 1974; Kale & Metzner, 1974).

Drag reducing polymers can be classified based on the source of polymer i.e., synthetic (extracted from petroleum oil) or natural. Polymers can also be classified based on their structure. A polymer is simply a large molecule build up from many smaller units known as monomers or repeating units. A linear polymer consists of long chain of monomers. Polyethylene oxide is an example of a linear polymer. A branched polymer has a treelike structure where branches covalently attached to the main chain. These branches could be further branched but the secondary branches are not connected to any other existing branches such as polysaccharide. Cross-linked polymers, sometimes called network polymers have different chains are connected. i.e., monomers of one chain are covalently bonded with monomers of another chain. This structure results in a three-dimensional network (Bahadur & Sastry, 2005; Soldati & Monti, 2014). These three polymer structures are shown in Figure 2.2. Polymers can also classified based on their charge as anionic, non-ionic, and cationic.

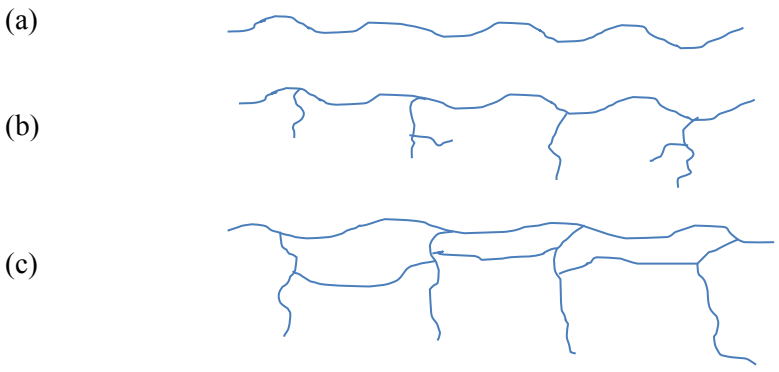

Figure 2.2. A schematic of (a) linear, (b) branched, and (c) cross-linked polymers. (Adapted from Bahadur & Sastry ,2005).

Drag reduction (DR) with polymer additives are classified into two categories based on their molecular structure: rigid and flexible polymers (Japper-Jaafar *et al*., 2009). The most common water-soluble polymer as drag reducers based on previous studies on polymer drag reduction, are polyacrylamide (PAM) and polyethylene oxide (PEO), xanthan gum (XG), guar gum (GM), and carboxymethyl cellulose (CMC). PAM and PEO and are categorized as flexible polymers and XG, GM and CMC as rigid polymers.

The chains in rigid rod polymers are always a fully extended conformation as shown in Figure 2.3 (a). The level of flexibility is negligible in rigid rod polymers (Gillissen, 2008). Pereira *et al*. (2013) showed that the relaxation time of (Xanthan gum) rigid polymers are small compared with the flexible polymers. Relaxation time is the time required to relax back to an equilibrium configuration after applying shear stress to extend chains. On the other hand, chains in flexible polymer are coiled at the rest, then start to uncoil gradually by the shear flow (Andrade *et al*., 2016), as shown in Figure 2.3 (b). The results of Japper *et al*. (2009) showed that flexible polymers typically yield a higher DR compared to rigid rod polymers. The polymer degradation is considered the main drawback in the industrial application and study of drag reduction because effectiveness of polymer drag reducer decreases with increasing degradation. The polymer degradation can be classified in to chemical and mechanical degradation (Toonder *et al*., 1995).

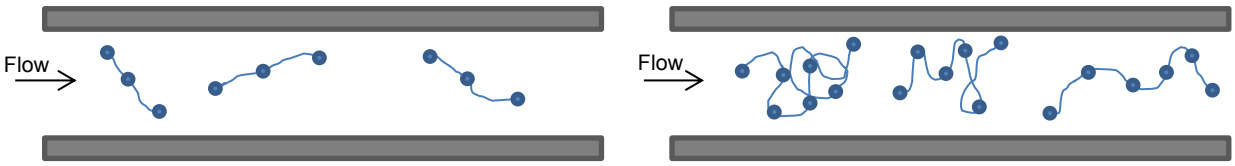

(a) Rigid polymer (b) Flexible polymer

Figure 2.3. Schematic of the effect of shear stress with time on rigid and flexible polymer without considering the degradation effect.

Chemical degradation

The polymer structure is changed by chemical reactions; it can occur for instance by the presence of certain metals or metal ions but there is limited understanding of the exact mechanism of chemical degradation (Shupe, 1981). Additionally, polymers may degrade when dissolved oxygen is present, but also this issue is still not clear because there is evidence of negligible degradation for solutions up to one-week-old (McComb *et al*., 1982). However, Shupe (1981) reported that removal of oxygen from the polyacrylamide solution can reduce chemical degradation because oxygen reacts with other substances (formaldehyde, glutaraldehyde and metals). Martin (1986) found that degradation of polymer increases when the salinities or calcium concentration of the solvent is high

Mechanical degradation

When polymers chains are subject to high shear rate, the chains are broken down into shorter segments. This leads to a decrease in polymer molecular weight, and thus a considerable decrease in drag-reducing effectiveness. High mechanical degradation mainly occurs during pumping, mixing and sharp turns in flow loop. The theoretical work of Bueche (1960) showed that polymer molecules in shear flow are subject to stretching due to strain rates and rotation due to vorticity. Lumley (1973) theoretically investigated the interaction between polymer molecules and a flow field, finding that if the vorticity is small and strain rate is too large, the molecules will expanded significantly.

2.3 Mechanism of Drag Reduction

2.3.1 Analytical and computational studies

The mechanism of interaction between polymer molecules and turbulent flow causing drag reduction is not completely understood, although the phenomena of polymer drag reduction has been reported by Tomas since 1949. Various plausible mechanisms have been suggested in the literature. The most common theories are proposed by Lumley (1973) and de Gennes (1986).

Lumley's theory is among the first theories explaining the mechanism of polymer drag reduction, based on molecular extension (Lumley 1969, 1973). Lumley theoretically showed that polymer molecules can be considerably extended where the vorticity is small and random fluctuation of the strain rate is large. Stretching of polymer molecules in certain regions of turbulent flow causes an increase in viscosity locally (extensional viscosity). Lumley postulated that viscosity in the viscous sublayer is unaffected due to absence of high fluctuation of the strain rate. Further away from the viscous sublayer, in the buffer layer where there are high strain rate fluctuations, extensional viscosity (elongational viscosity) increases significantly. Therefore, the small eddies are suppressed and the thickness of the buffer layer increases. This leads to reduce the velocity gradient at the wall, thus reducing the wall shear stress. Metzner and Metzner (1970) showed that extensional viscosity of Newtonian fluid is three times higher than their shear viscosity. In case of several concentrated polymer solutions, they found that extensional viscosity is 270 to 1730 times larger than the shear viscosity.

Additionally, Lumley explained a threshold limit of the mechanism associated with onset phenomenon in his theory by defining time scale ratio of the eddies to the relaxation time of the polymer molecules. The onset of drag reduction occurs when the polymer relaxation time is longer than the time scale of turbulence near the wall. Lumley (1969) also stated that the size of the polymer molecules is several orders of magnitude smaller than the smallest turbulence scale at the onset of drag reduction. This is contrary to Virk's theory (1967), which defined the onset of drag reduction based on the ratio of turbulence length scale and polymer length scale. When the ratio of length scale reaches a critical value, the onset of drag reduction occurs. Hinch (1977) supported Lumely's theory using elongation models and concluded that random-coil

molecules are stretched significantly when they are subject to high strain rate, which leads to an increase of extensional viscosity.

Ryskin (1987) proposed a yo-yo model based on modifying Lumley's theory. Based on this model, the polymer chain unravels when strain rate exceeds a critical value in extensional flow. If the flow becomes weaker, the polymer chain will curl back into the coiled conformation. During the unraveling chain process, the central part is elongated first which generates large additional stresses. Ryskin also formulated an expression for effective viscosity (extensional viscosity) as a function of the highest extensibility of a polymer and the polymer concentration and concluded that effective viscosity increase as a result of polymer stretching in a turbulent flow.

Landahl (1973, 1977) developed a two-scale mechanistic model of turbulence based on the classical hydrodynamic stability applied to the turbulent boundary layer. Landahl proposed that turbulence near the wall consists of a coupled motion at two disparate scales. The small scale is instable due to shearing of the large scale eddies by the mean flow. The drag reduction occurs due to aligned elongated polymer molecules stabilizing the small scale and causing anisotropic stress, reducing turbulent production. Den Toonder *et al* (1997) and Orlandi (1995) investigated this theory by means of direct numerical simulation (DNS). Den Toonder *et al*. (1997) used two different models and laser Doppler velocimetry (LDV). The first model was based on viscous anisotropic effects of elongated molecules. The second model was an extension of the first model based on the Maxwell model (elastic component). The results of viscous anisotropic polymer model showed relative accuracy with LDV measurements and higher drag reduction than the viscoelastic model. Thus, the authors suggested that viscous anisotropic stresses have the main role in the mechanism of drag reduction.

Tabor and de Gennes (1986) proposed a theory, based on the elastic properties of the dissolved polymers, known as elastic theory. Tabor & de Gennes (1986) and de Gennes (1990) thought that random fluctuations of strain rate in turbulent flow is insufficient to significantly increase the extensional viscosity. They argued that even dilute polymer solution in turbulent flow can exhibit elastic properties even at high frequencies (small scales). In de Gennes (1990) model, coil chains of polymer in solvent behave like elastic springs. De Gennes postulated that polymer molecules absorb some of turbulent energy cascade as elastic energy. When the elastic

energy and the turbulent kinetic energy are comparable, turbulence is suppressed at certain length scale resulting in drag reduction. Sreenivasan & White (2000) elaborated on elastic theory to explain the onset of maximum drag reduction. Rabin & Zielinska (1989) theoretically investigated the effect of polymer molecules on the vortices distribution in elongational flow. They showed that elastic energy storage by polymer molecules can enhance vorticity at large scale and, thereby inhibiting the energy cascade toward the dissipative scales.

2.3.2 Experimental studies

Most of the experiments in polymer drag-reduced flows reported before 1970 have been carried out using Pitot tubes, hot film anemometers, or wire film anemometers. Virk *et al* (1967) used pitot tubes to measure mean velocity profiles and they used hot-wire anemometry to obtain velocity fluctuations of the turbulent field and the energy spectrum. These measurement techniques have subsequently been shown to be inaccurate in polymer flows. Measurement of velocity of the flow field in polymer solutions using Pitot tubes, hot film anemometers or wire film anemometers can be in error (Walker and Tiederman, 1990). The disadvantage of using hot film is that polymer molecules wrap around the sensors of hot-film, which can have direct influence on heat transfer as well as single-point measurement (Wei & Willmarth, 1992). The effect of wrapping polymer molecules around the hot film sensor is more pronounced at a high concentration and especially in non-homogeneous polymer solutions.

Laser Doppler anemometry (LDA) or laser Doppler velocimetry (LDV) has a fundamental advantage over pitot and hot-film probes since there is no physical interaction with the flow. However, LDV also measures the velocity only at a single point. In order to obtain a large area of flow field, measurements must be repeated at different points throughout the flow field. LDV has been reported in many studies of polymer drag reduced flow in the literature. The early LDV measurements were carried out by Rudd (1972), Chung and Graebel (1972), and Logan (1972) in pipes. In the following years, studies by Mizushina & Usui (1977), Sá Pereira and Pinho (1994), Den Toonder *et al*. (1997), Ptasinski *et al* (2001), and Japper-Jaafar *et al* (2009) were carried in pipes as well as in channel flows (Reischman & Tiederman 1975, Willmarth *et al*. 1987, Luchik & Tiederman 1988, Walker & Tiederman 1990, Harder & Tiederman 1991, Wei and Willmarth 1992, Gyr and Tsinober 1997, Warholic *et al*. 1999, Escudier and Smith 2001, and Escudier *et al*. 2009).

To overcome the limitation in simultaneous measurement of velocity over a larger field, particle image velocimetry (PIV) was used. PIV has become the most effective and progressive measurement tool because fluid velocities can be simultaneously measured at multiple points in a plane. Measurements using 2D-PIV are reported by Warholic *et al* (2001) in a channel flow, and by Somandepalli *et al.* (2003) and White *et al.* (2004) in flat-plate boundary layer. Besides PIV, flow visualization techniques were also used to investigate the structure of polymer drag-reducetion. Flow visualization studies of drag reduction by polymer solution were carried out by Donohue *et al.* (1972), Gyr (1976), Achia & Thompson (1977), Oldaker & Tiederman (1977), McComb & Rabie (1982), Tiederman *et al*. (1985), and Walker *et al.* (1986).

Numerous experimental investigations over the years have confirmed the effect of drag reduction in turbulent flows by polymers since the discovery of drag reducing polymers in 1948 by Toms. One of the earliest comprehensive and exhaustive experimental investigations was carried out by Virk *et al*. (1967) in turbulent pipe flow of dilute polymer solutions. They used hot-film and Pitot tubes to measure the streamwise velocity. The remarkable features of their work are that an onset for drag reduction occurs at a well defined wall shear stress, and the existence of a universal maximum drag reduction (MDR) asymptote, known as *Virk's asymptote*. In a subsequent work, Virk (1975) showed that mean velocity profile is significantly modified by addition of polymer and the onset of drag reduction does not depend on polymer concentration or pipe diameter. Reischman & Tiederman (1975) carried out an investigation using single-component LDV measurements in a fully developed turbulent channel. The results of this experimental study showed that thickness of viscous sublayer does not change, the thickness of the buffer layer increased in normalized mean velocity profile and the logarithmic profile of the mean velocity is shifted upwards. However, studies of Rudd (1972) in pipe flow with LDV measurements and Escudier *et al*. (2009) in channel flow with LDV measurements showed a thicker viscous sublayer.

Recent experiments in pipe flow were performed by Ptasinski *et al.* (2001) and Japper-Jaafar *et al.* (2009), who used LDV to measure turbulence statistics in a two dimensional and a three dimensional flow, respectively. According to the study performed by Ptasinski *et al*., who used Superfloc A110 (flexible polymer), the peak values of streamwise Reynolds stress at low concentration increased to levels higher than that for water. However, the peaks decreased to

levels present in the water flow at high concentrations. The peak location shifted towards the center of the pipe. Radial Reynolds stress decreased with increasing polymer concentration. The Reynolds stress profiles were normalized with the friction velocity of the polymer. They also observed that Reynolds stress significantly decreases at high polymer concentrations, but it remains non-zero. Their results also indicate that a significant contribution to the total shear stress comes from polymer stress at high concentrations, and the polymer stress increases with increasing distance from the wall. Polymer stress "shear deficits" is in addition to the viscous and Reynolds stresses in polymer drag reduced flow, because the sum of viscous and Reynolds stresses no longer equals the total stress. Japper-Jaafar et al. (2009) investigated scleroglucan which is a rigid polymer, in a fully developed turbulent pipe flow. At a constant Reynolds number of 67,000, their results showed that axial and radial turbulence intensities in wall coordinate for water are consistent with Ptasinski *et al*. (2001) at low concentrations, and they also reported that tangential turbulence intensity decreases.

Walker and Tiederman (1990) studied the effect of the injection of a concentrated polymer solution at the wall on turbulence in a channel flow with LDV measurements in streamwise and wall-normal directions. They reported a drag reduction of up to 44 % when a polymer solution was injected in the region from 150 to 250 mm downstream of the injector. They showed that the peak of streamwise Reynolds stress normalized with friction velocity of flow without injection increased by 15% and shifted away from the wall. The wall-normal Reynolds stress and shear Reynolds stress were decreased. However, when the polymer solution was injected in the region from 50 to 150 mm downstream of the injector, the drag reduction approached 25%. The results showed an increase in streamwise Reynolds stress and Reynolds shear stress. In addition, there is a slight increase in wall-normal Reynolds stress in the buffer layer which is not observed at 44% drag reduction. In another study, Warholic *et al*. (1999) used 2D-LDV measurements to investigate the effect of the injection different polymer concentrations on turbulence statistics in channel flow. The master polymer solution of Percol 727 was injected through wall slots. In their experiments, they observed that streamwise Reynolds stress normalized with friction velocity of polymer solution increases at low drag reduction and decreases at high drag reduction compared with water flow at constant flow rate. They also reported that wall-normal Reynolds stress and shear Reynolds stress decreases with increasing drag reduction. Polymer stresses were noted in the viscous sublayer at low concentration and

throughout the cross section of the channel at high concentration. The Reynolds stress was almost zero at maximum drag reduction. This finding was confirmed in subsequent work by Warholic *et al.* (2001) with 2D-PIV measurements in channel flow. Mohammadtabar *et al.* (2017) investigated the turbulent structure of a rigid polymer (Xanthan Gum) in a turbulent channel flow using 2D-PIV. The results of this experimental study showed the wall-normal Reynolds stresses and Reynolds shear stresses are significantly decreased at concentration of 125 ppm. The peak value of streamwise Reynolds stresses at concentration of 100 ppm increased to level above that for water at a constant flow rate, while it decreased to the same level as water flow for 125 ppm. In their results, the Reynolds stresses were normalized using the inner scaling of water. Their results also showed that the angle of the principal axis of the Reynolds stress tensor with respect to the wall in quadrant analysis near the wall decreases with increasing polymer concentration. The spatial-correlation of the fluctuating velocity field showed that the spatial coherence of u fluctuations in the streamwise direction increases with increasing polymer concentration.

A more detailed measurement of coherent structures can enhance the understanding of the mechanism of polymer drag reduction. Achia & Thompson (1977) investigated the effect of polymer additives on turbulent structures near the wall in pipe flow using a real-time hologram interferometer (flow visualization technique). They reported that an increase in the mean spanwise spacing between low-speed velocity streaks was accompanied by a decrease in burst rate in drag-reduced flow when compared to that of the solvent alone, at almost the same shear velocity. In other flow visualization studies, pre-mixed polymer solutions in turbulent channel flow of Donohue *et al*. (1972) and Tiederman & Oldaker (1977) both reported that the time interval between bursts of a streak at the same wall shear stress for a drag-reduced flow and a water flow were almost the same. This agrees with results of Achia & Thompson (1977) in pipe flow when compared at the same wall shear stress. This means that a polymer does not directly affect bursting events. On the contrary, Tiederman *et al.* (1985) and Walker *et al.* (1986) carried out wall-injection polymer solution experiments in channel flow with flow-visualization. They found that streak spacing increased and the burst rate decreased for polymer solutions compared with water flow at the corresponding shear velocity. In another polymer injection experiments in a pipe flow, similar results were obtained by McComb & Rabie (1982). Due to the wall injection of high polymer concentrations in the aforementioned studies, it is expected that there

are large gradients of concentration in the wall-normal direction. Therefore, the investigation of the polymer effect can be in a disequilibrium state. Bogard & Tiederman (1983; 1986) concluded that the flow visualization method that was used to deduce the time between bursts of a streak were not accurate because the events within the field of view were not completely counted. Luchik & Tiederman (1988) also confirmed that the flow visualization technique is not practical to obtain statistical velocity quantities based on conditional sampling, though Tiederman *et al.* (1985) showed accurate results of the average burst rates. Luchik and Tiederman (1988) used LDV to measure streamwise and wall-normal velocities in very dilute polymer solution channel flow with injection system. They found an increase in average time between bursts and the streak spacing in drag-reduced flow when compared to its Newtonian counterpart at the same wall shear stress. In addition, they showed that an increase in the average spanwise streak spacing equals the increase in the time scale.

Chapter 3. Experimental Setup

Two different experiments with different objectives are carried out in this thesis. In the first experiment, two-dimensional time-resolved PIV is used to obtain the turbulent statistics of water and polymeric flow. In the second experiment, three-dimensional measurements of the channel flow, using time resolved 3D-PTV with "Shake-the-box" method are used to evaluate turbulence structure for Newtonian (water) and Non-Newtonian flows (shear thinning-high concentrated polymer solutions. The results of these experiments for water flow are compared with DNS in order to evaluate the measurement accuracy.

This chapter describes the experiments in five sections. The first section describes the flow loop. In the second and third section, the polymer preparation and rheological measurements are explained, respectively. The 2D-PIV setup and image processing procedure are described in the fourth section. Finally, the 3D-PTV setup and image processing procedure are covered in the fifth section.

3.1 Flow loop

The experiments were conducted in a recirculating flow loop in the Department of Mechanical Engineering of the University of Alberta, as shown in Figure 3.1 (a). The loop has a test section with a rectangular cross-section of 120 mm width (W) and 15 mm height (H) and aspect ratio of W/H=8. The hydraulic diameter D_h is defined as $2WH/(W+H)$ and is equal to 26.66 mm. The x-axis is parallel to the flow direction, the y-axis is normal to the bottom of the channel positive in the upward direction and the z-axis is spanwise direction as shown in Figure 3.1 (b). The test section has cast acrylic sidewalls and removable top and bottom glass plates for physical and high quality optical access. The 2D-PIV/3D-PTV measurement region is located 1600 mm (106.66H) downstream of the channel inlet to ensure that the flow is fully developed. The total length of the rectangular channel is 2500 mm (166.67H). Two transition sections are placed at the entrance and exit of the channel in order to change the cross section gradually from circular to rectangular and vice versa. The pipes sections of the loop are schedule 40 stainless steel (SS-304 L) and PVC plastic with 2 inch diameter.

A centrifugal pump (LCC-M 50-230, GIW Industries Inc.) is used to circulate the test fluid through the flow loop. A progressive cavity pump (Moyno 2F090G1CDB3SAC, Liberty Process Equipment) with (10 HP) motor also is used to. compare the degradation of the polymer solution as a result of operating the Moyno and the centrifugal pump. A pulsation dampener is installed after the pump in order to absorb the flow pulses coming from the Moyno pump. All experiments reported in this thesis are carried out at a constant flow rate. Experiments and DNS analyses at constant flow rates have also been applied by previous investigations in polymer drag reduction by Harder and Tiederman (1991), Warholic *et al.* (1999), Warholic *et al.* (2001), and Min *et al.* (2003). A Coriolis flow meter (Micromotion F-series, Emerson Process Management) is used to measure mass flow rate and the density of the fluid. The flow rate is maintained constant at 2.08 kg/s by PID controller through LabVIEW software (National Instruments).

A K-type thermocouple probe (Omega) is used to measure fluid temperature. The instrument is connected to a high precision data acquisition (DAQ) system (NI 9211 by National Instrument) with 4-channel, +/−80mV, 24-bit differential analog input. The fluid is maintained at a constant temperature of 25±0.2 °C using a double pipe heat exchanger. All analog modules are installed in the CompactDAQ chassis (cDAQ-9174) for data collection. The cDAQ system interfaced with a personal computer equipped with LabView 2015 through a simple USB 2 connection, pre-installed for processing the acquired signals. Pressure drop measurement between two pressure ports are collected using a Validyne DP-15 pressure transducer with 0.2 psi diaphragm and an accuracy of ±0.25% using a full scale of diaphragm. The distance between pressure ports is 1 m, which is chosen to be large in order to minimize the relative measuring error associated with the very low range of the diaphragm. The signal from the DP-15 sensor is processed by a sine wave carrier demodulator (Validyne CD-15) with a 1 kHz response to provide a DC output signal. The signals are then acquired using a National Instruments NI-9201 DAQ and digitized with a 12 bit resolution. The data is collected at frequency of 100 Hz. The pressure transducer is calibrated using a Druck DPI 610 pressure calibrator. The measurement data of the flow rate and pressure gradient, temperature and density are sampled automatically with LabVIEW. The Reynolds number based on the full channel height H and the bulk velocity across the channel is Re_H = 20,000 with the water dynamic viscosity of $\mu^{(s)} = 8.684 \times 10^{-4}$ m^2/s based on 2D-PIV /3D-PTV measurements.

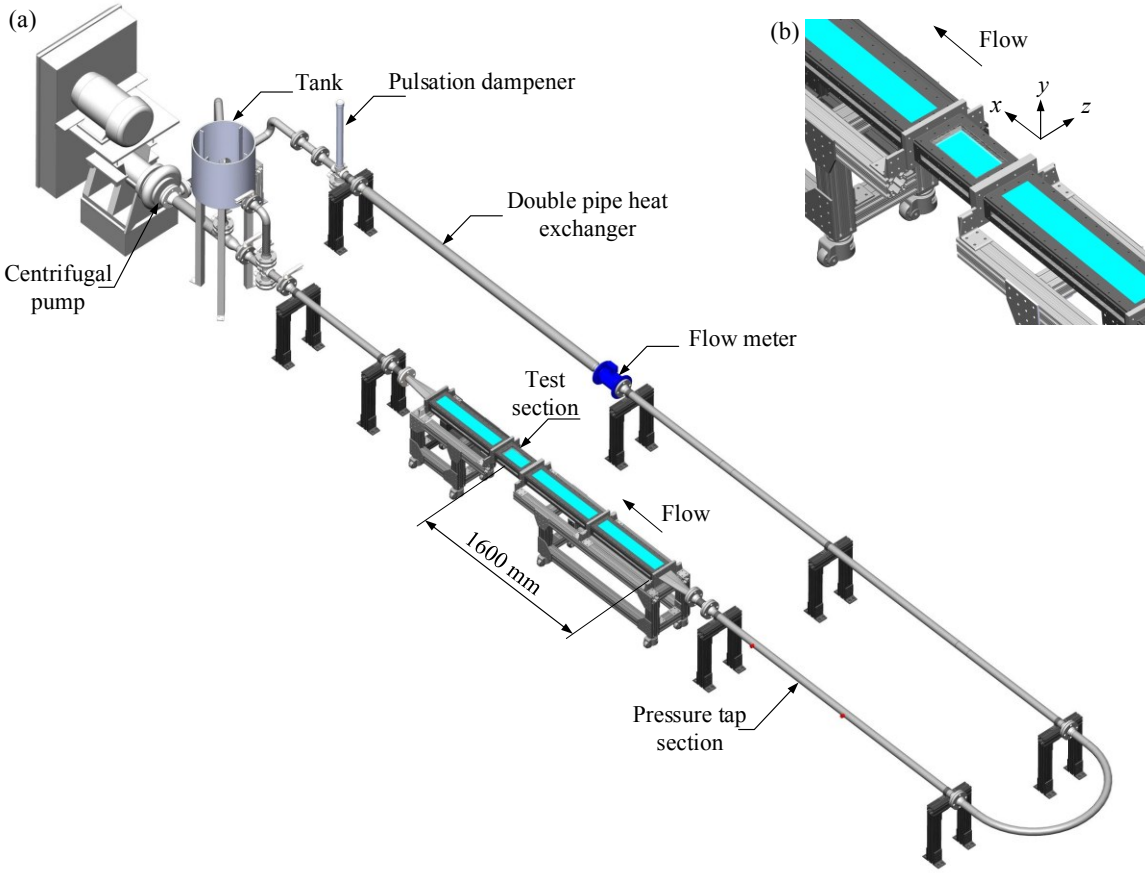

Figure 3.1. (a) Drawing of flow loop facility. (b) Test section with coordinate system.

3.2 Polymer preparation

The polymer additive used is Superfloc A-125V (Kemira Chemicals Inc.), which is anionic polyacrylamide (APAM). The APAM used for this study has a high molecular weight with medium anionic charge density based on the information provided by the manufacturer. Anionic polyacrylamide flocculants are made by either hydrolyzing the amide group (-CONH2) or combining the copolymerization of acrylamide with an anionic monomers (Wu CS 2003). The chemical structure of the anionic polyacrylamide is shown Figure 3.2. The transparency of a well mixed homogeneous polyacrylamide solution provides optical access to collect the light scattered by the tracer particles in optical measurements (PIV/PTV).

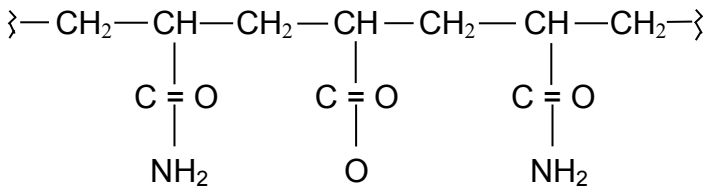

Figure 3.2. Molecular structure of anionic polyacrylamide (Caulfield 2002).

A solution of polymer powder and solvent (tap water) is prepared in a large mixing tank. A schematic of the mixing tank and marine impeller with characteristic dimensions are shown in Figure 3.3. The mixing tank is made from polyethylene and has a capacity of 240 liters, which is equipped with a mixer (Lightnin Labmaster, L5U10F). It is unbaffled and a conical bottom cylindrical tank with a slope of 25º for easy discharge of the fluid from the tank into the pump suction. The tank has a height of H = 82.5 cm and dimeter of T = 58.5 cm. The tank is filled with predetermined amount of water (210 liters) for each experiment to ensure repeatability of the experiments. The three-bladed marine impeller with a diameter of D_I= 250 mm, depth of H_I = 70 mm produces a circulating pattern with upward axial flow in order to draw up air bubbles to the surface. The marine impeller is attached to a shaft with diameter of 10 mm, which is connected to a mixing gear at the top. The impeller is located at height C from the bottom of the tank, which is around a half of the height of the water in the tank. The location of the impeller is recommended to be between a half or third the height of the tank (Tatterson, 1991). Warm tap water at approximate temperature of 60 ºC is stored in storage tanks for a week to reduce the level of dissolved oxygen. Shupe (1981) reported that the removal of oxygen from the Polyacrylamide solution can reduce chemical degradation. The polymer solutions are mixed at

75 rpm for 2 hours. This type of impeller is selected because it produces low shear. Therefore, it minimizes the amount of mechanical degradation during the mixing process. Mechanical degradation is the process in which polymer molecules break down into smaller segments when they are subjected to the high shear of the flow field. This leads to a decrease in polymer molecular weight, thus a decrease in drag reduction.

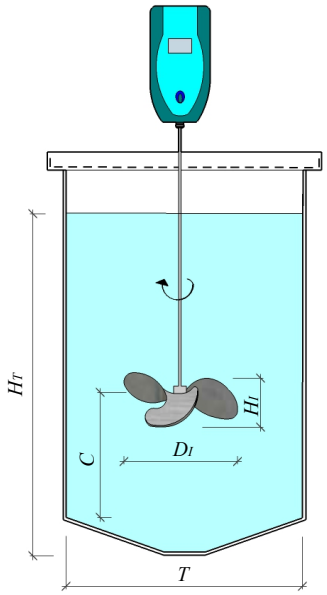

Figure 3.3. Schematic illustration of the mixing tank, the marine impeller, and the characteristic dimensions.

The amount of dry polymer powder required to prepare solution is precisely weighed using analytical balance (Mettler Toledo, AB104-S) with an accuracy of 0.1 mg. The dry polymer powder is spread slowly over the surface of the water (vortex shoulder) when a mixer runs continuously to prevent aggregation or flocculation. Therefore, this mixing procedure allows obtaining homogeneous polymer solutions and avoided the use of Ethylene glycol, which is used to prevent polymer agglomeration. The polymer concentration is varied from 10, 20, 90, and 160 ppm to investigate turbulent structures in the case of dilute and shear thinning polymer solutions, as well as low and maximum drag reduction.

The estimated mixing Reynolds number inside the mixing tank (N_{Re}) for Newtonian fluids can be calculated by the following equation (Metzne & Otto, 1957 ;Sánchez *et al.,* 2006; Tatterson, 1991):

$$N_{Re} = \frac{\rho N D_I^2}{\mu}, \tag{3.1}$$

Since the shear viscosity changes with shear rate in mixing tank for non-Newtonian fluids, Paul (2004) and Metzner and Otto (1957) developed definition of Reynolds number based on a power-law of the flow consistency index, K (Pa.s^n) and the flow behavior index of the fluid, n.

$$N_{Re}^{*} = \frac{\rho N^{(2-n)} D_I^2}{K\, k_s^{(n-1)}}, \tag{3.2}$$

Where ρ is the density of fluid (kg/m^3), N is the rotational speed (s^{-1}), D_I is the impeller diameter (m), μ is the apparent fluid viscosity (Pa.s). When the N_{Re} is below 10, the flow is laminar. Turbulent flow occurs when the N_{Re} exceeds 10,000 (Tatterson, 1991). The impeller speed is proportional with shear rate with the constant k_s

$$k_s = \left(\frac{\mu}{K}\right)^{1/(n-1)} \frac{1}{N}. \tag{3.3}$$

The average shear rate (Sánchez *et al.* 2006) in Newtonian turbulent mixing condition fluid is

$$\gamma_T = \left(\frac{4 N_p \rho D_I^2}{27\,\pi\,\mu}\right)^{\frac{1}{2}} N^{3/2}. \tag{3.4}$$

In the case of non-Newtonian power law turbulent mixing condition, the average shear rate is described by:

$$\gamma_T = \left(\frac{4 N_p \rho D_I^2}{27\,\pi\,K}\right)^{\frac{1}{1+n}} N^{\frac{3}{1+n}}, \tag{3.5}$$

where N_p is the power number (Sánchez *et al.*, 2006; Tatterson, 1991):

$$N_P = \left(\frac{P}{\rho D_I^5 N^3}\right), \tag{3.6}$$

where P is the input power in watts. Stoops and Lovell (1943) reported power consumption correlation based on a marine impeller with three blades:

$$P = 0.56\,\mu N^2 D_I^3 \left(\frac{\rho N D_I^2}{\mu}\right)^{0.81} \left(\frac{T}{D_I}\right)^{0.93}. \tag{3.7}$$

The values of the Reynolds number and the average shear rates (γ_T) at mixing sped of 75 rpm for different concentrations, based on viscosity measurements (detailed in section 3.3), are presented in Table 3.1.

Table 3.1. Reynold number and shear rates of the polymer solutions based on the mixing conditions.

Polymer concentration	Consistency index (Pa.s^n), K	Power-law index, n	γ_T(s^{-1})	Reynolds number
10 ppm	-	-	28.87	77812
20 ppm	-	-	26.81	64844
90 ppm	0.0099	0.264	40.26	2819
160 ppm	0.0132	0.271	32.55	1921

3.3 Rheology

3.3.1 Shear viscosity measurements

Viscosity is a significant parameter in the investigation of polymer drag reduction. Since it is well known that addition of a certain amount of polymer to a Newtonian fluid can alter the rheological properties into that of a non-Newtonian fluid, the viscosity measured here is the shear viscosity (apparent viscosity). The rheological characterization of polymer solutions is investigated using a rheometer (RheolabQC, Anton Paar USA Inc.) equipped with a double gap cylinder measuring system (DG42). The advantage of using a double gap cylinder with small clearance is that it is suited to measure low viscosity fluids at high shear rate in a laminar flow and prevents formation of Taylor vortices and transition to turbulence (Taylor 1923). The rheological characterization requires that measurements of viscosity be carried out at different shear rate in case of non-Newtonian fluids. Figure 3.4 shows the schematic of bob and cup geometry of a double gap concentric cylinder (DG42, Anton Paar USA Inc.) with the dimensions are summarized in Table 3.2. The rheometer consists of cup with an inner cylinder and a bob attached to a rotor. The cup remains stationary whereas the bob is driven by a motor. A temperature control is connected to the cup to maintain the desired temperature. The rheometer (DG42) provides measurements over a range of shear rate from 4×10^{-2} to 9×10^{3} s^{-1} and apparent viscosity from 10^{-4} to 7×10^{3} Pa.s. The rheometer is connected to a computer and controlled via commercial software (Rheoplus/32 V3.62, Anton Paar USA Inc.).

Measurements are carried out at a shear rate up to 1100 s^{-1}, and a constant temperature (25˚C). In the case of dilute polymer solutions at concentration of 10 and 20 ppm, the solution viscosity slightly increases with increasing polymer concentration and showed Newtonian behavior, in which the viscosity is independent of shear rate, as illustrated in Figure 3.5. As polymer concentration increases, the solution viscosity significantly increases and non-Newtonian behavior appears. The viscosity of polymer solutions at concentration of 90 and 160 ppm showed shear-thinning behavior, in which the viscosity decreases with increasing shear rate. A strong shear-thinning behavior increases as expected with the concentration. The apparent viscosity for shear thinning polymer solution at the wall of the channel ($\mu_w^{(p)}$) is used for inner-wall scaling. The shear rate at the wall $(d\langle U\rangle/dy)_w$ is estimated using 2D-PIV/3D-

PTV measurements in order to obtain near-wall viscosity from viscosity measurements, shown in Figure 3.5.

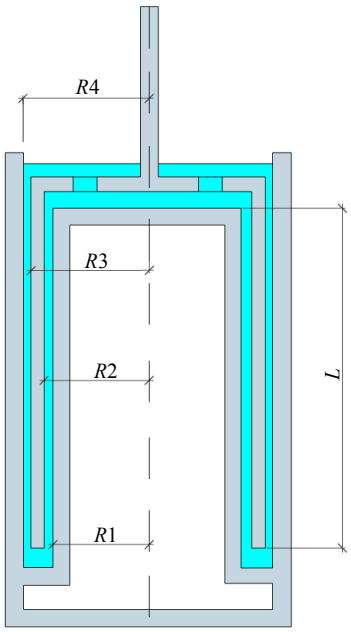

Figure 3.4. Schematic of the double gap concentric cylinder (DG42).

Table 3.2. Dimensions of the measuring bob and cup of the (DG42) rheometer in (mm)

Internal radius of the measuring cup (*R1*)	19.748
Internal radius of the measuring bob (*R2*)	20.2435
External radius of the measuring bob (*R3*)	20.9970
External radius of the measuring cup (*R4*)	21.5055
Effective measuring gap (*L*)	78.700
Internal gap	0.4955
External gap	0.5100

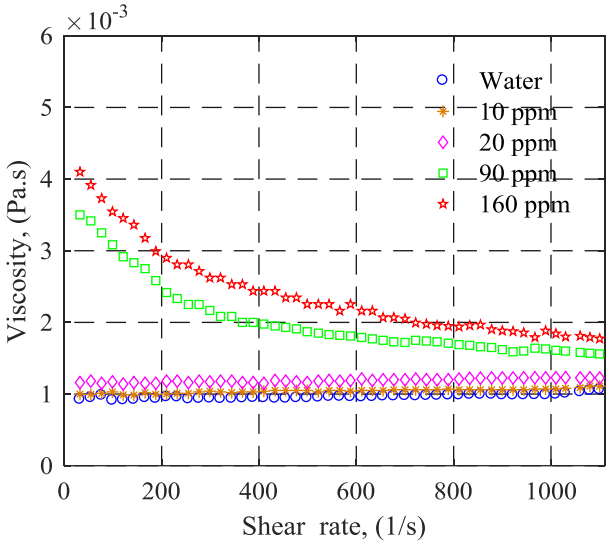

Figure 3.5. Apparent viscosity as a function of shear rate for water and the four polymer solutions showing rheological behavior of the fluid.

3.3.2 Extensional viscosity measurements

The extensional rheological behavior of superfloc A125V was evaluated using a capillary break-up extensional rheometer (Haake CaBER, Thermo Scientific). A small sample of each polymer solution is placed carefully between two circular plates with 6 mm diameter (D_P) using a syringe. In order to minimize shear, the syringe is used without a needle. The initial separation between two plates (h_i) is 2 mm and then the top plate rapidly separates from the bottom plate until a final height (h_f = 8.2 mm) at a constant extension rate is reached. The initial and final ratio, defined as h_i / D_P and h_f / D_P are set as 0.33 and 1.36, respectively. The typical stretch time (strike time) applied for all solutions is 50 ms. The filament thickness (midpoint diameter) at half the stretching height is monitored with a laser micrometer as a function of time after reaching the final height. After stretching, the thinning fluid filament between endplates imposes a uniaxial extensional flow.

The extensional relaxation time is estimated using the upper-convected Maxwell model by regression of the data. Entov & Hinch (1997) reported that viscosity dominates the initial phase, which is followed by an intermediate time-scale. The dynamic of the filament drainage in the intermediate time-scale is governed by a balance between surface tension and elasticity instead of viscosity of solution. The linear section of the data in a semi-logarithmic plot of filament diameter versus time, representing the elastic region, are extracted to fit with the upper-

convected Maxwell model by regression as given in equation (3.8). The extensional relaxation time is calculated based on the data. The surface tension of water (σ), 73 milli N/m is considered as the same for polymer solutions. The experimental work of Erik *et al*. (2009) showed that even at high polymer concentration (10,000 ppm, polyacrylamide) surface tension is 72 milli N/m.

$$D_{mid}(t) = D_0 \left(\frac{G\, D_0}{4\,\sigma}\right)^{\frac{1}{3}} e^{\left(\frac{-t}{3\tau_{ext}}\right)}, \tag{3.8}$$

where τ_{ext} is a characteristic relaxation time , G is elastic modulus of the filament which can be obtained from fitting the data, D_0 is the initial diameter of the sample and $D_{mid}(t)$ is the mid-point diameter of the filament.

The evolution in the midpoint diameter is governed by the balance between forces on the filament as showed in following equations (Yarin, 1993; Renardy, 1995):

$$3\,\eta_S \left(-\frac{2}{D_{mid}}\,\frac{d\,D_{mid}}{dt}\right) = \frac{F_Z}{\pi\,(D_{mid}/2)^2} - [\tau_{zz} - \tau_{rr}] - \frac{\sigma}{(D_{mid}/2)}\,, \tag{3.9}$$

where F_z is the tensile force acting on the column ends, η_s is solvent viscosity. The term on the left-hand side of equation (3.9) represents the viscous stress. The first and second term on the right-hand side of the same equation indicate the difference of tensile and normal stress for non-Newtonian elastic stress. The last term on the right-hand side expresses capillary pressure.

The evolution of the midpoint diameter of fluid samples with time in a Haake CaBER device is driven by the capillary force and resisted by the extensional stress and viscous force (Anna & McKinley 2001; McKinley 2005; Kim *et al*. 2010). The equation (3.9) can be reduced to

$$3\,\eta_S \left(-\frac{2}{D_{mid}}\,\frac{d\,D_{mid}}{dt}\right) + [\tau_{zz} - \tau_{rr}] = \frac{2\sigma}{(D_{mid})}\,. \tag{3.10}$$

The strain in extension is usually defined as a Hencky strain as shown by the following equation (Schummer & Tebel, 1983):

$$\varepsilon(t) = 2\ ln\left(\frac{D_0}{D_{mid}(t)}\right). \tag{3.11}$$

The strain rate is defined as (Schummer & Tebel, 1983):

$$\dot{\varepsilon}(t) = -\frac{2}{D_{mid}(t)}\left(\frac{d\,D_{mid}(t)}{dt}\right). \tag{3.12}$$

The apparent extensional viscosity ($\eta_{app}(e)$) is defined in the following equation. The derivations of this equation is detailed in previous studies (Anna & Mckinley, 2001; Kim *et al*., 2010).

$$\eta_{app}(e) = -\frac{(2x-1)\sigma}{\frac{dD_{mid}}{dt}}, \tag{3.13}$$

where x is the correction factor for axial variation and its value is 0.7127 in the CaBER experiment (McKinley &Tripathi 2000).

Entov and Hinch (1997) reported that fluid relaxes at the rate 2/3 of strain rate during filament drainage using the FENE model. The maximum elasticity occurs at the critical Deborah number of 0.66 when filament drainage is constant. The Deborah number is the dimensionless product of the polymer relaxation time and the strain rate (Kim *et al*., 2010).

Figure 3.6 shows the effect of polymer concentration on filament diameter as a function of time. The negative time represents the period before reaching the final height (h_f) and zero time represents the time when the top plate reaches the final height. The error bars show maximum variation based on uncertainty analysis. For proper estimation of uncertainty, more independent experiments are required. The results showed that dilute polymer solutions of 10 and 20 ppm break up at a diameter of 0.08 and 0.077 mm, respectively, while the concentrated polymer solutions of 90 and 160 ppm break up at 0.0123 and 0.0117 mm, respectively. There is a slight increase in resistance to capillary force at 20 ppm compared with 10 ppm. It is obvious that dilute polymer solutions undergo a more rapid filament breakup than concentrated polymer solutions. This is due to low elasticity at dilute polymer solutions. The polymer solutions that have higher relaxation time will show more elasticity (Marshal and Metzener, 1966). Delshad *et al*. (2008) also used the relaxation time to represent the elasticity in polymers in a viscoelastic model. It is also noticeable that solution resistance to capillary force increases with increasing polymer concentration. Therefore, concentrated polymer solutions have higher potential to stretch more than dilute polymer solutions.

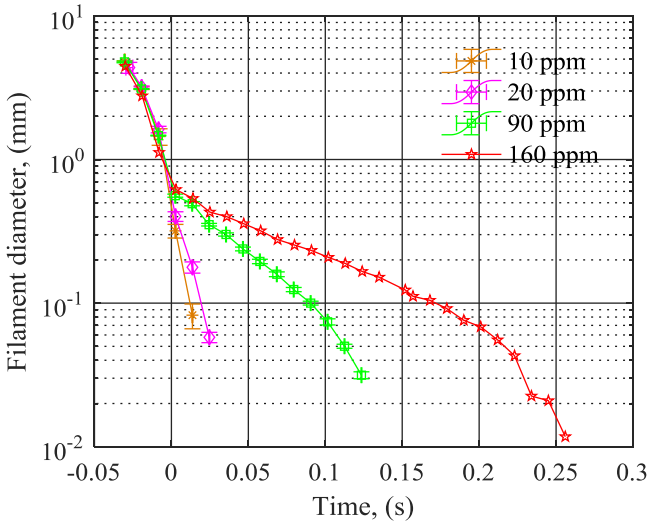

Figure 3.6. A semi-logarithmic plot of filament diameter as a function of time for four different polymer concentrations. The error bars represent minimum and maximum of filament diameter and time (peak-to-peak) for three measurements.

The effect of polymer concentration on the extensional viscosity as a function of Hencky strain is presented in Figure 3.7. Hencky strain shows the ability of polymer molecules to retain its extensional properties when they are subjected to stretch. In the case of dilute polymer solutions, the extensional viscosity reaches the peak then starts decreasing which shows strain loosening behavior. For concentrated polymer solutions, the extensional viscosity increases with increasing Hencky strain which shows strain hardening characteristics. The results indicate that concentrated polymer solutions have more flexibility, extensibility and higher elasticity compared with dilute polymer solutions.

A semi-logarithmic plot of extensional viscosity as a function of generated strain rate for four different polymer concentrations are presented in Figure 3.8. The maximum extensional viscosity corresponding to the critical Deborah number and other properties are presented in Table 3.3. The extensional relaxation time is estimated using equation (3.8) and the strain hardening index obtained from the fitting of the extensional viscosity data as a function of Hencky strain.

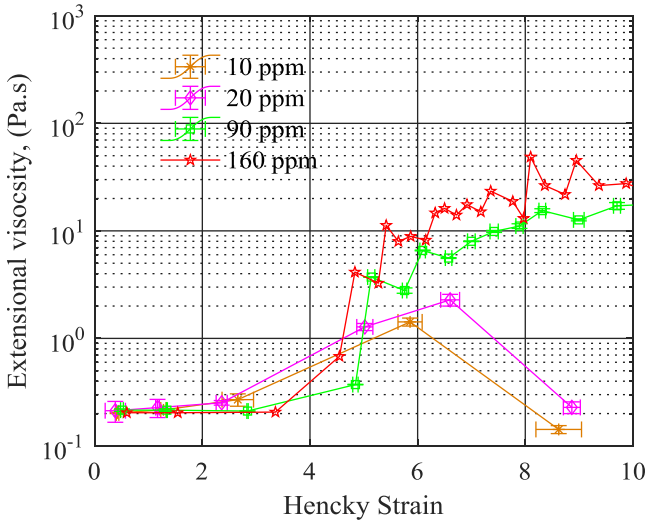

Figure 3.7. Evolution in the apparent extensional viscosity of different polymer solutions as a function of Hencky strain.

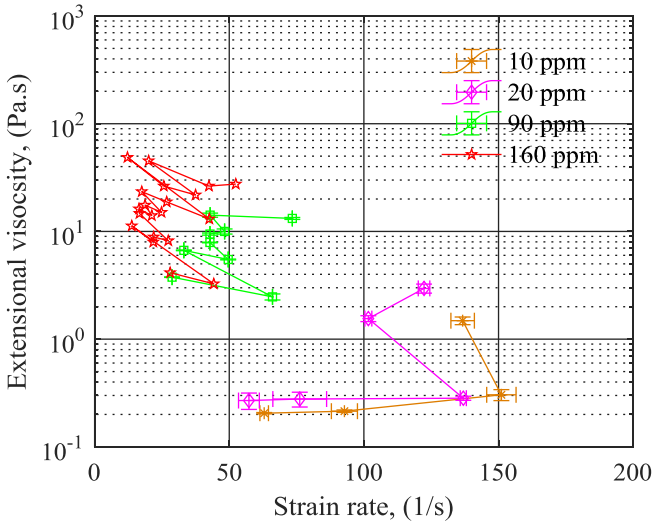

Figure 3.8. A semi-logarithmic plot of extensional viscosity as a function of strain rate.

Table 3.3. Measured and computed properties of four different polymer concentrations as determined from CaBER experiments.

Polymer concentration	Relaxation time, (s)	Maximum extensional viscosity, (Pa.s)	Strain hardening index
10 ppm	0.00265	1.42	0.2244
20 ppm	0.00425	2.28	0.4784
90 ppm	0.0164	14.91	1.78
160 ppm	0.0304	25	2.35

3.4 Planar particle image velocimetry (PIV)

PIV measurements were carried out to cover the near-wall region with a high-speed CMOS camera (Phantom v611, Vision Research). The camera has a sensor size of 1280 × 800 pix with a pixel size of 20 microns and 12 bit resolution. The camera is equipped with a Micro-Nikon 105 mm lens with an aperture setting of f/8. Instantaneous measurements are made of velocity vectors in the streamwise wall-normal (x-y) plane. For the illumination of tracer particles, a dual-cavity Nd:YLF Laser (DM20- 527 DH, Photonics Industries Inc.) is used with output of 20 mJ per pulse at 1 kHz, and repetition rate from 1 to 10 kHz per cavity. The laser pulses are focused into a sheet with a thickness less than 1 mm in the streamwise direction parallel to the channel walls using a combination of cylindrical and spherical lenses. The PIV configuration is shown in Figure 3.9. Silver-coated glass spheres (SG02S40, Potters Industries Conduct-O-Fil®) were chosen as tracer particles, whose density is 4 g/cm^3 and their average diameter is 2 μm. The digital resolution is 71.4 pixel/mm at a magnification of M = 1.42 and the field of view (FOV) is 12.5 mm× 5.4 mm in the streamwise and wall-normal directions, respectively. The depth of field (DOF) is estimated 1.77 mm. The details of the measurement specifications are listed in Table 3.4. The PIV images are captured in single-frame at 16 kHz with a pulse separation of Δt = 62.5 μs by staggered operation of the laser cavities. The synchronization of the laser and camera is accomplished by the Programmable Timing Unit (PTU X, LaVision GmbH) which is controlled by DaVis 8.3 software.

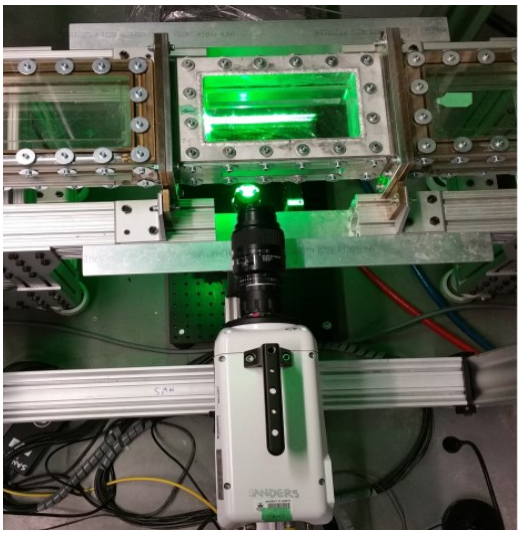

Figure 3.9. Experimental setup of planar PIV in the x-y plane.

Six uncorrelated datasets of 16,294 images is collected for every polymer concentration and also the Newtonian flow of water. Polymer degradation has been avoided during PIV recordings by using the high-speed camera. In order to increase the signal to noise ratio, the minimum intensity of the ensemble is subtracted from the individual images then normalizing every image with the ensemble average. The instantaneous velocity fields for turbulent intensities are obtained from sliding sum of correlation with a filter length of 2 (number of neighboring images around a certain image) and image time steps of 2 between image pairs that are correlated. The sliding sum of correlation is performed with final interrogation windows of 16×16 pix (224x224 μm^2) with 75% overlap. The vector fields for the mean velocity profile are obtained from the ensemble of correlation (EC) (Meinhart *et al*. 2000). The initial window size and final window size are 64×64 pix and 6×6 pix (84x84 μm^2) with overlap 75% elongated with 4:1 aspect ratio in the streamwise direction. The processing of all PIV data sets is conducted in Davis 8.3 (LaVision, GmbH). The percentage of drag reduction and flow parameter for each polymer solution are presented in Table 3.5.

Table 3.4. Specification of the planar PIV system. The dimensions with superscript $^+$ are normalized using wall unit λ_0 = 14.79 μm of water.

Data set	16,294	
Magnification	1.42	
Digital resolution	71.4 pix/mm	
Time interval Δt (μs)	62.5	
Measurement field (Δx, Δy)	892×385 pix 12.5×5.4 mm^2 $845.15^+ \times 365.1^+$	
Velocity evaluation	Single-frame correlation	Ensemble of Correlations
Interrogation region (x, y)	16×16 pix 224×224 μm^2 $15.15^+ \times 15.15^+$	6×6 pix 84×84 μm^2 $5.68^+ \times 5.68$
Window overlap	75 %	75%

Table 3.5. Drag reduction and flow parameters for water and polymeric flows. DR% is calculated based on τ_w in the channel from PIV measurements.

	DR %	u_τ (m/s)	μ_w(Pa.s)	τ_w (Pa)	dU/dy (1/s)	λ (μm)
Water	0	0.0589	0.868 e^{-3}	3.464	3991	14.79
10 ppm	23	0.052	$1e^{-3}$	2.680	2680	19.29
20 ppm	42	0.0452	$1.2e^{-3}$	2.025	1687	26.63
90 ppm	54	0.0392	$1.6e^{-3}$	1.611	1007	40.94
160 ppm	60	0.0374	$2.05e^{-3}$	1.4	683	54.98

The strain rate tensor has to be evaluated along the Lagrangian trajectories because polymer molecules are advected with the local bulk flow (Gyr & Bewersdorff, 2013). The main scheme for calculating the strain rate is in the Lagrangian frame, while the Eulerian method is also reported for comparison. The fluid parcel travels on a trajectory with velocity $\boldsymbol{U_P}$ passing through the grid node at location $\boldsymbol{x_p}$ (t_o) at time t_o. The new location of a fluid parcel at time $t_o+n\Delta t$ is estimated by following the 2D velocity vector $\boldsymbol{U}_p(t_o)$ where n is the time step, as shown in Figure 3.10 (a). In order to estimate the velocity at grid node position (white squares in Figure 3.10 (a &b).), interpolation for 2-D gridded data in meshgrid format is used. The tracks at specific wall-normal location are linked together in order to get long track. The magnitude of frequency resolution is applied based on the length of short tracks which they have the same length. For instance, the frequency resolution is 200 Hz for short tracks with length of 80 time steps.

(a)

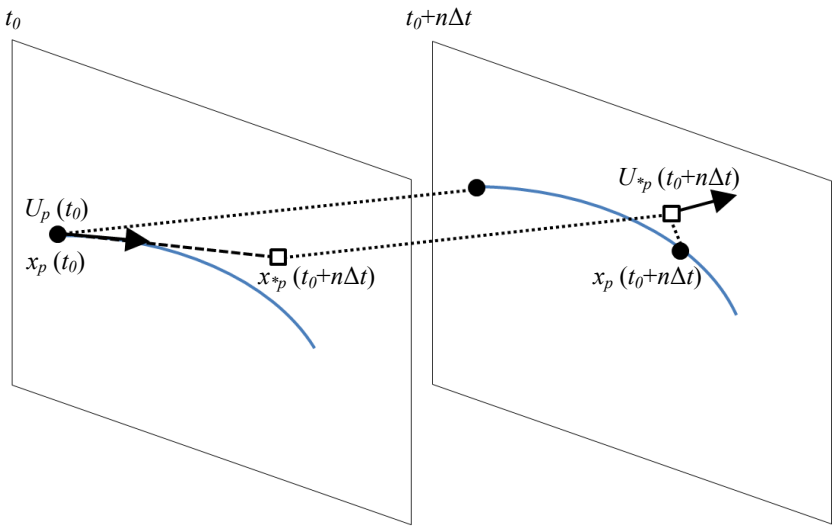

(b)

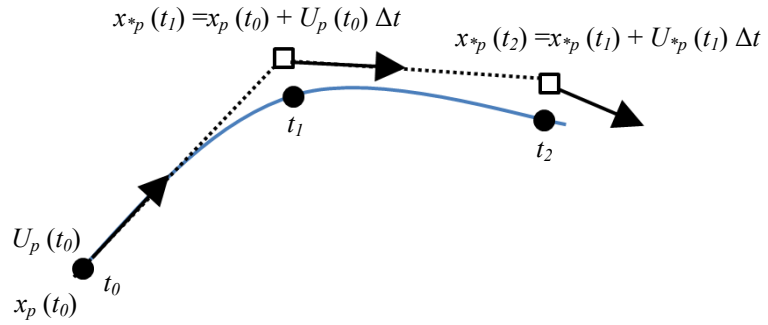

Figure 3.10. Schematic diagrams of Lagrangian method used to calculate the Lagrangian tracks. (a) The location of fluid parcel at grid point is $\boldsymbol{x_p}$ at time t_o then it is tracked forward in time ($t_o+n\Delta t$). (b) Trajectory crosses consecutive images (step =1). Black dots represent the actual positions of the fluid parcel moving along trajectory while white squares represent the estimated positions.

3.5 Particle tracking velocimetry (3D-PTV)

The time resolved 3D-PTV is applied to measure the three components of velocity within a volume. The imaging system consists of four Vision Research Phantom v611 cameras similar to the ones used in the PIV system. The cameras are operated with a cropped sensor of 1024×608 pix^2. The cameras are arranged in a symmetrical cross-like configuration with solid angle of ~35º as shown in Figure 3.11. Each camera is equipped with a Scheimpflug adapter, which is used to align the objective focal plane with the mid-plane of the illuminated area so that all particles within the light sheet are in focus. Four Micro-Nikon lenses of focal length 105 mm are used at aperture setting of f /16. The flow is seeded with 2 μm silver-coated glass beads (SG02S40, Potters Industries Conduct-O-Fil®) whose density is 4 g/cm^3. The illumination of the tracer particles is provided by the same laser that used in PIV system. The laser is introduced from the side of the channel and collimated into a laser sheet of 64 mm wide and 4 mm thick. Knife-edge filters are attached to the both side walls of the channel in order to cut off the low-energy tails of the expanded laser sheet and create top-hat light intensity distribution. The acquisition frequency in single-frame mode is 6 kHz to limit particle displacement to 3.92 pix. The laser and cameras are synchronized using the Programmable Timing Unit (PTU X) and controlled by DaVis 8.3 software. The magnification is 0.407, which yields a digital resolution of 20.25 pix/mm. The achieved measurement volume is 50×4×30 mm^3 (1013×81×608 voxel) in streamwise (x), wall-normal (y), and spanwise (z) directions, respectively. The particle image diameter is around 3 pixels. Inside the volume 24,500 particles are distributed corresponding to 0.038 particles per pixels. The cameras are calibrated using a 3D target (type-11) in Davis 8.3 (LaVision GmbH). An ensemble of 9,000 images are collected with Δt = 166.66 μs in single-frame mode.

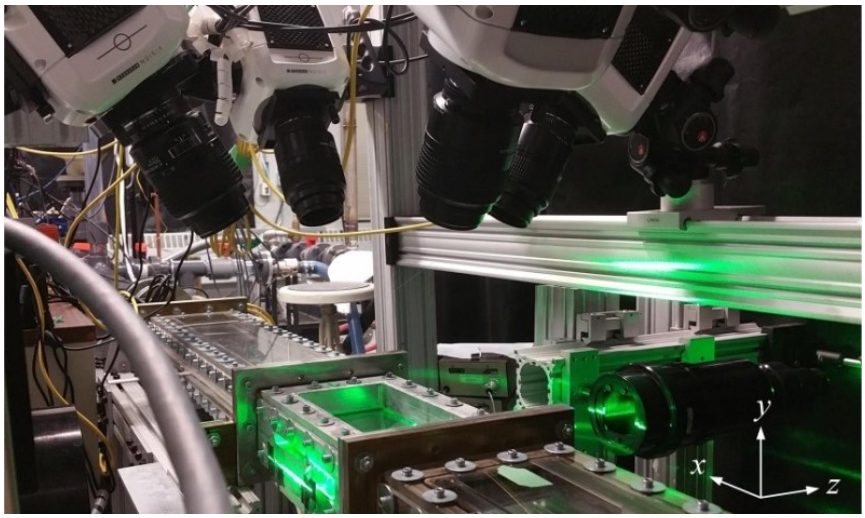

Figure 3.11. Experimental setup of 3D measurements in a symmetrical cross-like configuration with solid angle of ~35º.

The image preprocessing is applied to remove background noise and enhance the particle image quality before volume self-calibration and the calculation of the optical transfer function. The image preprocessing includes subtracting sliding minimum, normalizing with local average and Gaussian smoothing. Volume self-calibration is used to remove any residual calibration disparities using recorded images. The maximum amount of disparity has been reduced to 0.12 pixel and standard deviation to 0.014 pixel. Optical transfer function is calculated to reconstruct virtual camera images precisely which is used to optimize 3D particle positions and intensity. The determination of the 3D location of the individual particles is based on the "Shake-the-Box" algorithm (Schanz *et al*., 2016) in Davis 8.4. The maximum triangulation error is set 0.5 vox for particle intensity threshold of 250 counts. The detected particle velocities are discretized into wall normal bins. Detailed information about the imaging system of the 3D-PTV setups is summarized in Table 3.6. The optimization of the Shake-the-Box parameters is covered in the Appendix B.

Table 3.6. System specifications of the 3D-PTV measurement setup. The dimensions with superscript $^{+}$ are normalized using wall unit λ_0 = 14.79 μm of water.

Data set	9,000	
CCD-sensor size (cropped)	1024×608 pix	
Magnification	0.4	
Digital Resolution	20.25 pix/mm	
Time interval Δt (μs)	166.66	
Measurement volume (Δx, Δy Δz)	50×4×30 mm^3	
	Mean velocity	Reynolds stresses
Spatial resolution (bin size)	0.5 × 0.5 × 0.5 voxels	0.8 × 0.8 × 0.8 voxels
	0.024 × 0.024 × 0.024 mm^3	0.04 × 0.04 × 0.04 mm^3
	$1.62^{+} \times 1.62^{+} \times 1.62^{+}$	$2.7^{+} \times 2.7^{+} \times 2.7^{+}$

Chapter 4. Pressure measurements

4.1 Introduction

The first group of experiments investigated the effect of polymer concentration on drag reduction using the centrifugal pump. The second group of experiments compares the degradation of the polymer solution as a result of operating the Moyno and the centrifugal pump. The methods of quantifying the degree of polymer drag reduction can be based on pressure measurement or flow rate measurement. In this thesis, the extent of drag reduction was determined by pressure drop measurement along a fully developed turbulent pipe flow at a constant flow rate. Savins (1964) defined the following equation for calculating the percentage of drag reduction in terms of pressure drop:

$$DR = \left(\frac{\Delta P_s - \Delta P_p}{\Delta P_s}\right) \times 100 \tag{4.1}$$

Where ΔP is the measured pressure drop per unit length of the pipe and the subscripts s and p refer to the solvent alone (water), and the polymer solution, respectively. The percentage of drag reduction can also be defined in terms of friction factors;

$$DR = \left(\frac{f_s - f_p}{f_s}\right) \times 100 \tag{4.2}$$

Where f_s is the friction factor of the solvent alone and f_p is the friction factor of polymer solution. The pressure loss is due to the friction between the solid surface and the adjacent fluid layers. By applying a force balance, pressure drop and wall shear stress are related by

$$\tau_w = \frac{\Delta P\, D}{4\, L} \tag{4.3}$$

Where τ_w is the wall shear stress, L is the distance between two ports in pipe, and D is the pipe diameter. The fanning friction factor is then defined as follows:

$$f = \frac{\tau_w}{\frac{1}{2}\rho\, U^2} = \frac{\Delta P\, D}{2\rho\, U^2\, L} \tag{4.4}$$

Where ρ is density of the fluid and U is the mean fluid velocity.

In many previous studies including Virk (1975) proved that the addition of polymers to solvent in laminar flow in smooth and rough pipes Poiseuille's law, i.e.,

$$f = \frac{16}{Re} \tag{4.5}$$

For a Newtonian turbulent flow region in smooth pipes, the friction factor is defined by the Von Karman equation as

$$f^{-1/2} = 4\, log_{10}(Re\, \sqrt{f}\,) \; - \; 0.4 \tag{4.6}$$

Virk (1975) proposed the maximum drag reduction asymptote (MDRA) in terms of fanning friction factor, which is accepted at high polymer drag reduction given by following equation:

$$f^{-1/2} = 19\, log_{10}(Re\, \sqrt{f}\,) \; - \; 32.4 \tag{4.7}$$

Four different polymer solution concentrations (10, 20, 90, 160 ppm) are tested to compare between low and high drag reduction regimes at constant flow rate (2.08 kg/s). The Reynolds number based on the inner pipe diameter (50 mm) and the bulk velocity across the pipe (1.06 m/s) is Re ≈ 61,000 with the water dynamic viscosity of μ = 8.684 × 10^{-4} m^2/s. Each polymer concentration is tested for an hour in order characterize degradation of the polymer against mechanical shear. The data collection starts five minutes after the start of the flow in the loop in every experiment to remove trapped air and bubbles.

4.2 Results and discussion

4.2.1 Effect of polymer concentration

The effect of polymer concentration on the drag reduction using the centrifugal pump is presented in this section. The pressure measurements for water are carried out before every polymer solution experiments in order to ensure that there is no contamination by previous polymeric experiments in the loop. Figure 4.1 shows instantaneous pressure drop measurements in water flow. The results show that the pressure drop remains constant for an hour at a constant flow rate of 2.08 kg/s and the Reynolds number of 61,000.

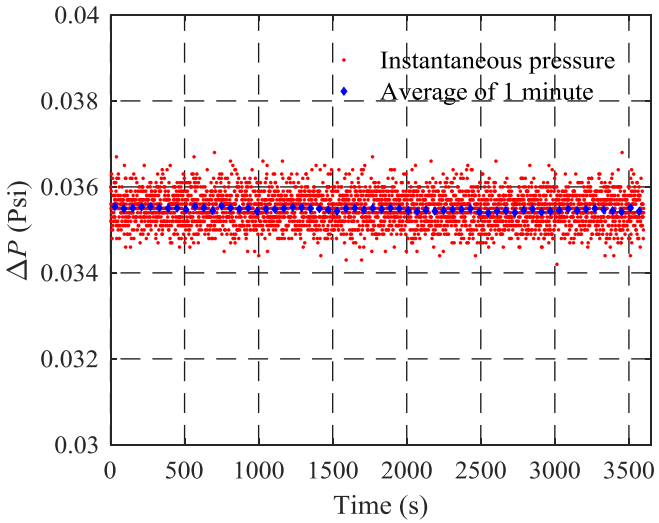

Figure 4.1. Measurement of pressure drop for flow of water.

The pressure measurements for four different polymer concentrations are shown in Figure 4.2. The reduction in pressure drops after one hour for 10 ppm and 20 ppm (low concentration regime) were around 7.92% and 5.96 %, respectively. A the high concentration regime the reduction in pressure drop was about 4.1 % and 3.6% for 90 ppm and 160 ppm , respectively. The results also showed that the range of pressure fluctuations range increases in polymer solution and it increases with increasing the concentrations. The maximum pressure fluctuations ranges are 0.0026 psi, 0.003 psi and 0.0056 psi for water, 20pmm and 160 ppm, respectively.

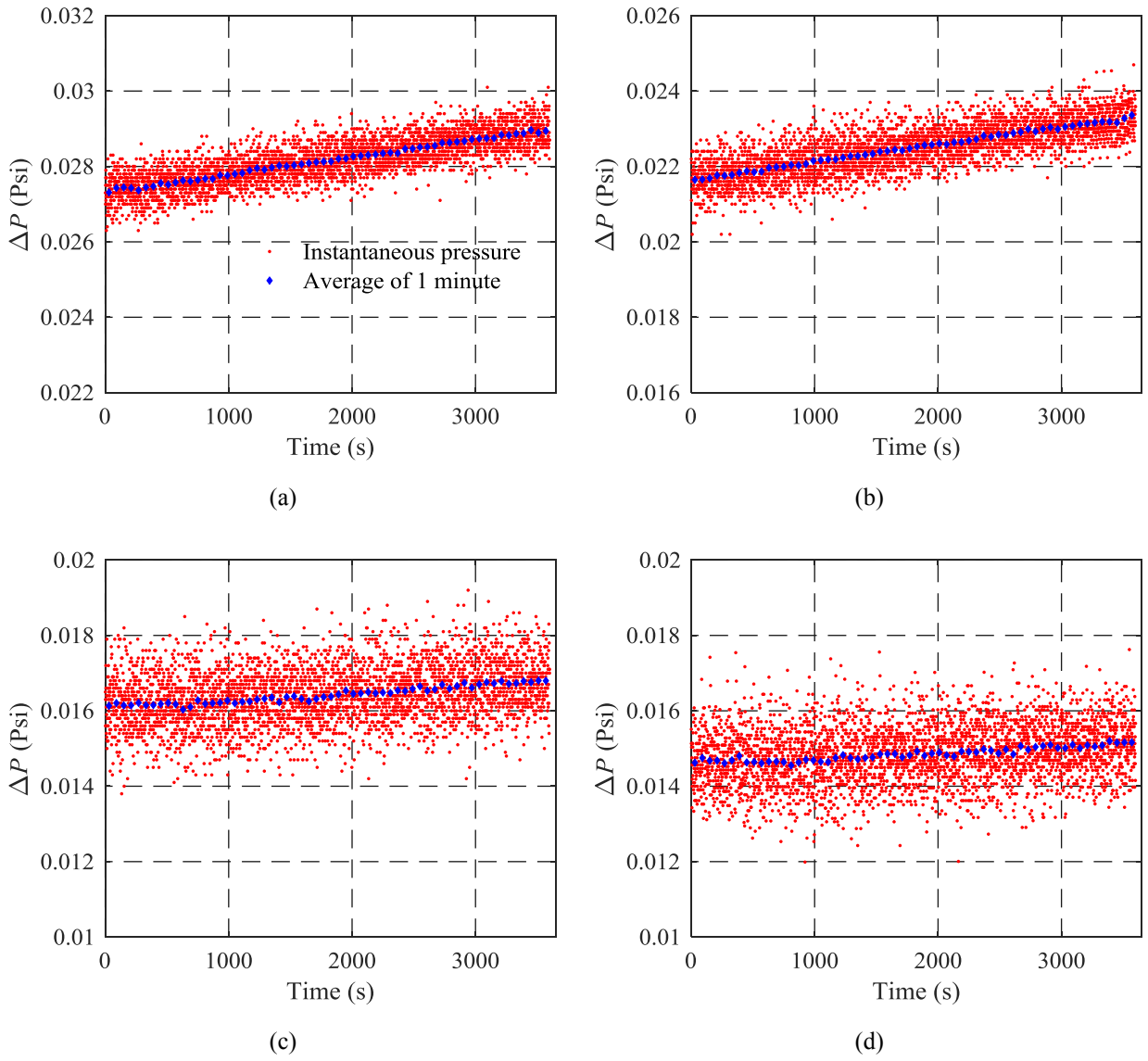

Figure 4.2. Instantaneous pressure drop measurement at (a) 10 ppm (b) 20 ppm (c) 90 ppm (d) 160 ppm.

The effect of polymer concentration on drag reduction is shown in Figure 4.3. The one-hour average drag reduction is 20.69 % for 10 ppm, while a concentration of 20 ppm was around 1.7 times more effective, approaching 37% one-hour average drag reduction. The concentration of 160 ppm achieved the highest drag reduction of all four-polymer concentrations. The increase of concentration from 10 ppm to 160 ppm increased one-hour average drag reduction by 37.47 %. The variation of one-hour average drag reduction at high concentration was not as large as the difference between low concentrations. The one-hour average drag reduction at 160 ppm was 8.24 % higher than that of 90 ppm. The increase of the concentration might have an

inverse effect on drag reduction because of increasing viscosity at maximum drag reduction. However, this case has not been observed at 160 ppm.

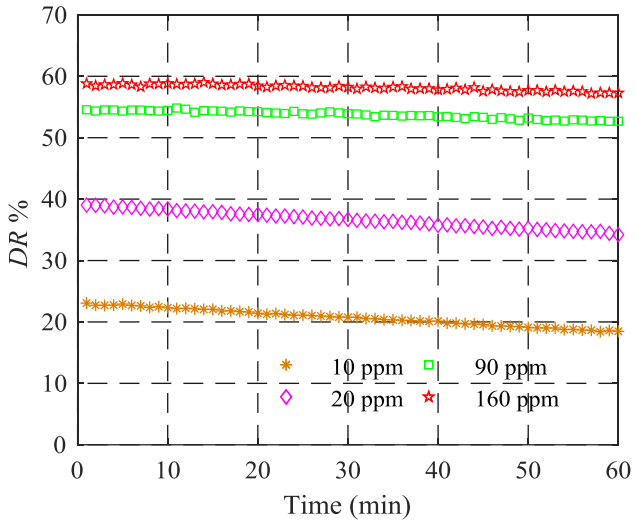

Figure 4.3. Effect of concentration on drag reduction using centrifugal pump.

The results shown in Figure 4.3 also indicate that degradation rate at concentration of 10 ppm is around 21 % in one hour while degradation rate decreased to 12.4 % at concentration of 20 ppm. The effect of polymer concentration on the degradation is more obvious at low concentrations. The degradation rate at 90 ppm and 160 ppm are 3.42% and 2.58%, respectively. Although the same polymer flow passes through the pump and pipes many times, the degradation rate decreased significantly at high concentrations. It should be mentioned again that the actual measurements only started after five minutes of recirculating polymer drag reducing flow through the loop. As a result, some degradation might have taken place. Although molecular weight and molecular weight distribution play a significant role in degradation (Gampert and Wagner, 1985), Superfloc A125V is commercially produced and its molecular weight and distribution of molecular weight is unknown. Comparison with other polymers at the same flow conditions and concentration is not enough.

The effect of polymer concentration on fanning friction factor is shown in Figure 4.4. The experimental data demonstrated in Figure 4.4 is based on the one-hour average pressure drop. The Reynolds number is defined based on the wall viscosity (μ_w) at the pipe wall ($Re_w = \rho U_b D/\mu_w$). The results showed that friction factor for the flow of water overlaps with Prandtl-Kaman equation in turbulent flow. It is also observed that deviations in friction factor for

polymer drag reducing flow from that of water increases with increasing polymer concentration. The relationship between the ratio of percentage of drag reduction to polymer concentration and polymer concentration is shown in Figure 4.5. It is observed that the ratio of percentage of drag reduction to polymer concentration decreases with increasing polymer concentration and the relationship between the ratio of percentage of drag reduction to polymer concentration and polymer concentration is not linear.

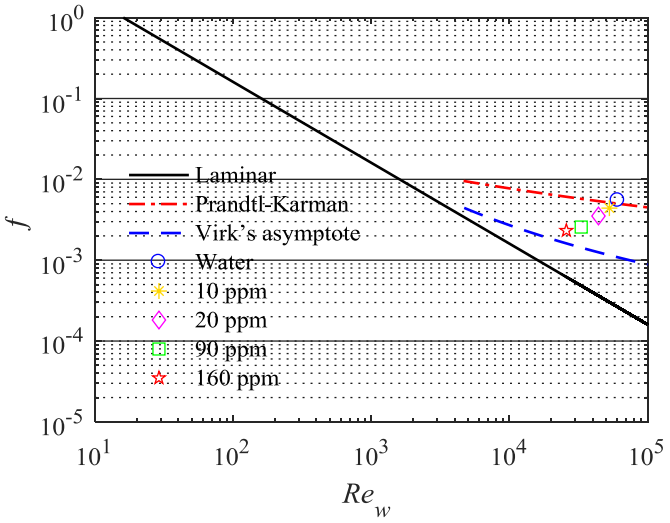

Figure 4.4. Effect of polymer concentration on Fanning friction factor. The three lines refer to Equations (4.5), (4.6), and (4.7).

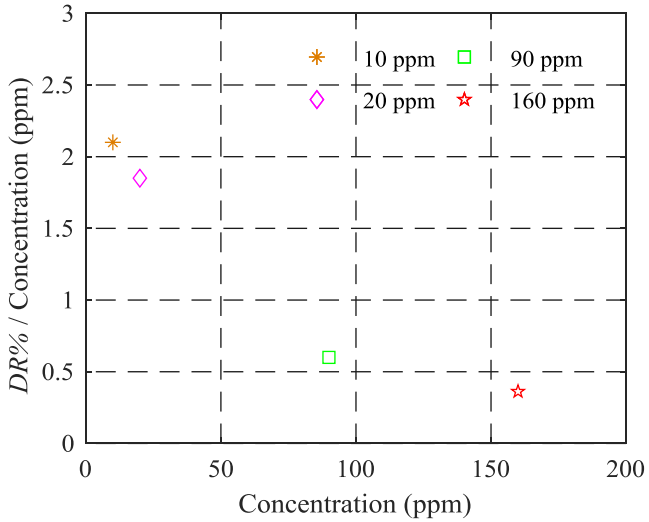

Figure 4.5. A ratio of percentage of drag reduction to polymer concentration versus polymer concentration.

4.2.2 Comparison between Moyno and the centrifugal pump

It has been well known since the earliest work by Toms (1948) that effectiveness of drag reduction decreases if the polymers in solution are subjected to high mechanical shear. In this section, the degradation of the polymer solution investigated in terms of comparing the Moyno and the centrifugal pump. The investigations were carried at constant flow rate 2.08 kg/s for both the Moyno and the centrifugal pump. Figure 4.6 shows the comparison between Moyno and the centrifugal pump in terms of drag reduction at two different polymer concentrations. As mentioned above, the data collection after five minutes of recirculating polymer drag reducing flow in the loop. The results showed that the most rapid degradation occurs in the centrifugal pump because of intense mechanical shear. It is also observed that the difference in the drag reduction between the Moyno and the centrifugal pump decreases with increasing polymer concentration. The one-hour average drag reduction for centrifugal pump is 35.62 % at 20 ppm while it increased to 43 % for Moyno pump. In case of 90 ppm, the difference in one-hour average drag reduction between Moyno and the centrifugal pump is 4.5 %.

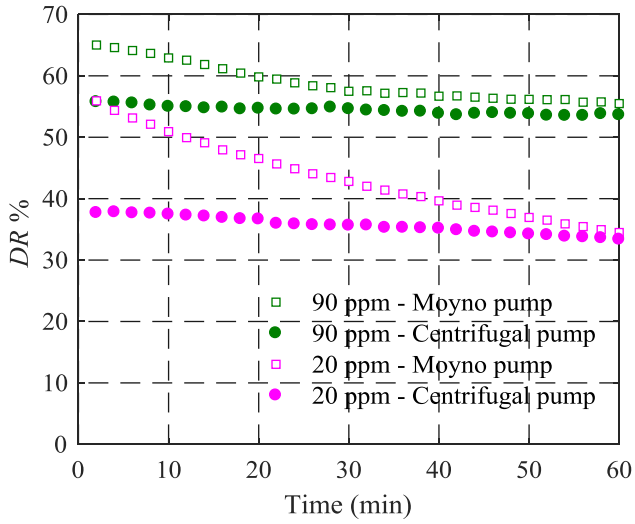

Figure 4.6. Comparison between Moyno and the centrifugal pump in terms of drag reduction

4.3 Conclusion

An increase in polymer concentration causes the degradation to decrease and drag reduction to increase until reaching a limit in drag reduction. It is clear that of the four different concentrations tested 90 ppm and 160 ppm are both most resistant to mechanical degradation and most effective in terms of drag reduction. It is also observed that the addition of long-chain polymers to flowing fluids increases pressure fluctuation range. The results of this experimental work also show that Moyno pump has less severe effect on mechanical degradation compared with centrifugal pump.

Chapter 5. Spatio-temporal structure of near-wall turbulence using time-resolved 2D-PIV

5.1 Introduction

Modification of turbulent statistics and structures due to the interaction of non-Newtonian fluid with turbulence can be the key to understanding the mechanism of polymer drag reduction. The literature on polymer drag reduction can be broadly divided into the following categories: turbulence statistics, turbulent structure and behavior of polymer molecules in turbulent flow. One of the earliest experimental investigations on the effects of polymer on the turbulence statistics was carried out by Virk *et al.* (1967). They used hot-film and Pitot tubes to measure streamwise velocity in pipe flow. Their work led to an empirical correlation with dilute solutions of a homologous series of linear, random-coiling polymers describing the maximum drag reduction (MDR), 'Virk's asymptote', that can be achieved in practice. The drawbacks of using hot film that it is an intrusive measuring device and polymer molecules can wrap around the sensors, which affects heat transfer especially in non-homogeneous drag reduction. In a later work, Virk (1975) also showed that the addition of polymer causes modification of the mean velocity profile.

With advances in instrumentation, Warholic *et al.* (1999) provided significant information on modifications of the statistical properties of turbulence in homogeneous polymer channel flow with laser Doppler velocimetry (LDV) measurements. For experiments at the same flow rate, the peak of the streamwise Reynolds stress normalized with friction velocity of the polymer solution increased for low drag reduction (DR $\leq$ 38%), while those peaks decreased to a level lower than observed in water for high drag reduction (DR $\geq$ 55%). A decrease in wall-normal Reynolds stress and Reynolds shear stress was also observed at low and high drag reduction. The Reynolds shear stress is close to zero and non-zero polymer stress over the whole cross section of the channel when the flows is at MDR. Escudier *et al*. (2009) also used LDV to study the turbulent structure in a fully-developed turbulent channel flow. They observed different trend at MDR, based on studies with polyacrylamide. The streamwise Reynolds stress

normalized with the friction velocity of the polymer solution increased to levels above that for water at the same Reynolds number which are contrary to the results obtained by Warholic *et al*. (1999) at MDR. The difference in these trends can be affected by the variation of friction velocity of the polymer solution.

Investigation of near-wall turbulent structure is important to understand the mechanism of the polymer drag reduction. Turbulent structure can be identified by conditional statistics or flow visualization techniques. Early flow visualizations in polymer drag-reducing flows were reported by Donohue *et al*. (1972) and Tiederman *et al*. (1985) in a fully developed two dimensional channel flow. Their results showed that the spanwise spacing of low-speed streaks significantly increases and the rate of bursting events decrease compared with that of the solvent alone. One of the first papers addressing the effect of polymers on the power spectrum of streamwise velocity fluctuation in pipe flow using one-dimension LDV measurements was carried out by Berman (1986). The results showed a redistribution of energy from high to low frequencies. In a more recent work, two-component LDV measurements were reported by Hoyer & Gyr (1996), Wei & Willmarth (1992) and Warholic *et al*. (1999). In other investigations, Warholic *et al*. (2001) employed particle image velocimetry in the *x*-*y* plane and in *x*-*z* plane to study effect of drag-reducing polymers on the turbulent structure in channel flow with a polymer injection system, which included power spectra of the streamwise and spanwise fluctuating velocity components.

The influence turbulent structure on the behaviour of polymer molecules is still the most difficult area of polymer flow phenomena. Lumley (1969, 1973) proposed that stretching of the molecules (coil-stretch transition) occurs outside of the viscous sublayer due to large fluctuating strain rates. This stretching of polymer molecules leads to an increase in effective (extensional or elongational) viscosity of the solution outside the viscous sublayer. Lumely argued that effective viscosity in viscous sublayer is essentially unchanged because polymer molecules are not expanded. Hinch (1977) supported this hypothesis by polymer elongation models. Hinch also suggested that the local effective viscosity increases with increase in stretching of random-coil molecules and the degree of stretching is associated with strain rate of the flow field. In contrast with Lumley's hypothesis, Tabor and de Gennes (1986) and de Gennes (1990) argued that random fluctuating of strain rate is not sufficient to increase extensional viscosity and

proposed a theory based on the elastic behavior of polymers (elastic theory). In their theory, polymer molecules can absorb some of the turbulent energy cascade from the flow at small scales and store it as elastic energy and then release this energy away from the wall.

The work presented in this section has been mainly motivated by including strain rate tensors along with the power spectra of the fluctuating velocity and strain rate. These investigations are at different layers in the near-wall region in channel flow with varying the percentage of drag reduction from low to maximum, using time-resolved 2D-PIV. The investigations of strain rate tensors are in the Lagrangian frame instead of Eulerian since polymer dynamics are intimately related to the Lagrangian frame (following the fluid element). With one exception (Warholic *et al.* 2001), in which particle-image velocimetry was used, previous measurements for power spectra in polymer drag reduction in channel flow have been made mainly using laser Doppler anemometry. In many previous works in turbulent channel flow, there is a limited information about flow rheology. Only Gampert *et al.* 2004; Warholic *et al*. 1999; and Escudier *et al*. 2009 provided viscosity shear rate curves in order to classify polymer solution degree of shear thinning.

5.2 Results and discussion

In this section, the turbulent data obtained from time-resolved 2D-PIV in *x*-*y* plane is used to study the structure in homogeneous channel flow with the addition of Superfloc A125v polymer. The turbulent structure near the wall, which is manifested as reduced drag, is investigated in dilute and shear thinning polymer solutions. The results of polymer solutions will be compared with that of water. DNS of turbulent water channel flow is also provided as a reference for comparison.

5.2.1 Mean velocity profile

Comparisons of measurements of mean streamwise velocity profiles $<U>$ normalized by the bulk velocity U_b near the wall for polymer drag reducing flows and water flow are presented in Figure 5.1 (a). There is a significant difference between polymer drag reducing flows and the corresponding Newtonian (water) flow. In the case of dilute polymer solutions (10 ppm and 20 ppm), the velocity profile of polymer drag reducing flow is similar to the profile of water. When rheological properties of polymer flow are changed into shear thinning at concentrations of 90 ppm and 160 ppm, the profile of polymer drag reducing flow lies between that of Newtonian turbulent flow and a laminar flow. However, the profile of shear thinning flow is still far away from the laminar flow. The velocity gradient ($d<U>/dy$) near the wall reduces with increasing polymer concentration and hence drag reduction potentially increases as polymer concentration increases until reaching maximum drag reduction. The velocity of water flow is higher than that of the polymer flow near the wall. The reduction in the velocity of polymer flow near the wall increases with increase of the polymer concentration. On the contrary, further away from the wall, the velocity of water is smaller than that of the polymer flow in order to maintain the same mass flow rate across the channel. The uncertainty is assumed to be 0.1 pix in the instantaneous velocity of PIV (Westerweel, 1997). The error in measurement of $<U>$ for water flow is 0.0112 m/s (0.19 $u_{\tau 0}$).

A semi-logarithmic plot of mean streamwise velocity profiles $<U>$ of each flow normalized with its corresponding friction velocity u_τ is presented in Figure 5.1 (b). The friction velocity u_τ=0.0589 m/s is estimated using Clauser's method (Clauser, 1954) which is confirmed by 3D-PTV measurements. The wall distance y is also normalized with the corresponding wall unit (λ).

As it is observed for water flow, the measured mean velocity profile is in agreement with law of the wall ($u^+=y^+$) and the von-Karman log law ($u^+ = 1/\kappa\ ln\ y + B$) with $\kappa = 0.389$ and $B = 5.5$. This agreement confirms that flow is fully developed. The comparison in viscous sublayer ($y^+ < 5$) show the profiles of polymeric flows and water flow data overlap. However, the viscous sublayer in polymeric flows extended beyond $y^+ = 7$. The vertical shift in the log-region and a thickening of the buffer layer increase with increasing polymer concentration. It is also noted that the slope of the logarithmic layer for the profiles of shear thinning flow increases but it remains parallel to that of the Newtonian flow in dilute polymer flows. The upward shift of the log-layer implies that the balance between the turbulent energy production and the viscous dissipation occurs away from the wall, and the smallest size of turbulent eddies near the wall increases. The profile of the 160 ppm flow reaches the maximum drag reduction asymptote ($U^+ = 11.7\ ln\ y^+ -17$) determined empirically by Virk *et al*. (1970).

(a) (b)

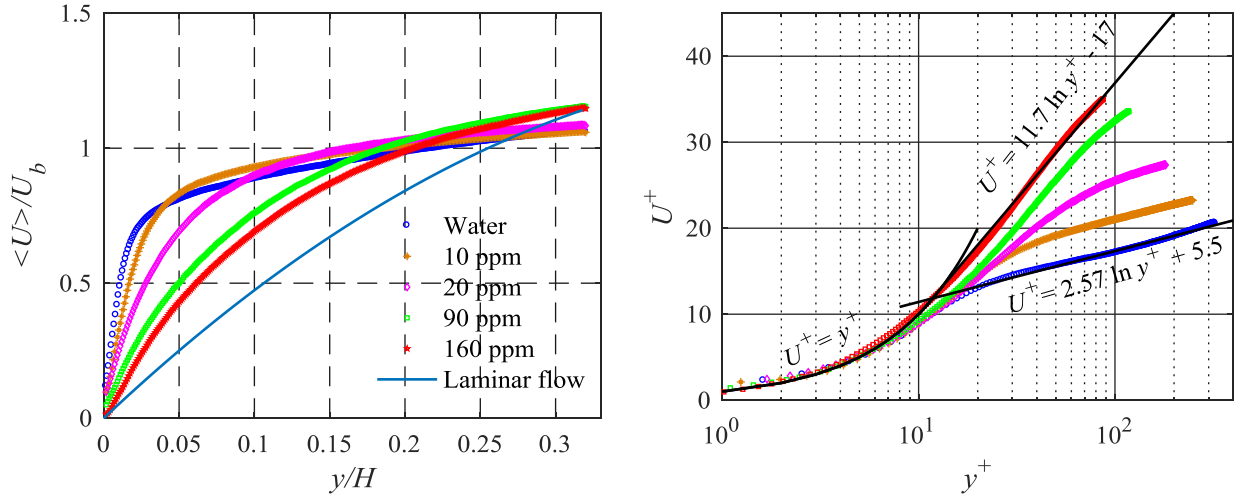

Figure 5.1. The effect of polymer concentration on the (a) mean streamwise velocity normalized by the bulk velocity as a function of the wall location normalized with channel height , and (b) mean streamwise velocity versus the distance from the wall normalized by the corresponding the inner scaling of flow. The law of the wall ($U^+=y^+$), log-law of Newtonian flows ($U^+=2.57\ln y^+ +5.5$), and Virk's asymptote ($U^+=11.7\ln y^+ -17$).

5.2.2 Reynolds stresses

The Profiles of Reynolds stress are normalized by the inner scaling of water ($u_{\tau 0}$) instead of that of the polymer solution to avoid variation of Reynolds stresses due to change in friction velocity at constant flow rate. The normalized profiles of streamwise Reynolds stress $<u^2>/u^2_{\tau 0}$ are shown in Figure 5.2 (a). The erroneous data points in the vicinity of the wall ($y_0^+ < 12$) which is associated with bias error of PIV have been removed to avoid any ambiguity. The biased error in the first few vectors near-wall results from the mirrored particle images, signal truncation and the glare of the laser light in the near wall interrogation windows (Theunissen *et al*., 2008). The results obtained from measurement in water flow at $Re_\tau = 507$ and $y_0^+ > 12$ are consistent with the DNS of fully developed channel flow by Moser *et al*. (2015) at $Re_\tau = 544$. The peak of normalized streamwise Reynolds stress in dilute polymer flows decreased and shifted towards the centre of the channel compared with the Newtonian fluid and this trend is more pronounced in shear thinning flows. The shift of the location of maximum streamwise Reynolds stress away from the wall corresponds to the tendency for increase in the thickness of the viscous sublayer and buffer region as observed in the semi-log plot of Figure 5.1 (b). The trend of peak values of $<u^2>/u^2_{\tau 0}$ in high drag reduction regime (DR > 40%) agrees with the results of Warholic *et al* (1999). The variation in the trend at low drag reduction is compared with results of Warholic *et al.*(1999) because the Reynolds stresses are normalized with friction velocity of water in this study as mentioned above.

The profiles of wall-normal Reynolds stress $<v^2>/u^2_{\tau 0}$ are presented in Figure 5.2 (b). The $<v^2>$ peak at 10 ppm reduces by 52.4% and the peak location is shifted away from the wall to $y_0^+ = 133$, relative to that of the water flow. However, when the polymer concentration is increased further or in other words for larger drag reduction, the reduction of $<v^2>$ profiles increases. Warholic *et al*. (1999) and Escudier *et al.* (2009) also reported these trends at low and high drag reduction. The largest reduction is observed at maximum drag reduction.

Normalized profiles of Reynolds shear stress $<uv>/u^2_{\tau 0}$ are shown in Figure 5.2 (c). The Reynolds shear stresses are reduced and in agreement with reductions of $<u^2>$ and $<v^2>$. The location of the peak moves continuously away from the wall with increasing polymer concentration in dilute polymer flows, whereas the value of $<uv>$ is close to zero in shear thinning polymer flows especially at MDR. This is consistent with previous experimental

observations (Warholic *et al*. 1999; Warholic *et al*. 2001). The error in the measurement of $\langle uv \rangle$ for water flow is 0.036 $u^2_{\tau 0}$ with the assumption of 0.1 pix uncertainty in the instantaneous velocity of PIV (Westerweel, 1997).

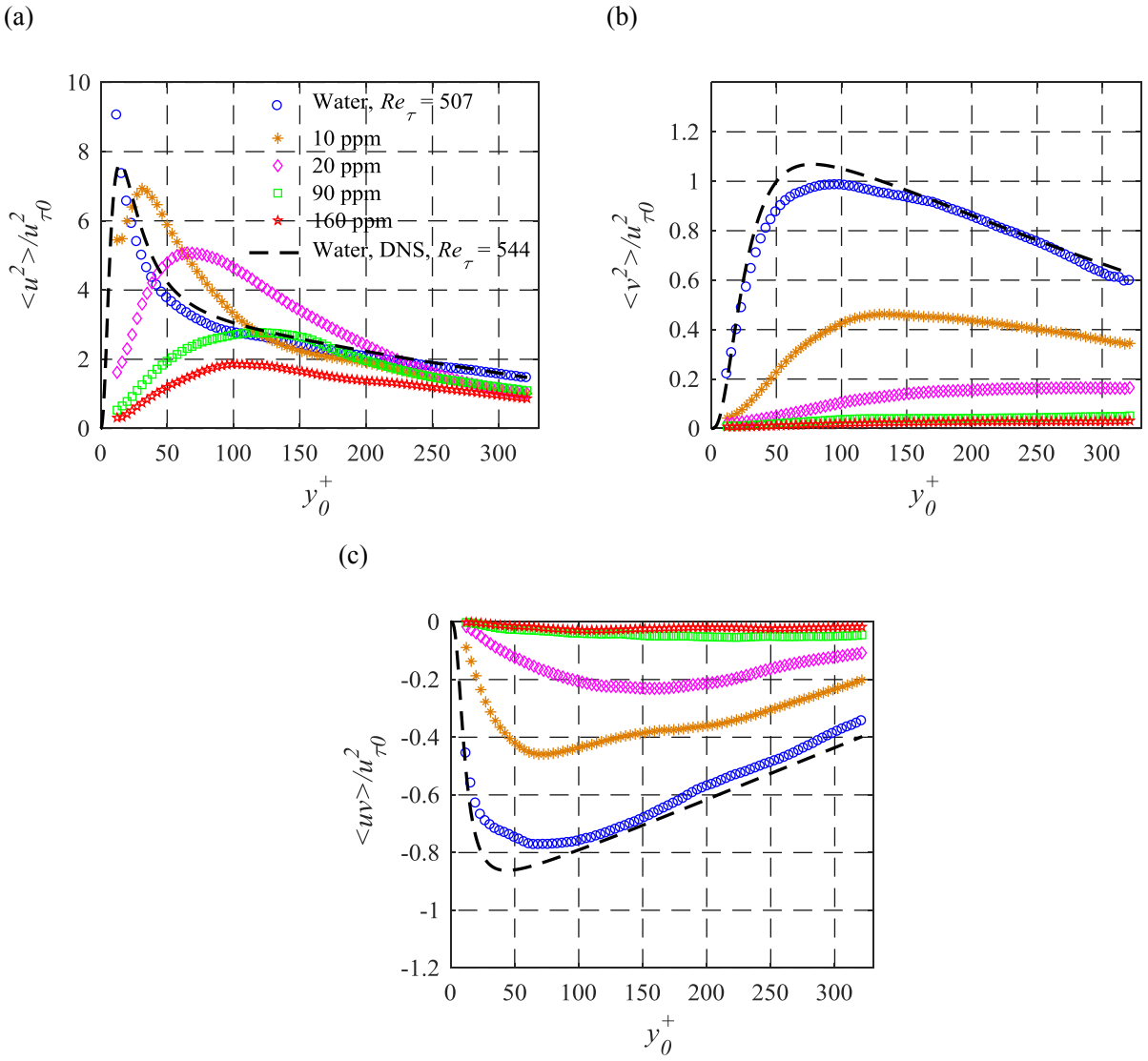

Figure 5.2. The effect of polymer concentration on the (a) streamwise and (b) wall-normal, and (c) shear Reynolds stresses normalized by the friction velocity of water ($u_{\tau 0}$).

5.2.3 Velocity power spectrum

The power spectral density (PSD) of the streamwise velocity fluctuations (u) at y_0^+= 16, and 145 for polymers and for water are compared in Figure 5.3(a) – 5.3 (b), respectively. The PSD is computed using Hanning window at frequency resolution of 100 Hz. The effective noise bandwidth (ENBW) is 150.94 Hz. The first location was chosen at y_0^+ = 16, which is in the region close to the peak of the streamwise Reynolds stress for water flow. The u-spectra at y_0^+= 16 shows that amplitudes for polymer drag reducing flows are much less than the corresponding Newtonian flow and the energy decreases with increasing drag reduction over the entire frequency range. The reduction of energy in the buffer layer is higher than that of log layer (y_0^+=145) in comparison with the Newtonian results. In case of shear thinning polymer flows or in other words at high drag reduction, a significant damping of relative contribution of high frequency fluctuations to the turbulence is observed which become more pronounced in the log layer. Figure 5.3 (c) and 5.3 (d) show the PSD of wall-normal velocity fluctuations (v) at y_0^+= 16, and 145, respectively. The v-spectra at y_0^+= 16 and 145 are suppressed at low and high frequency. The suppression of energy is more drastic at high frequency.

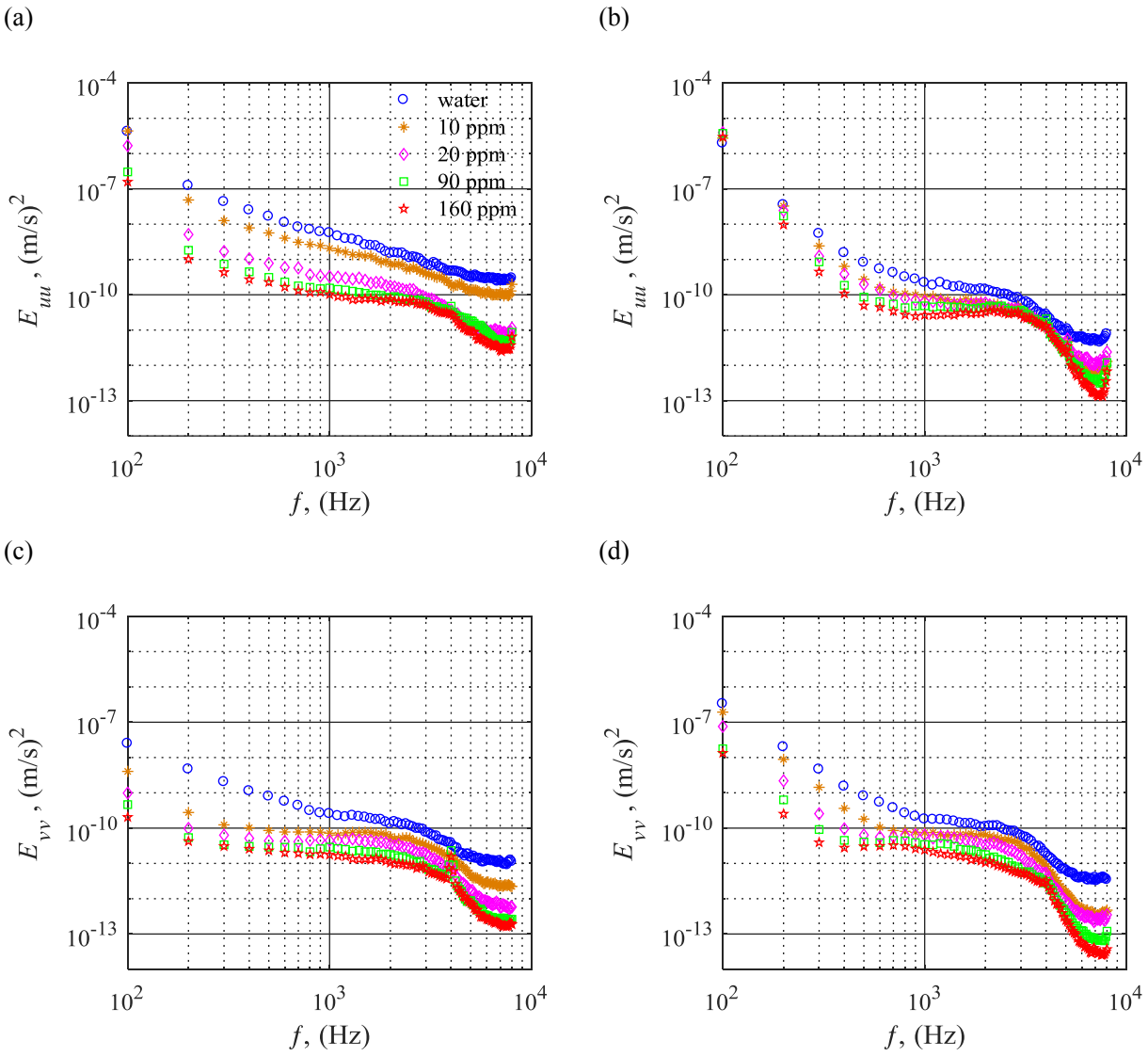

Figure 5.3. The PSD of (a and b) streamwise velocity fluctuation and (c and d) wall-normal velocity fluctuation. Two wall-normal locations of y_0^+ =16 (a, c), and y_0^+ =145 (b, d) are shown.

5.2.4 The strain field

The turbulent strain-rate plays significant role in polymer drag reduction which is believed to play an essential role in stretching of polymers. The deformation of polymers depend strongly on the nature of flow (de Gennes 1974; Smith *et al*., 1999; Babcock, 2000; Dua A & Cherayil BJ 2003). Flows in many practical applications consist of a mixture of both rotational and elongational components. In case of pure elongation flow, it is expected that significant changes occur in the polymer chain. In pure rotational flow, on the other hand, polymer chain will be rotated without inducing deformation. Therefore, the deformation of the polymer molecules depend on the relative magnitudes of strain rate and rotation (Lumley , 1969 ; Dua A, 2010; Smith *et al*., 1999).

5.2.4.1 Streamwise strain rate

The effect of polymer concentration on turbulent strain-rate is investigated using probability density function (PDF) at three different wall-normal locations. The results of streamwise strain rate (S_{11}) from the Lagrangian method are shown in Figure 5.4 (a,c and e). The streamwise strain rate is defined as

$$S_{11}=\frac{\partial U}{\partial x} \tag{5.1}$$

The PDF profiles of streamwise strain rate at three different wall-normal locations show symmetric distribution around zero strain rate. This means that polymer chains are subjected to stretching and compression. Positive strain values describe stretching and negative values are when the element of fluid is being compressed. The role of compression of molecules is at least as important as their stretching since both contribute to the extensional viscosity. In case of uniaxial elongation, the stretching of a polymer chain occurs in the principle direction whereas compressing occurs in the other orthogonal directions. If the flow is a biaxial elongation flow, a polymer chain will be simultaneously stretched in two directions and compressed in the third direction (squeezing) (Den Toonder *et al*., 1995). The investigation of this chapter is limited to two directions.

In the region close to the wall (y_0^+ =16), shown in Figure 5.4 (a), the profile of the streamwise strain rate for polymeric flow become sharper and narrower with increasing polymer

concertation. This means that turbulent fluctuations of the streamwise strain rate are absorbed by coiling polymer chains to be unraveled (flexible polymers) in the principle strain rate direction. The PDF profiles of streamwise strain rate at $y_0^+ = 27$ are presented in Figure 5.4 (c). The fluctuation range of streamwise strain rate of water decreased to ±2000 s^{-1} and the difference among the PDF profiles of polymer solutions (20, 90 and 160 ppm) is more pronounced at $y_0^+ = 27$. Further away from the wall ($y_0^+ = 145$), the PDF profile of water becomes narrower with a larger peak. It is observed that range of the rate of streamwise strain rate fluctuation for water is reduced to half compared with that at $y_0^+ = 27$. Due to low fluctuations in streamwise strain rate of water, the difference between water and polymeric flows is not as large as that in the buffer layer ($y_0^+ = 16$ and 27). It should be also noted that the difference between 10 ppm and the other polymeric flows is small compared to that in the buffer layer ($y_0^+ = 16$ and 27). This also implies that weak fluctuations and a small number of strong fluctuations in log layer is not adequate to stretch all polymer chains at higher concentrations. The finding of a substantial suppression of turbulent strain-rate fluctuations in the buffer layer ($y_0^+ = 16$ and 27) compared with log layer are consistent with the large reduction of Reynolds stresses in the buffer region. The reason for this is that strain rate fluctuations in the log layer is small compared with the buffer layer. An increase in the number of stretched molecules results in greater increase in local extensional viscosity. Therefore, polymers are more effective in the buffer layer. The results of streamwise strain rate from Eulerian method are presented in Figure 5.4 (b,d and f).The PDF profiles for water and polymeric flows are slightly narrower than in the Lagrangian method. This demonstrates that fluctuation are stronger along the Lagrangian trajectory.

The PSD profiles of streamwise strain rate at three different wall-normal locations from Lagrangian method are shown in Figure 5.5 (a, c and e). The S_{11}-spectra at $y_0^+ = 16$ shows that reduction in energy intensity increases as drag reduction increases. In case of dilute polymer solutions, the slope of PSD profiles increases at high frequency. In concentrated polymer solution, on the other hand, the slope of PSD profiles decreases with increasing drag reduction. The results also showed that the PSD profiles for 20, 90 and 160 ppm overlap between 800 to 1250 Hz. At $y_0^+ = 27$, shown in Figure 5.5 (c), the S_{11}-spectra for polymeric flow decreases as drag reduction increases and the spectral intensity remains constant at low frequency while there is a slight increase at high frequency. The magnitude of reduction in energy for polymeric flows

is small in the log layer compared with those in the viscous sublayer as shown in Figure 5.5 (e). It is also noted that spectral intensity is almost the same for 10, 20 and 90 ppm. The amplitude of spectrum for 160 ppm showed the largest suppression. The results from the Eulerian method show contrary trends compared with the Lagrangian method at high frequency as shown in Figure 5.5 (b,d and f). This can be associated with a small change in the magnitude of fluctuation between the pair of images while the magnitude of fluctuation is large along the Lagrangian trajectory between two consecutive locations of fluid parcel. The spectral intensity of streamwise strain rate fluctuations significantly decreases at high frequency and the cut-off frequency of polymeric flow decreases with increasing polymer concentration in the viscous sublayer while they have similar cut-off frequency (2 kHz) at log layer.

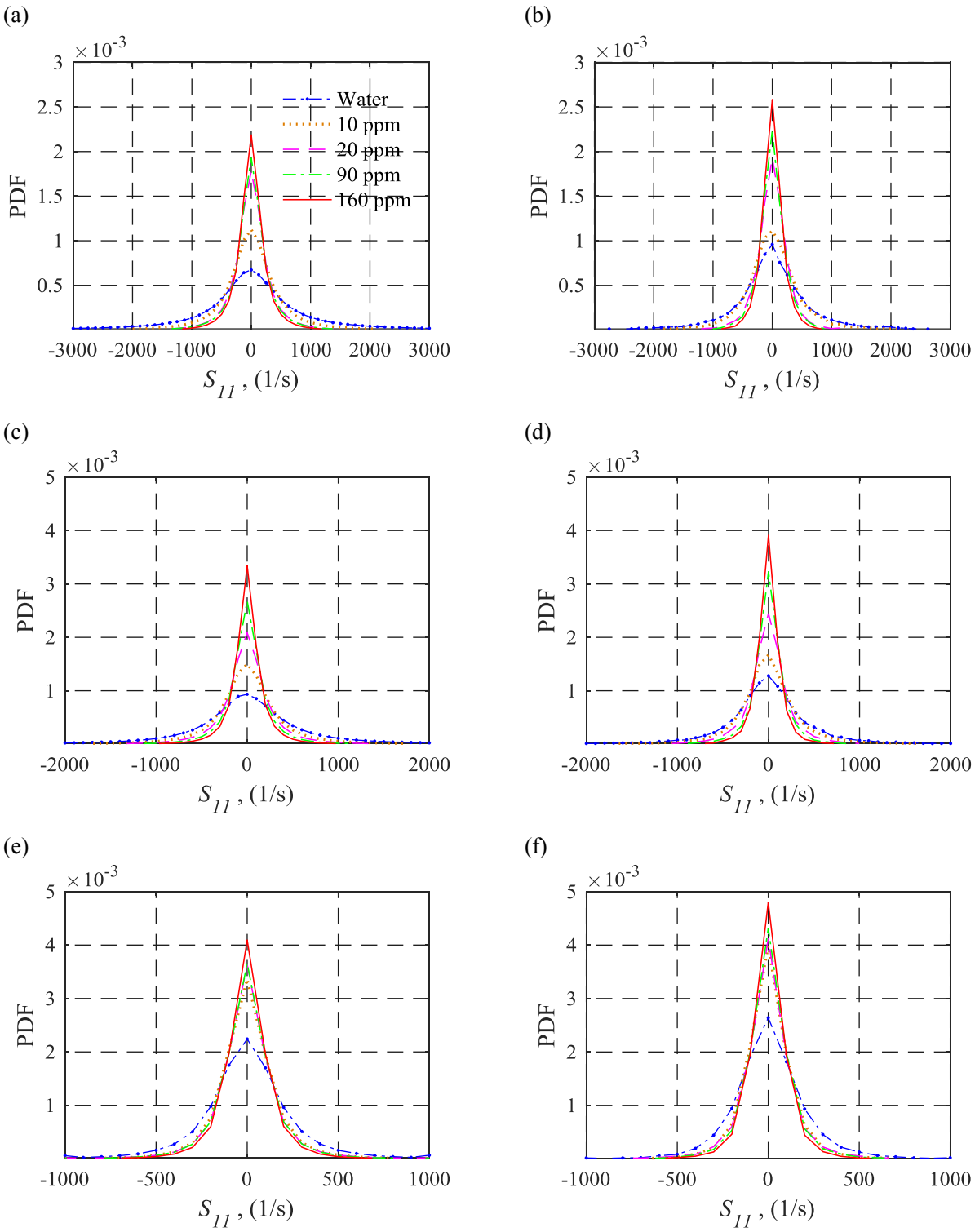

Figure 5.4. The PDF of streamwise strain rate in Lagrangian method (a,c, and e) and Eulerian method (b,d, and f) for the water flow and the four polymer cases. Three wall-normal locations of y_0^+ =16 (a, b), y_0^+ =27 (c, d), and y_0^+ =145 (e, f) are shown.

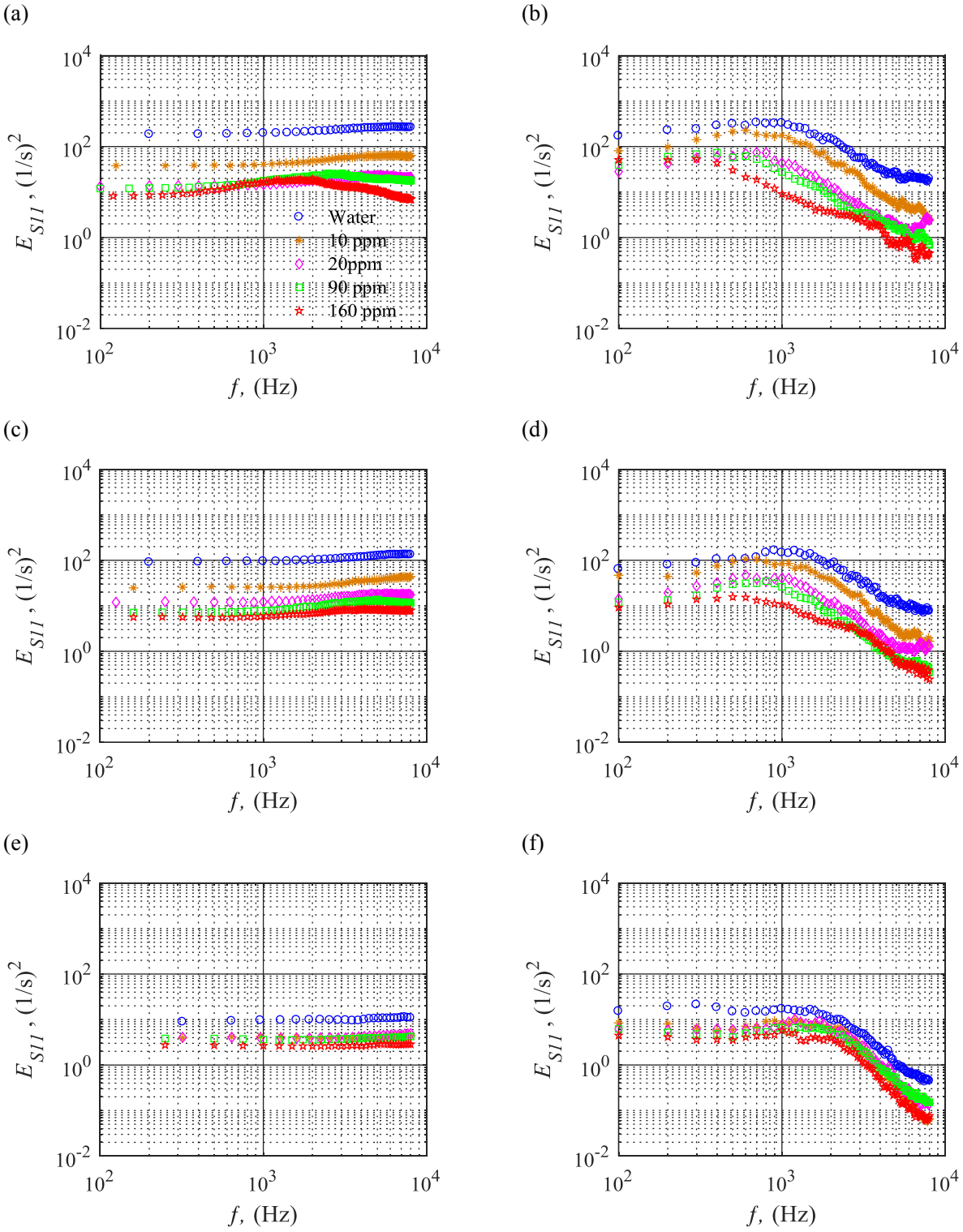

Figure 5.5. The PSD of the streamwise strain rate fluctuations in Lagrangian method (a,c, and e) and Eulerian method (b,d, and f) for the water flow and the four polymer cases. Three wall-normal locations of y_0^+ =16 (a, b), y_0^+ =27 (c, d), and y_0^+ =145 (e, f) are shown.

5.2.4.2 Wall-normal strain rate

The PDF of wall-normal strain rate (S_{22}) from Lagrangian method at three different wall-normal locations are shown in Figure 5.6 (a,c and e). The streamwise strain rate is defined as

$$S_{22}=\frac{\partial V}{\partial y} \tag{5.2}$$

The results show that a decrease strain rate fluctuations increases with increasing polymer concentration. Almost similar trends and magnitudes are observed at three different wall-normal locations. Generally, as can be seen in Figure 5.6 (a,c and e), polymer chains are subject to smaller stretch and compression in the wall-normal direction than the streamwise direction at y_0^+ =16 and 27. However, it is obvious that the fluctuation range of wall-normal strain rate of water is adequate to stretch polymers since there is reduction in the fluctuations in the polymeric flows.

The range of wall-normal strain rate of water at three different wall-normal locations is almost the same as that of streamwise strain rate of water at the log layer. However, there are clear variations among PDF profiles of wall-normal strain rate for polymeric flows while the PDF profiles of streamwise strain rate for polymeric flows (10, 20 and 90 ppm) are almost identical. This might be due to polymer chain alignment in streamwise direction, which have more resistance to strain rate fluctuation than monomers. Figure 5.6 (b,d and f) show PDF profiles of the wall-normal strain rate from the Eulerian method at three different wall-normal locations. It is observed that the PDF profiles from Eulerian method are slightly sharper than in the Lagrangian method implying lower fluctuations range in Eulerian method.

The PSD profiles of wall-normal strain rate fluctuations for water and polymeric flows from the Lagrangian method at three different wall-normal locations are presented in Figure 5.7 (a,c and e). The amplitude spectrum of S_{22} for polymeric flows are reduced and the reduction increases with increasing drag reduction. The results also showed that PSD profiles for polymer solutions remain almost constant and parallel to the flow of water throughout the entire frequency range at three different wall-normal locations. It should be noted that the difference in S_{22}–spectra between polymer solutions increases as the distance from the wall increases. The results from the Eulerian method, shown in Figure 5.7 (b,d and f), are contrary to the observations obtained from Lagrangian method. The PSD of water and polymeric flow is not

constant over the entire frequency range. A significant reduction in S_{22}–spectra at high frequency is observed.

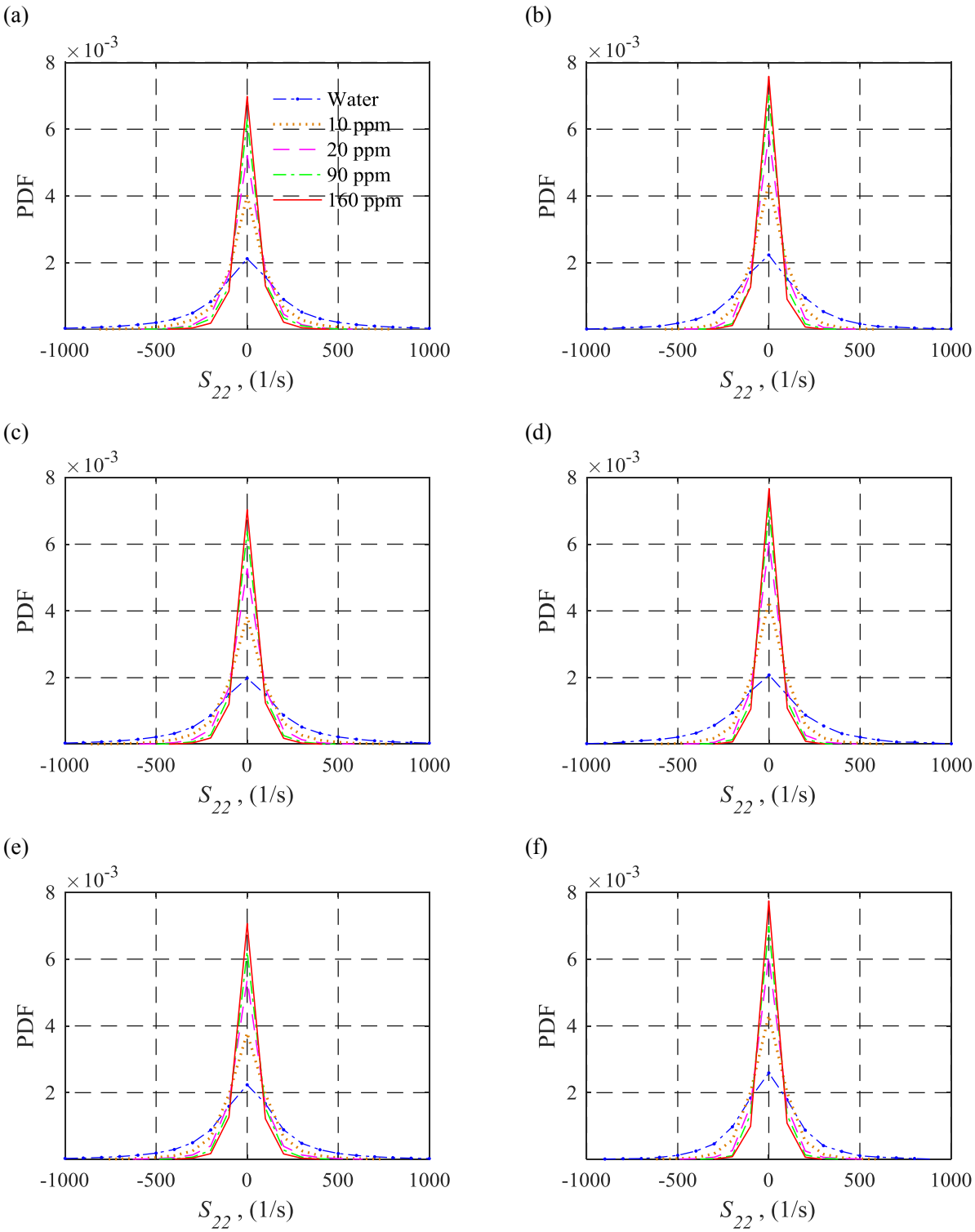

Figure 5.6. The PDF of wall-normal strain rate in Lagrangian method (a,c, and e) and Eulerian method (b,d, and f) for the water flow and the four polymer cases. Three wall-normal locations of y_0^+ =16 (a, b), y_0^+ =27 (c, d), and y_0^+ =145 (e, f) are shown.

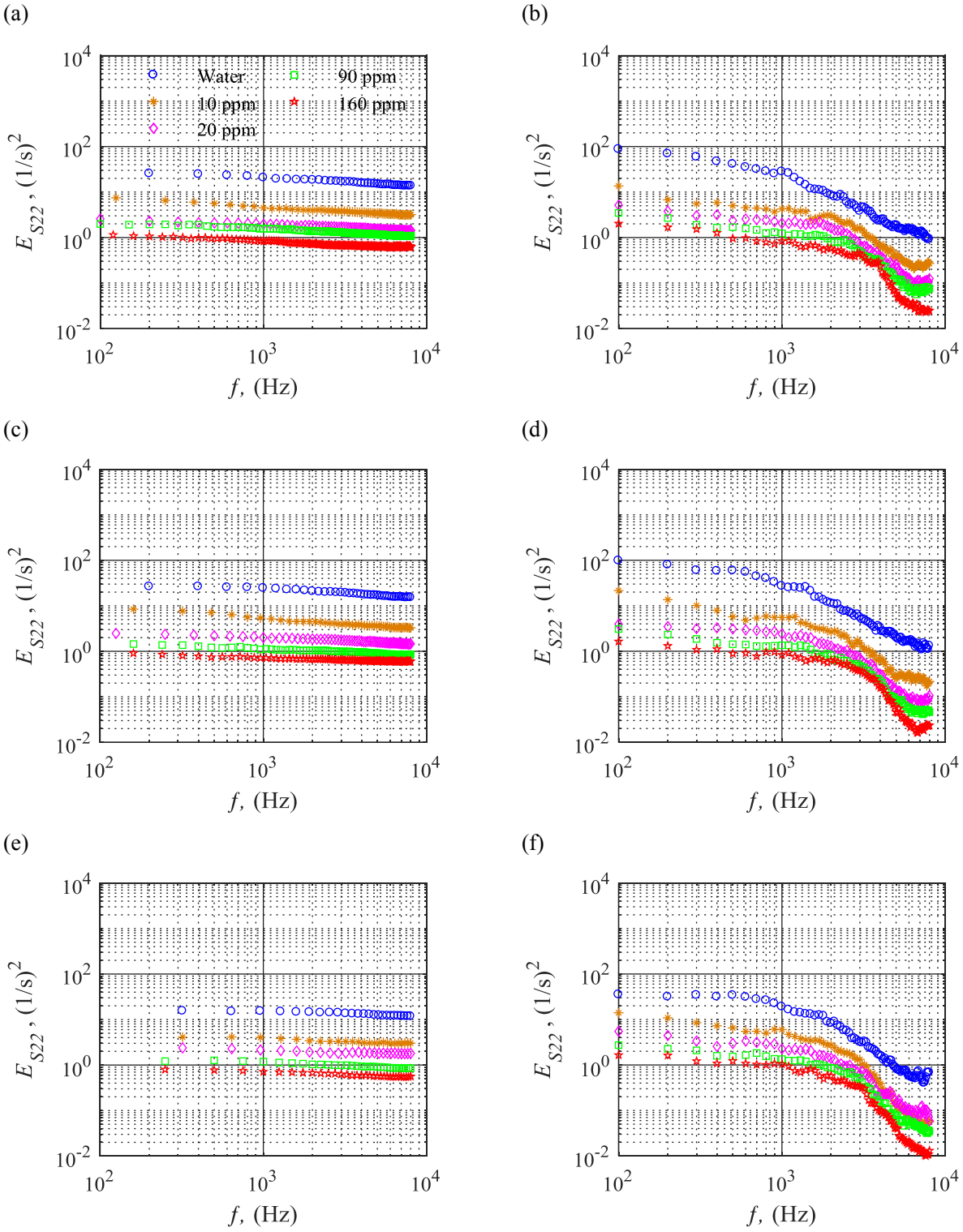

Figure 5.7. The PSD of the wall-normal strain rate fluctuations in Lagrangian method (a,c, and e) and Eulerian method (b,d, and f) for the water flow and the four polymer cases. Three wall-normal locations of y_0^+ =16 (a, b), y_0^+ =27 (c, d), and y_0^+ =145 (e, f) are shown.

5.2.4.3 Shear rate

Occurrence of shear flow next to extensional flow is investigated through shear rate (S_{12}). The PDF profiles of shear rate from the Lagrangian method at three different wall-normal locations are illustrated in Figure 5.8 (a, c and e).). The shear strain rate is defined as

$$S_{12}=\frac{\partial U}{\partial y}+\frac{\partial V}{\partial x} \tag{5.3}$$

In the vicinity of the wall (y_0^+ =16), the location of the peak of the PDF profile for 10 and 20 ppm is shifted to higher a strain rate compared with water, and the location of the peak for 90 ppm is almost the same as that of water. The location of the peak for 160 ppm, on the other hand, is shifted to a lower strain rate compared to water flow. In comparison with the PDF profile of water, it is important to note that all PDF profiles of polymeric flows are shifted to the positive side. This implies that polymer chains are significantly subject to stretching more than compression. The PDF profile of polymer solution becomes sharper and narrower with increasing polymer concentration, which indicates a larger number of weak fluctuations and a smaller number of strong fluctuations.

The PDF profiles of shear rate for water and polymer solutions at y_0^+ = 27 are presented in Figure 5.8 (c). The positive range of PDF profile for water flow reduces to 2000 s^{-1}, reflecting a decrease in positive fluctuations (stretching). The location of the peak for 20, 90 and 160 ppm is almost the same at 400 s^{-1} while the PDF peak location for 10 ppm is shifted to 450 s^{-1} and the PDF peak location for water is less than any of the polymeric flows.

Further away from the wall (y_0^+ =145), shown in Figure 5.8 (e), the location of maximum probability for the polymeric flow shifts to higher value in the positive side as polymer concentration increases, which is contrary to observations at y_0^+ =16. The PDF profiles of water and polymer solutions show an asymmetric distribution at three different wall-normal locations and the PDF profile of polymeric flows become closer to a symmetric distribution with increasing polymer concentration.

It is observed that the location of maximum probability for the dilute polymer solutions (10 and 20 ppm) is higher than that of water at y_0^+ =16 and 27, while they have almost the same peak location in the log layer. It should be noted that positive range of shear rate (stretching) for

flow significantly decreases as the distance from the wall increases while there is a slight decrease in the negative range of shear rate (comparison) with increasing distance from the wall. As a result, the polymer chains are subjected to higher compression in the log layer than the buffer layer (y_0^+ =16 and 27). The results of shear strain rate from the Eulerian method are shown in Figure 5.8 (b,d and f). The PDF profiles for water and polymeric flows are narrower than in Lagrangian method. This implies that fluctuations are weaker in Eulerian method compared with Lagrangian method.

The power spectral density of the strain rate fluctuations from Lagrangian method are also computed at same the wall-normal locations as shown in Figure 5.9 (a,c and e). Figure 5.9(a) shows the PSD of the strain rate fluctuations at y_0^+ =16. As drag reduction increases, the energy of the strain rate fluctuations (S_{12}) suppresses compared with Newtonian flow. It is observed that the rate of reduction of energy is small at low frequency, while it is large at higher frequency. A different trend is observed at y_0^+ =27 as shown in Figure 5.9 (c). The slope of PSD for the profiles of polymer solutions significantly decreases at low frequency but they have a small slop at high frequency. At y_0^+ =145, shown in Figure 5.9 (e), the difference between water and polymeric flows is very small at low frequency while the difference increases as the frequency increases. It is also noted that the spectral intensity remains roughly constant for polymeric flows at very high frequency. The result from the Eulerian method show different trend as shown in Figure 5.9 (b,d and f). The addition of polymer decreases the energy at high frequencies relative to those at lower frequencies and this effect increases as the distance from the wall increases.

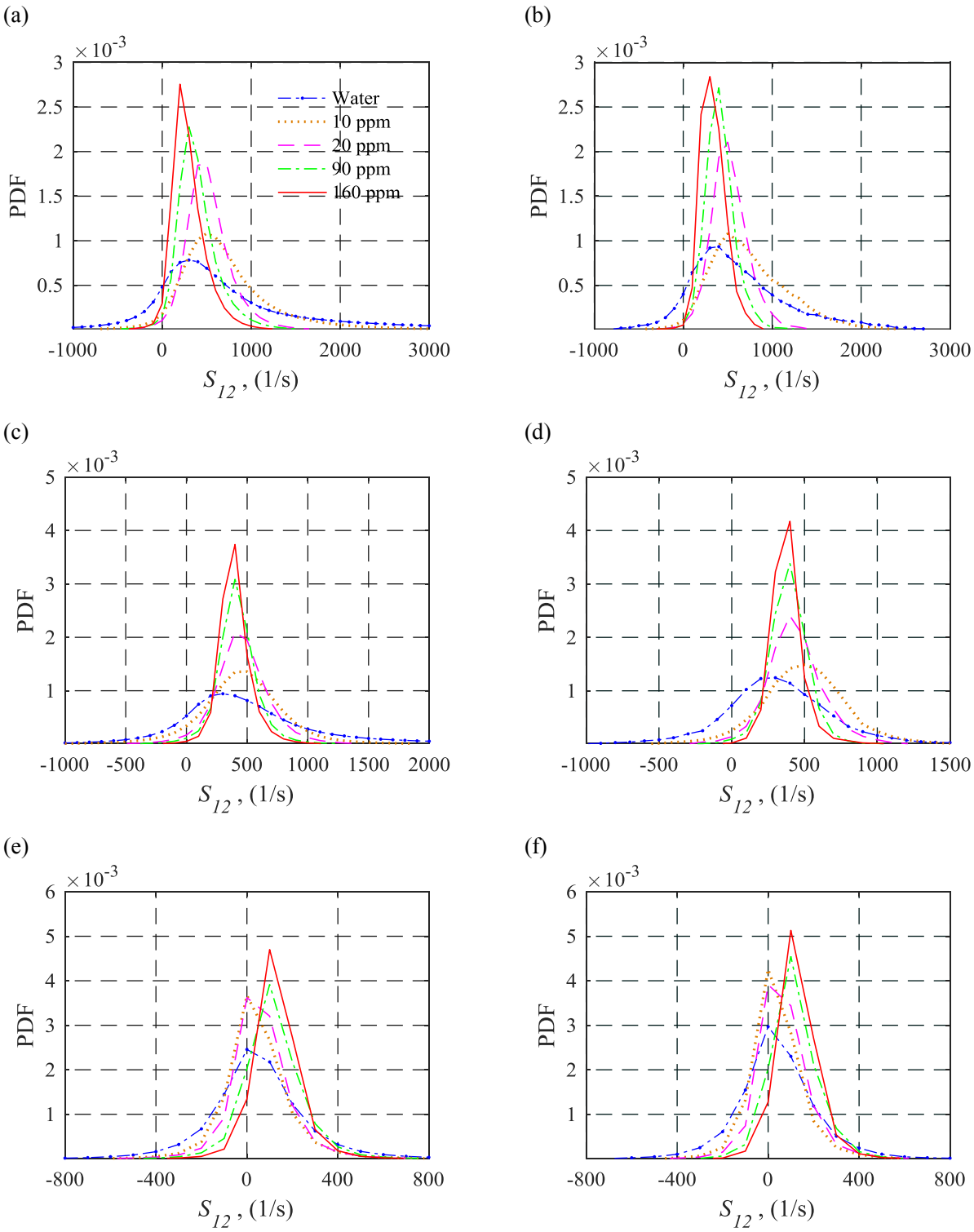

Figure 5.8 The PDF of shear rate in Lagrangian method (a,c, and e) and Eulerian method (b,d, and f) for the water flow and the four polymer cases. Three wall-normal locations of y_0^+ =16 (a, b), y_0^+ =27 (c, d), and y_0^+ =145 (e, f) are shown.

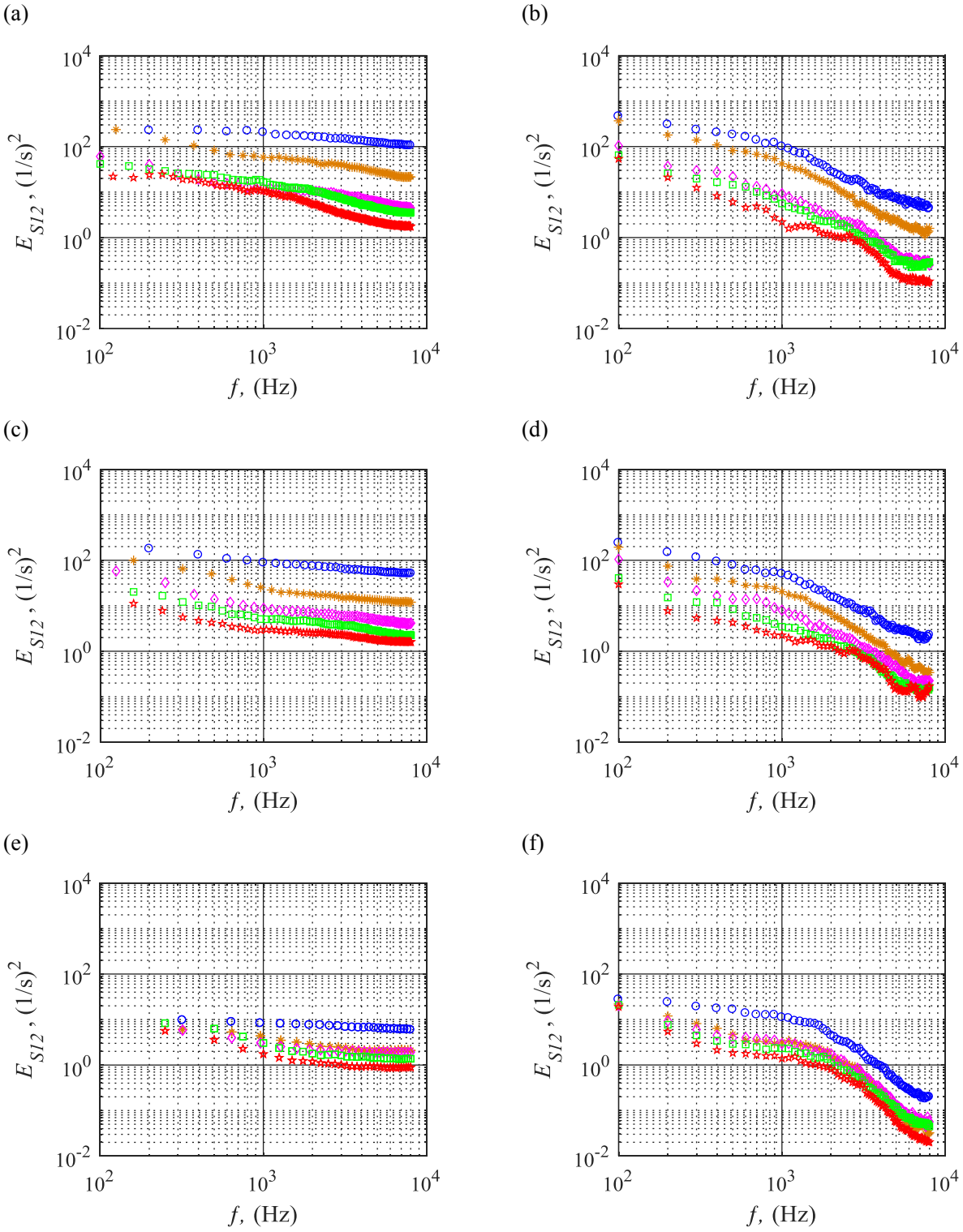

Figure 5.9. The PSD of the shear rate fluctuations in Lagrangian method (a,c, and e) and Eulerian method (b,d, and f) for the water flow and the four polymer cases. Three wall-normal locations of y_0^+ =16 (a, b), y_0^+ =27 (c, d), and y_0^+ =145 (e, f) are shown.

5.2.5 Quadrants of velocity fluctuations

The contribution of ejection (quadrant 2) and sweep (quadrant 4) motions to the total turbulence production is investigated using conditional averaging of Reynolds stress, following Willmarth and Lu (1972). The first quadrant ($u > 0$ and $v > 0$) is associated with motion of high-speed fluid toward the center of the flow field. The second quadrant ($u < 0$ and $v > 0$) represents the events corresponding to the low-speed fluid moves toward the center of the flow field (ejection). The third quadrant, where ($u < 0$ and $v < 0$), show inward motions of low speed fluid. The fourth quadrant ($u > 0$ and $v < 0$) represents the events in which high-speed fluid moves toward the wall (sweep). The second and fourth quadrant events (*uvQ*2 & *uvQ*4) contribute to positive turbulence production (negative Reynolds shear stress) and the first and third quadrant events (*uvQ*1 & *uvQ*3) contribute to negative turbulence production (positive Reynolds shear stress) (Pollard *et al*., 2016).

The results of conditional averaging of the *uvQ*1are presented in Figure 5.10 (a) for water and the polymer solutions. In the near wall region ($y_0^+ < 20$), a significant reduction of the *uvQ*1 is observed at high polymer concentrations. The peak value of *uvQ*1 in polymeric flows moves away from the wall compared with the Newtonian fluid. Generally, the profiles of *uvQ*1 in polymeric flows (20, 90 and 160 ppm) decreased near the wall and increased away from the wall. Figure 5.10 (b) shows that intensity of ejection motions (*uvQ*2) decreases with increasing polymer concentration. This implies that turbulence production due to ejection is reduced. The location of the peak moves continuously away from the wall with increasing polymer concentration in dilute polymer flows, whereas the peak almost vanished for 90 and 160 ppm. A similar trend is observed for *uvQ*3 as shown in Figure 5.10 (c). The conditional average of the *uvQ*4 in Figure 5.10 (d) shows the contribution of sweep motions to turbulence production. The *uvQ*2 events dominate the turbulence production away from the wall ($y_0^+ >14$). In the vicinity of the wall ($y_0^+ <14$), the *uvQ*4 events (sweeps) are dominated which is in agreement with Kim *et al* .(1987). The profiles of *uvQ*4 for polymeric flows are reduced and the intensity of sweep motions decreases with increasing polymer concentration.

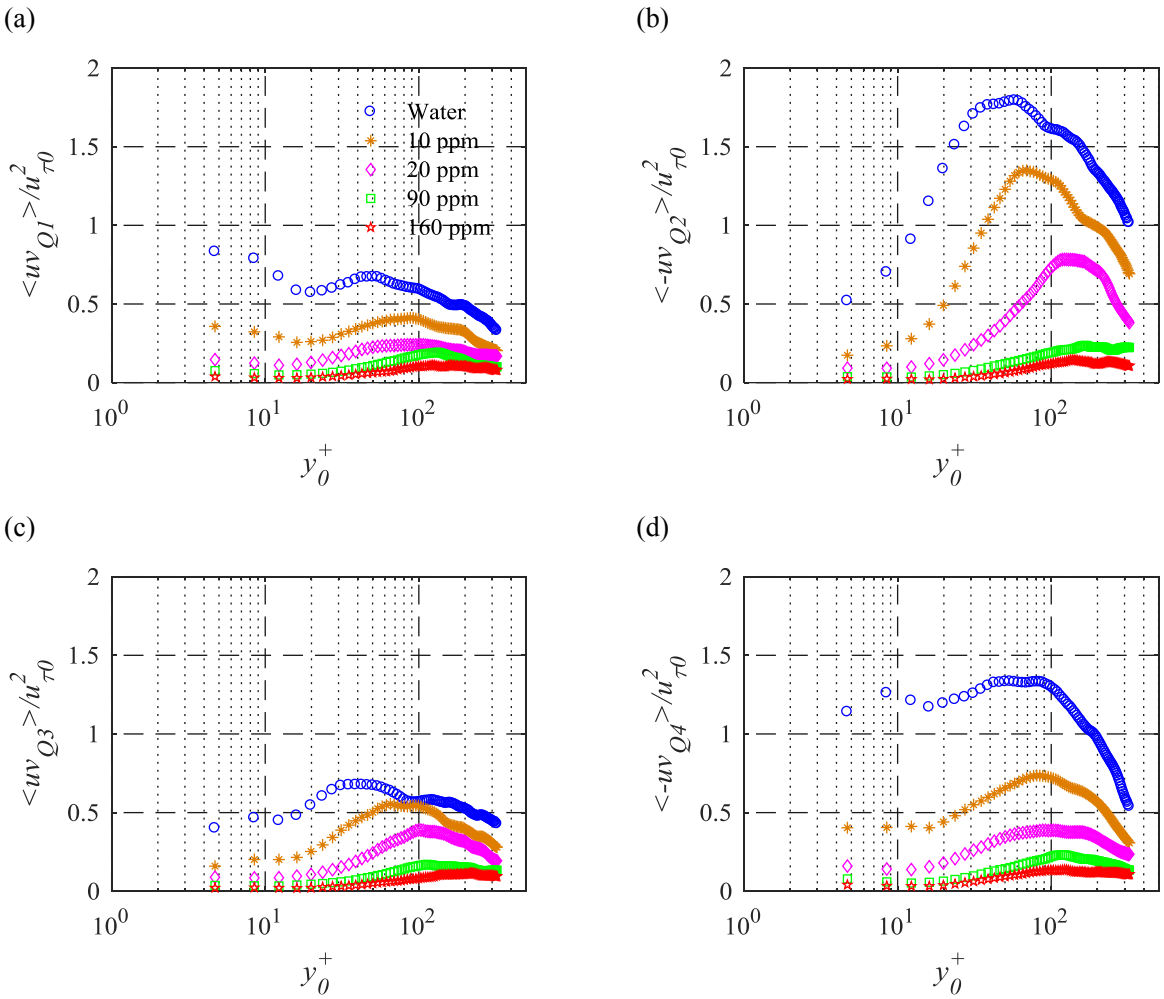

Figure 5.10. Evaluation of the conditional averages of the four quadrants (a) *uvQ*1, (b) *uvQ*2, (c) *uvQ*3, and (d) *uvQ*4.

5.2.6 Vorticity and eddy diffusivity of momentum

The variation of the normalized spanwise root-mean-square of vorticity fluctuation with polymer concentration is shown in Figure 5.11. DNS data at Re_τ = 530 is also provided for comparison (Min *et al*. 2003). A least squares is applied in order to reduce the measurement noise for calculating the velocity gradients (Raffel *et al*., 2007). The profile of normalized spanwise root-mean-square of vorticity fluctuation for 10 ppm is slightly smaller near the wall. As polymer concentration increases, the normalized spanwise root-mean-square of vorticity fluctuation decreases. Further away from the wall (y_0^+ >200), the normalized spanwise root-mean-square of vorticity fluctuation for polymer solutions overlap with each other.

The eddy diffusivity of momentum is defined as (Fu *et al*., 2014; Sugioka *et al*., 2015)

$$\epsilon_t = \frac{-\langle uv \rangle}{\partial \langle U \rangle / \partial y} \tag{5.1}$$

The effect of polymer concentration on eddy diffusivity of momentum is presented in Figure 5.12. The eddy diffusivity of momentum obtained for 10 ppm is found to slightly decrease far away from the wall (y_0^+ > 225) when compared with the water flow. The eddy diffusivity of momentum decreases dramatically for shear thinning polymeric flows over the wall-normal distance, which implies that 90 and 160 ppm have an important effect on suppression of momentum transfer.

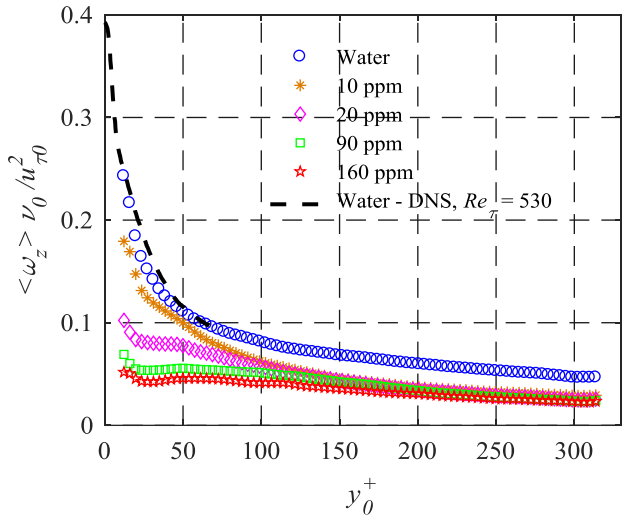

Figure 5.11. Spanwise root mean square vorticity fluctuation from PIV measurement normalized using $u_{\tau 0}$ and v_0 of water. The DNS data for Newtonian channel flow by Min *et al.* (2003) at $Re\tau = 530$ is presented for comparison.

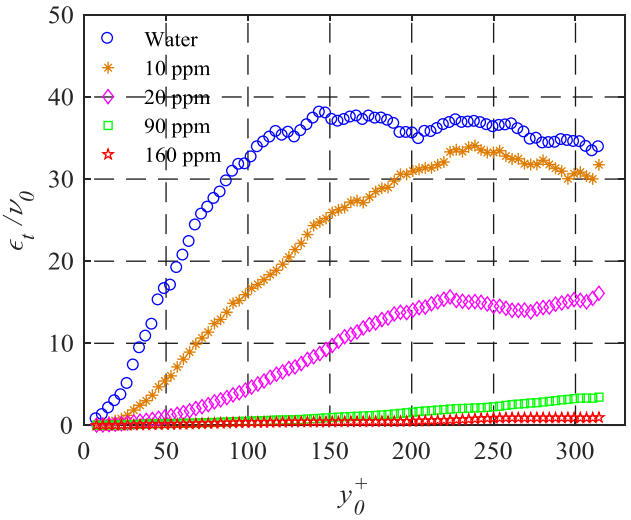

Figure 5.12. The effect of polymer concentration on eddy diffusivity of momentum normalized using kinematic viscosity of water (v_0).

5.3 Conclusion

Turbulent flow for Newtonian and non-Newtonian flow is experimentally investigated. Flow characteristics are measured using time resolved planar PIV over a streamwise/wall-normal plane. The addition of polymer (Superfloc A-125V) to water at different concentrations resulted in significant changes in the turbulent structures.

The investigations of the present chapter show that the log layer for dilute polymer solutions (10 and 20 ppm) shifts upward parallel to Newtonian flow while the slope of the logarithmic layer for concentrated polymer solution flows (90 and 160 ppm) increases until the profile reaches the MDR at concentration of 160 ppm. This implies that turbulence production is balanced by the viscous dissipation of turbulent at a location further away from the wall. At maximum drag reduction, following Virk's asymptote, logarithmic layer is disappeared and the largest thicknesses of the viscous and buffer layers are observed. The thickness of the buffer layer increases with increasing polymer concentration, which is consistent with increase of extensional viscosity with increase of concentration.

The profiles of streamwise and wall-normal Reynolds stresses, and also Reynolds shear stresses for polymeric flow attenuates as drag reduction increases. The peak location of streamwise Reynolds stress shifts continuously away from the wall with increasing polymer concentration which corresponds to an increase in the thickness of the viscous and buffer layers. It should be noted that Reynolds shear stress is almost at zero level at maximum drag reduction. Investigation of the quadrants of velocity fluctuations showed that the sweep and ejection events are significantly suppressed in polymeric flows reflecting a reduction of turbulence production. In the vicinity of the wall, the profile of spanwise root-mean-square of vorticity fluctuation decreased with increasing polymer concentration. However, further away from the wall, all the profiles for polymeric flows overlapped. The profiles of eddy diffusivity of momentum for concentrated polymeric are significantly suppressed implying reduction of momentum transfer.

The Lagrangian method showed an advantage over the Eulerian method. The polymer molecules are subject to higher deformation along the trajectory than that observed in Eulerian method. In case of elongational deformation from Lagrangian method, both S_{11} and S_{22}

contribute to stretching and compression of the polymers. The distributions suggests that a significant stretching of the polymer chains is in the streamwise direction. The PDF profiles of wall-normal strain rate show similar trends in the buffer and log layer while those of streamwise strain rate reveal that the strength of fluctuations in the buffer layer is higher than that in the log layer. The results also showed that polymers in elongation deformation of S_{11} and S_{22} are subjected to almost similar magnitude of compression, since PDF profiles have a symmetric distribution with respect to zero. However, regarding shear strain rate, the polymers are subject to stretching more than compression. As a polymer concentration increases, the polymer chains are more subject to stretching than compression due to shear rate in buffer layer and log layer.

The PSD profiles of streamwise, wall-normal and shear strain rate fluctuations from the Lagrangian method for polymer solution decrease with increasing polymer concentration compared with water flow throughout the entire frequency range. At y_0^+=16 , there is a large reduction of PSD at high frequency at maximum drag reduction, while there is an increase at high frequency for polymeric flows (10, 20 and 90 ppm). At y_0^+=27, the PSD of streamwise strain rate fluctuations increased at high frequency while they have almost the same magnitude at low and high frequency at y_0^+ =145. In case of wall-normal strain rate fluctuations, the PSD profiles have similar trend in the buffer and log layer. The PSD of shear strain fluctuations shows that the difference between water and polymeric flows increases at high frequency and magnitude of reduction is higher in the buffer layer compared with log layer.

Chapter 6. Evaluation of 3D measurements

6.1 Introduction

The previous experimental studies of turbulence flows with drag reducing polymers have been mainly limited to two velocity components (e.g., Warholic *et al*. 1999; Escudier *et al.* 2009). As a result, the full 3D features of the turbulent flow require further scrutiny. The unique feature of the data presented in this chapter is the measurement of all the three components of velocity at low and high drag reduction (DR). The present work experimentally investigates the effect of polymers on all the Reynolds stress components in the near wall region of a turbulent channel flow. The measurements also aim at evaluation of a new three-dimensional particle tracking technique known as "Shake-the-box" (STB) (Schanz *et al*. 2016). The optimization of the STB parameters are discussed and presented in Appendix B.

6.2 Results and discussion

6.2.1 Mean velocity profile

The profiles of mean streamwise velocity $<U>$ normalized by the bulk velocity U_b are presented in Figure 6.1 based on 3D-PTV measurements. The results agree with results from 2D-PIV, previously presented in Chapter 5. The velocity gradient ($d<U>/dy$) at the wall decreases with increasing polymer concentration. It is should be noted that the profiles of shear thinning flows are far away from the laminar flow. The mean streamwise velocity in laminar channel flow is given by the following equation (Weigand, 2004):

$$\frac{U}{<U>} = \frac{3}{2}\left(1 - \left(\frac{y}{\delta}\right)^2\right). \tag{6.1}$$

Comparison of the semi-logarithmic plot of mean streamwise velocity profiles $<U>$ of water normalized with the same friction velocity of water $u_{\tau 0}$= 0.0589 m/s from STB and PIV is shown in Figure 6.2. The results from STB show more accurate results in the viscous sublayer than 2D-PIV. The profiles of mean velocity from STB shows a good agreement with the law of the wall ($u^+ = y^+$) and the von-karman log-law ($u^+ = 1/\kappa \, ln \, y + B$) with $\kappa = 0.389$ and $B = 5.5$

which confirms a fully developed flow. The average uncertainty for STB under the ideal imagining conditions is 0.0033 pix for seeding densities of 0.05 ppp (Schanz *et al.,* 2014). In the case of considering vibrations of the single camera lines-of-sight and distribution of particle size within the flow, a position uncertainty is assumed to be ~ 0.1 pix for STB (Schröder *et al.,* 2015). The error in measurement of $<U>$ for water flow is 0.03 m/s (0.503 $u_{\tau 0}$) assuming ~ 0.1 pix position uncertainty.

The effect of polymer concentration on the turbulent layer in a semi-logarithmic plot is shown in Figure 6.3. The results are in agreement with observation from 2D-PIV measurements. The viscous sublayer and buffer layer become thicker with increasing polymer concentration. The log-layer of the profiles of low polymer concentration is shifted upward and remains parallel to water flow. The slope of log-layer continues to increase as polymer concentration increases until the profile reaches the MDR asymptote Virk *et al*. (1970).

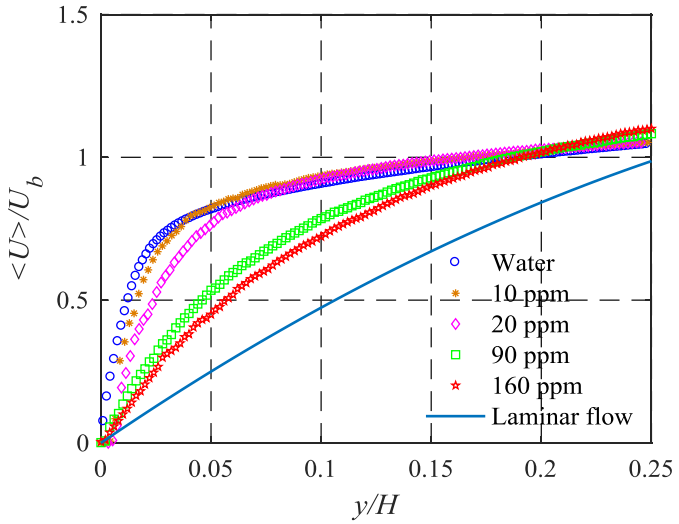

Figure 6.1. Mean velocity profile of water and four different polymer concentrations obtained from STB.

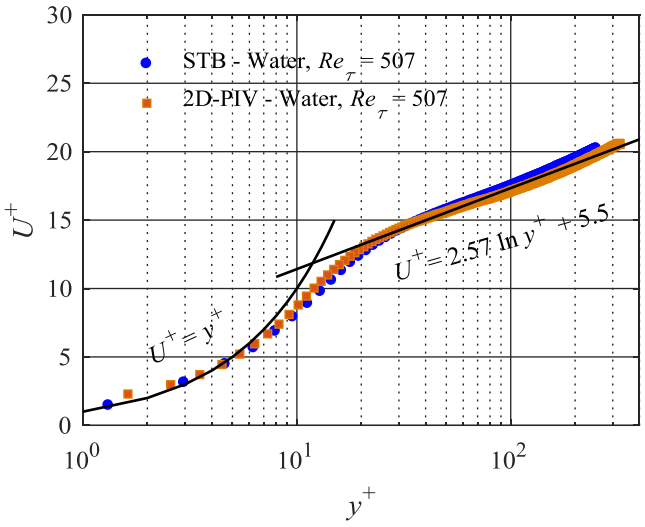

Figure 6.2. Semi-logarithmic plot of mean velocity of water from 2D-PIV and STB. The data is normalized using the same friction velocity of water.

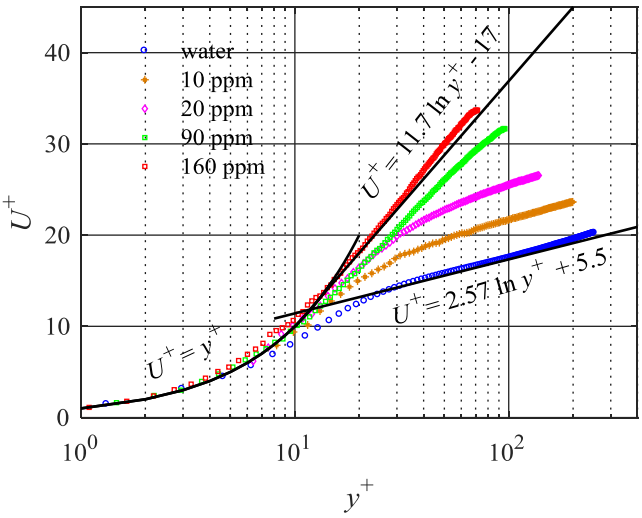

Figure 6.3. Semi-logarithmic plot of mean velocity from STB. The data of each polymer solution is normalized using the corresponding inner scaling. The law of the wall ($U^+=y^+$), log-law of Newtonian flows ($U^+=2.57\ln y^+ +5.5$), and Virk's asymptote ($U^+=11.7\ \ln y^+ -17$).

6.2.2 Reynolds stresses

All the profiles of Reynolds stresses, shown in Figure 6.4, are normalized by the inner scaling of water ($u_{\tau 0}$). The profiles of wall-normal Reynolds stress $<u^2>/u^2_{\tau 0}$ are presented in Figure 6.4 (a). In the vicinity of the wall, the profile of $<u^2>/u^2_{\tau 0}$ for water flow is higher than that of DNS of Moser *et al*. (2015) at Re_τ = 544. Away from the peak, discrepancy with respect to the DNS is small. The profiles of wall-normal, shear and spanwise Reynolds stresses for water flow agree with DNS. The results of Reynolds stresses ($<u^2>$, $<v^2>$ and $<uv>$) for polymeric flow show a similar trend as observed from 2D-PIV measurements. The Reynolds stresses decrease with increasing DR. The location of the peak moves continuously away from the wall with increasing polymer concentration. The error in measurement of $<uv>$ for water flow is $\varepsilon_{uv} = 0.25\ u^2_{\tau 0}$ with the assumption of ~ 0.1 pix position uncertainty (Schröder *et al.,* 2015).

Figure 6.4 (d) shows the normalized spanwise Reynolds stress $<w^2>/u^2_{\tau 0}$ from time resolved 3D-PTV measurements. The evaluation of spanwise Reynolds stress is of interest since it is not available from planar PIV over *xy* plane. The $<w^2>/u^2_{\tau 0}$ profile and the peak value of each profile attenuate with increasing polymer concentration or in other words with increasing DR. The strongest reduction is observed at maximum drag reduction.

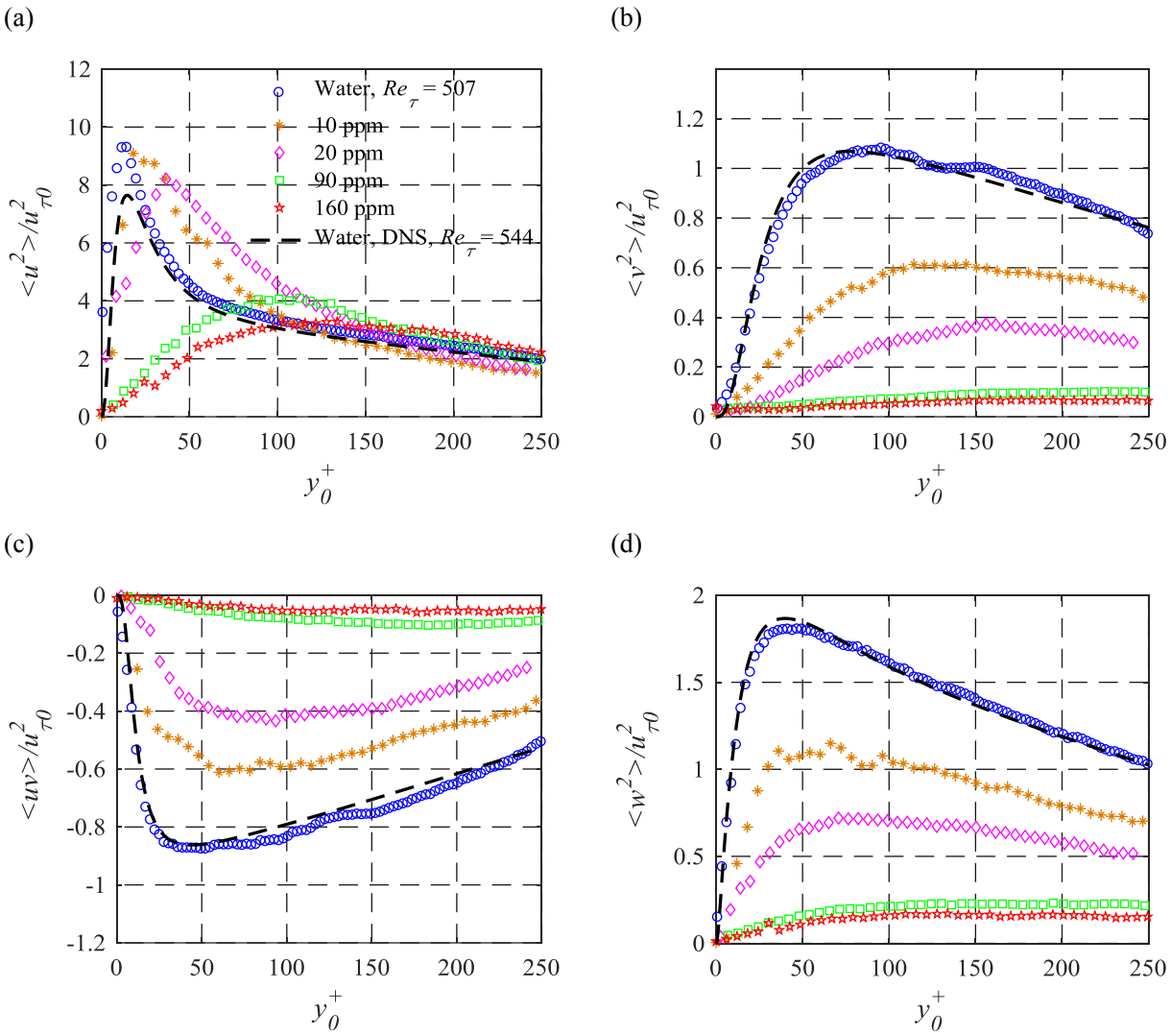

Figure 6.4. The effect of polymer concentration on the (a) streamwise and (b) wall-normal and (c) shear, and (d) spanwise Reynolds stresses normalized by the friction velocity of water ($u_{\tau 0}$).

6.2.3 Production of turbulent kinetic energy

The effect of polymer concentration on the production of turbulence kinetic energy (P_k) is presented in Figure 6.5. The normalized production of turbulence kinetic energy (P_k) is defined as

$$P_k = -\langle uv \rangle \frac{d\langle U \rangle}{dy} \frac{\delta_v}{u_\tau^3} \tag{6.2}$$

The profile of production of turbulence kinetic energy shows a good agreement with DNS of Moser *et al*. (2015) at Re_τ = 544. It is observed that production of turbulence kinetic energy for polymeric flow is smaller than that of the corresponding Newtonian flow and the difference is larger with higher concentration. For low polymer concentration, it is clearly noticeable that peak of the production of turbulence kinetic energy is shifted away from the wall, which is consistent with an increase in the thickness of the viscous and buffer layer. In case of shear thinning polymeric flows, the peak of production of turbulence kinetic energy has almost vanished.

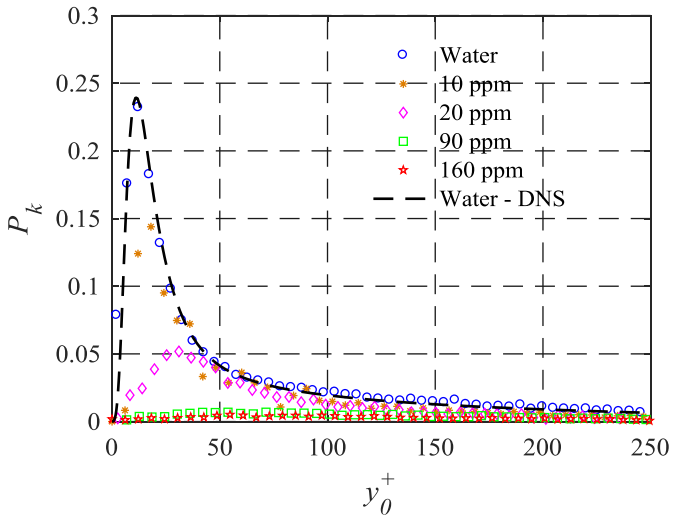

Figure 6.5. Production of turbulence kinetic energy (P_k) normalized by the inner scaling of water as a function of the distance from the wall for water and polymeric flows.

6.3 Conclusion

Time-resolved 3D-PTV "Shake-the-box" (STB) technique is evaluated near the wall for water and different polymeric flows. The investigation of the STB performance shows accurate measurement of the mean velocity profile and the wall-normal, spanwise and shear Reynolds stresses. Results compare well with those from DNS. However, there is a discrepancy between streamwise Reynolds stress and DNS near the wall ($y_0^+ < 20$).

The results of mean velocity profile and Reynolds stresses (streamwise, wall-normal and shear) for polymeric flow from 3D-PTV show trends similar to that observed in 2D-PIV. The profile of spanwise Reynolds stress for polymer flow decreases as drag reduction increases and the largest reduction of spanwise Reynolds stress is observed at maximum drag reduction. The normalized profiles of production of turbulence kinetic energy show a shift in the peak location in dilute polymer solutions and the peak is vanished in concentrated polymer solution. All the profiles of production of turbulence kinetic energy for polymeric flows are reduced and they are close to zero in the more concentrated polymer solution.

Chapter 7. Conclusion

The results from pressure measurements show that an increase in polymer concentration leads to a decrease in degradation rate and an increases in drag reduction. It is also observed that polymers are subjected to less shear degradation in a Moyno pump compared with a centrifugal pump.

Rheological measurements show that the extensional viscosity and the relaxation time increases with increasing polymer concentration. The dilute polymer solutions of polymers have lower potential to stretch compared with concentrated polymer solutions, which is consistent with results of drag reduction.

Time-resolved 2D-PIV and 3D-PTV, based on the "Shake-the-box" method, are carried out in a turbulent channel flow. The results show a significant modification of the near-wall turbulent structure of the polymeric solutions relative to its Newtonian counterpart. The viscous sublayer and buffer layer thicken. The log-region is shifted upwards while it remains essentially parallel to water in dilute polymer solutions at low drag reduction. In the case of concentrated polymer solutions, the profiles in the log-layer are not only shifted upward but also have a higher slope than that of water. The slope continues to increase as DR increases until the profile reaches the MDR asymptote.

The peak values of streamwise Reynolds stress in polymer flow are smaller than that of the corresponding Newtonian flow (water). Those peaks move away from the wall with increasing polymer concentration. A large decrease in spanwise root-mean-square of vorticity fluctuation, and wall-normal and spanwise Reynolds stresses at maximum drag reduction is observed. Reynolds shear stress is also close to zero at maximum drag reduction. The contribution of sweep and ejection motions to the negative Reynolds stress turbulence (i.e., to positive turbulence production) is reduced in polymeric flows. This is consistent with a significant reduction in production of turbulence kinetic energy. It is also noted that an increase in polymer concentration results in decrease of momentum transfer. The power spectral density (PSD) of streamwise and wall normal velocity fluctuation at buffer and log-layer shows a reduction over

all frequencies while energy decreases with increasing drag reduction. The reduction in energy becomes smaller in the log layer compared with buffer layer and the largest reduction is observed at high frequency. This implies that there reduction in the small eddies is higher than in large eddies since large eddies corresponds to the low frequency domain.

The effect of polymers on the field of strain rate in channel flow along with extensional viscosity measurements is investigated since no experimental work is available. The rate of strain is used to identify the strength of the flow field. The polymer chains in channel flow are subject to stretch, compression and rotation. The results show that the extent of deformation in channel flow depends strongly on the wall-normal location. The strength of the flow field including strain rate for elongational flow and shear rate for shear flow was investigated at buffer layer at y_0^+=16, and also compared with y_0^+= 27 and 145. The results show that significant fluctuations in strain tensors occur in the buffer layer at y_0^+=16 implying a large increase in extensional viscosity in the buffer layer. It was also obsrved that the main contribution to the deformation comes from the fluctuations of streamwise strain rate at the buffer layer. However, in the log layer (y_0^+=145), the contribution of streamwise and wall-normal strain rate fluctuations is almost the same, which means that polymer chains will be more subjected to biaxial-elongation since the effect of shear rate is small at the log layer. The PDF profiles of wall-normal strain rate fluctuations show similar profiles at three different wall-normal locations. The PDF profiles of streamwise and wall-normal strain rate have symmetrical distribution with respect to zero strain rate. This implies that both stretching and more compression take place. In shear rate, on the contrary, it is expected that polymer chains will be significantly subjected to stretch more than compression since the PDF profile of polymeric flows are shifted to positive side especially at the buffer layer.

The PSD of the streamwise strain rate fluctuations in the Lagrangian method shows a decrease in energy with increase of polymer concentration. At y_0^+=16, The PSD profiles of concentrated polymer solutions show a decrease in energy at high frequencies while an increase was observed in dilute polymer solutions. The difference between the PSD of the polymeric flows and water decreases as distance from the wall increases. The PSD profiles of the wall-normal strain rate fluctuations in the Lagrangian frame of reference are similar at three different wall-normal locations. The reduction in energy increases as drag reduction increases and PSD

profiles of all polymeric flows are parallel to water flow. This is consistent with observations in PDF profiles of wall-normal strain rate. In shear rate, the PSD profiles of polymeric flows show a decrease in energy at high frequency with respect to water. The magnitude of reduction in PSD is more pronounced in the buffer layer. There was a strong increase of the local extensional viscosity in the buffer layer due to strong fluctuations of strain tensors, which is consistent with the large reduction in production of turbulence kinetic energy in the buffer layer as well as an increase in the thickness of buffer layer.

Recommendations for future research

The results obtained and presented here for the deformation tensor are based on the deformation tensor for small deformations since measurement is limited to two-dimensions. It is recommended to extend this work using time-resolved Tomo-PIV measurement to obtain both the second and the third invariants of the rate-of strain tensor. In addition, pressure and Tomo-PIV measurements should be carried out at the same measurement location in order to obtain all the terms in the budgets of Reynolds stress and kinetic energy. This can help to answer many of the questions regarding the second theory "elastic theory" for drag reduction. Using Tomo-PIV measurement, the three components of the vorticity can also be simultaneously calculated which have not been experimentally reported before.

References

Deutsch, S., Moeny, M., Fontaine, A. A., & Petrie, H. (2004). Microbubble drag reduction in rough walled turbulent boundary layers with comparison against polymer drag reduction. *Experiments in fluids*, *37*(5), 731-744.

Rothstein, J. P. (2010). Slip on superhydrophobic surfaces. *Annual Review of Fluid Mechanics*, *42*, 89-109.

Walsh, M. J., & Lindemann, A. M. (1984). *Optimization and application of riblets for turbulent drag reduction*. Reston, VA: American Institute of Aeronautics and Astronautics.

Warholic, M. D., Massah, H., & Hanratty, T. J. (1999). Influence of drag-reducing polymers on turbulence: effects of Reynolds number, concentration and mixing. *Experiments in fluids*, *27*(5), 461-472.

Kawaguchi, Y., Segawa, T., Feng, Z., & Li, P. (2002). Experimental study on drag-reducing channel flow with surfactant additives—spatial structure of turbulence investigated by PIV system. *International Journal of Heat and Fluid Flow*, *23*(5), 700-709.

McComb, W. D., & Chan, K. T. J. (1985). Laser-Doppler anemometer measurements of turbulent structure in drag-reducing fibre suspensions. *Journal of Fluid Mechanics*, *152*, 455-478.

Toms, B. A. (1948). Some observations on the flow of linear polymersolutions through straight tubes at large Reynolds numbers. In *Proc. 1st Intl Congr. Rheol.* (Vol. 2, pp. 135-141).

Donohue, G. L., Tiederman, W. G., & Reischman, M. M. (1972). Flow visualization of the near-wall region in a drag-reducing channel flow. *Journal of Fluid Mechanics*, *56*(3), 559-575.

Virk, P. S. (1975). Drag reduction fundamentals. *AIChE Journal*, *21*(4), 625-656.

Reischman, M. M., & Tiederman, W. G. (1975). Laser-Doppler anemometer measurements in drag-reducing channel flows. *Journal of Fluid Mechanics*, *70*(2), 369-392.

Wei, T., & Willmarth, W. W. (1992). Modifying turbulent structure with drag-reducing polymer additives in turbulent channel flows. *Journal of Fluid Mechanics*, *245*, 619-641.

Ptasinski, P. K., Nieuwstadt, F. T. M., Van Den Brule, B. H. A. A., & Hulsen, M. A. (2001). Experiments in turbulent pipe flow with polymer additives at maximum drag reduction. *Flow, Turbulence and Combustion*, *66*(2), 159-182.

Escudier, M. P., Nickson, A. K., & Poole, R. J. (2009). Turbulent flow of viscoelastic shear-thinning liquids through a rectangular duct: Quantification of turbulence anisotropy. *Journal of Non-Newtonian Fluid Mechanics*, *160*(1), 2-10.

Warholic, M. D., Heist, D. K., Katcher, M., & Hanratty, T. J. (2001). A study with particle-image velocimetry of the influence of drag-reducing polymers on the structure of turbulence. *Experiments in fluids*, *31*(5), 474-483.

White, C. M., Somandepalli, V. S. R., & Mungal, M. G. (2004). The turbulence structure of drag-reduced boundary layer flow. *Experiments in Fluids*, *36*(1), 62-69.

Hou, Y. X., Somandepalli, V. S. R., & Mungal, M. G. (2008). Streamwise development of turbulent boundary-layer drag reduction with polymer injection. *Journal of Fluid Mechanics*, *597*, 31-66.

Virk, P. S., Merrill, E. W., Mickley, H. S., Smith, K. A., & Mollo-Christensen, E. L. (1967). The Toms phenomenon: turbulent pipe flow of dilute polymer solutions. *Journal of Fluid Mechanics*, *30*(2), 305-328.

Virk, P. S. (1971). An elastic sublayer model for drag reduction by dilute solutions of linear macromolecules. *Journal of Fluid Mechanics*, *45*(3), 417-440.

Virk, P. S. (1971). Drag reduction in rough pipes. *Journal of fluid mechanics*, *45*(2), 225-246.

Oldaker, D. K., & Tiederman, W. G. (1977). Spatial structure of the viscous sublayer in drag-reducing channel flows. *The Physics of Fluids*, *20*(10), S133-S144.

Sureshkumar, R., Beris, A. N., & Handler, R. A. (1997). Direct numerical simulation of the turbulent channel flow of a polymer solution. *Physics of Fluids*, *9*(3), 743-755.

Min, T., Choi, H., & Yoo, J. Y. (2003). Maximum drag reduction in a turbulent channel flow by polymer additives. *Journal of Fluid Mechanics*, *492*, 91-100.

Min, T., Yoo, J. Y., & Choi, H. (2001). Effect of spatial discretization schemes on numerical solutions of viscoelastic fluid flows. *Journal of non-newtonian fluid mechanics*, *100*(1), 27-47.

Kim, K., Li, C. F., Sureshkumar, R., Balachandar, S., & Adrian, R. J. (2007). Effects of polymer stresses on eddy structures in drag-reduced turbulent channel flow. *Journal of Fluid Mechanics*, *584*, 281-299.

Stone, P. A., Roy, A., Larson, R. G., Waleffe, F., & Graham, M. D. (2004). Polymer drag reduction in exact coherent structures of plane shear flow. *Physics of Fluids*, *16*(9), 3470-3482.

Dubief, Y., White, C. M., Terrapon, V. E., Shaqfeh, E. S., Moin, P., & Lele, S. K. (2004). On the coherent drag-reducing and turbulence-enhancing behaviour of polymers in wall flows. *Journal of Fluid Mechanics*, *514*, 271-280.

Ptasinski, P. K., Boersma, B. J., Nieuwstadt, F. T. M., Hulsen, M. A., Van den Brule, B. H. A. A., & Hunt, J. C. R. (2003). Turbulent channel flow near maximum drag reduction: simulations, experiments and mechanisms. *Journal of Fluid Mechanics*, *490*, 251-291.

Terrapon, V. E., Dubief, Y., Moin, P., & Shaqfeh, E. S. (2003, January). Brownian dynamics simulation in a turbulent channel flow. In *Proc. 4th ASME-JSME Joint Fluids Eng. Conf., Honolulu*.

Gyr, A., & Bewersdorff, H. W. (2013). *Drag reduction of turbulent flows by additives* (Vol. 32). Springer Science & Business Media.

Doering, C. R., Eckhardt, B., & Schumacher, J. (2006). Failure of energy stability in Oldroyd-B fluids at arbitrarily low Reynolds numbers. *Journal of non-newtonian fluid mechanics*, *135*(2), 92-96.

Baron, A., & Sibilla, S. (1997). DNS of the turbulent channel flow of a dilute polymer solution. *Applied scientific research*, *59*(4), 331-352.

Sibilla, S., & Baron, A. (2002). Polymer stress statistics in the near-wall turbulent flow of a drag-reducing solution. *Physics of Fluids*, *14*(3), 1123-1136.

Cant, S. (2001). SB Pope, Turbulent Flows, Cambridge University Press, Cambridge, UK, 2000, 771 pp.

Pinho, F. T., & Whitelaw, J. H. (1990). Flow of non-Newtonian fluids in a pipe. *Journal of Non-Newtonian Fluid Mechanics*, *34*(2), 129-144.

Draad, A. A., Kuiken, G. D. C., & Nieuwstadt, F. T. M. (1998). Laminar–turbulent transition in pipe flow for Newtonian and non-Newtonian fluids. *Journal of Fluid Mechanics*, *377*, 267-312.

Gyr, A., & Tsinober, A. (1997). On the rheological nature of drag reduction phenomena. *Journal of Non-Newtonian Fluid Mechanics*, *73*(1), 153-162.

Den Toonder, J. M. J., Hulsen, M. A., Kuiken, G. D. C., & Nieuwstadt, F. T. M. (1997). Drag reduction by polymer additives in a turbulent pipe flow: numerical and laboratory experiments. *Journal of Fluid Mechanics*, *337*, 193-231.

Truong, V. T. (2001). *Drag reduction technologies* (No. DSTO-GD-0290). DEFENCE SCIENCE AND TECHNOLOGY ORGANISATION VICTORIA (AUSTRALIA) AERONAUTICAL AND MARITIME RESEARCH LAB.

Qi, Y., & Zakin, J. L. (2002). Chemical and rheological characterization of drag-reducing cationic surfactant systems. *Industrial & engineering chemistry research*, *41*(25), 6326-6336.

Tamano, S., Kitao, T., & Morinishi, Y. (2014). Turbulent drag reduction of boundary layer flow with non-ionic surfactant injection. *Journal of Fluid Mechanics*, *749*, 367-403.

Forrest, F., & Grierson, G. A. (1931). Friction losses in cast iron pipe carrying paper stock. *Paper Trade Journal*, *92*(22), 39-41.

Mewis, J., & Metzner, A. B. (1974). The rheological properties of suspensions of fibres in Newtonian fluids subjected to extensional deformations. *Journal of Fluid Mechanics*, *62*(3), 593-600.

Kale, D. D., & Metzner, A. B. (1976). Turbulent drag reduction in dilute fiber suspensions: Mechanistic considerations. *AIChE Journal*, *22*(4), 669-674.

Lee, P. F., & Duffy, G. G. (1976). Relationships between velocity profiles and drag reduction in turbulent fiber suspension flow. *AIChE Journal*, *22*(4), 750-753.

Radin, I., Zakin, J. L., & Patterson, G. K. (1975). Drag reduction in solid-fluid systems. *AIChE Journal*, *21*(2), 358-371.

Roy, A., & Larson, R. G. (2005). A mean flow model for polymer and fiber turbulent drag reduction. *Applied Rheology*, *15*(6), 370-389.

Wang, Y., Yu, B., Zakin, J. L., & Shi, H. (2011). Review on drag reduction and its heat transfer by additives. *Advances in Mechanical Engineering*, *3*, 478749.

Ellis, H. D. (1970). Effects of shear treatment on drag-reducing polymer solutions and fibre suspensions. *Nature*, *226*(5243), 352-353.

Lee, W. K., Vaseleski, R. C., & Metzner, A. B. (1974). Turbulent drag reduction in polymeric solutions containing suspended fibers. *AIChE Journal*, *20*(1), 128-133.

Kale, D. D., & Metzner, A. B. (1974). Turbulent drag reduction in fiber-polymer systems: Specificity considerations. *AIChE Journal*, *20*(6), 1218-1219.

Bahadur, P., & Sastry, N. V. (2005). *Principles of polymer science*. Alpha Science Int'l Ltd..

Soldati, A., & Monti, R. (Eds.). (2014). *Turbulence Structure and Modulation* (Vol. 415). Springer.

Japper-Jaafar, A., Escudier, M. P., & Poole, R. J. (2009). Turbulent pipe flow of a drag-reducing rigid "rod-like" polymer solution. *Journal of Non-Newtonian Fluid Mechanics*, *161*(1), 86-93.

Gillissen, J. J. J. (2008). Polymer flexibility and turbulent drag reduction. *Physical Review E*, *78*(4), 046311.

Pereira, A. S., Andrade, R. M., & Soares, E. J. (2013). Drag reduction induced by flexible and rigid molecules in a turbulent flow into a rotating cylindrical double gap device: Comparison between Poly (ethylene oxide), Polyacrylamide, and Xanthan Gum. *Journal of Non-Newtonian Fluid Mechanics*, *202*, 72-87.

Andrade, R. M., Pereira, A. S., & Soares, E. J. (2016). Drag reduction in synthetic seawater by flexible and rigid polymer addition into a rotating cylindrical double gap device. *Journal of Fluids Engineering*, *138*(2), 021101.

Den Toonder, J. M. J., Draad, A. A., Kuiken, G. D. C., & Nieuwstadt, F. T. M. (1995). Degradation effects of dilute polymer solutions on turbulent drag reduction in pipe flows. *Applied Scientific Research*, *55*(1), 63-82.

Shupe, R. D. (1981). Chemical stability of polyacrylamide polymers. *Journal of Petroleum Technology*, *33*(08), 1-513.

McComb, W. D., & Rabie, L. H. (1982). Local drag reduction due to injection of polymer solutions into turbulent flow in a pipe. Part I: Dependence on local polymer concentration. *AIChE Journal*, *28*(4), 547-557.

Martin, F. D. (1986). Mechanical degradation of polyacrylamide solutions in core plugs from several carbonate reservoirs. *SPE Formation Evaluation*, *1*(02), 139-150.

Bueche, F. (1960). Mechanical degradation of high polymers. *Journal of Applied Polymer Science*, *4*(10), 101-106.

Lumley, J. L. (1973). Drag Reduction in Turbulent Flow by Polymer Additives. *J. Polym. Sci. Macromol*. **(7)**, 263–290.

Tabor, M., & De Gennes, P. G. (1986). A cascade theory of drag reduction. *EPL (Europhysics Letters)*, *2*(7), 519.

Lumley, J. L. (1969). Drag reduction by additives. *Annual review of fluid mechanics*, *1*(1), 367-384.

Metzner, A. B., & Metzner, A. P. (1970). Stress levels in rapid extensional flows of polymeric fluids. *Rheologica Acta*, *9*(2), 174-181.

Hinch, E. J. (1977). Mechanical models of dilute polymer solutions in strong flows. *The Physics of Fluids*, *20*(10), S22-S30.

Ryskin, G. (1987). Turbulent drag reduction by polymers: a quantitative theory. *Physical review letters*, *59*(18), 2059.

Landahl, M. T. (1973). Drag reduction by polymer addition. In *Theoretical and Applied Mechanics* (pp. 177-199). Springer, Berlin, Heidelberg.

Landahl, M. T. (1977). Dynamics of boundary layer turbulence and the mechanism of drag reduction. *The Physics of Fluids*, *20*(10), S55-S63.

Orlandi, P. (1995). A tentative approach to the direct simulation of drag reduction by polymers. *Journal of non-newtonian fluid mechanics*, *60*(2-3), 277-301.

De Gennes, P. G. (1990). *Introduction to polymer dynamics*. CUP Archive.

Sreenivasan, K. R., & White, C. M. (2000). The onset of drag reduction by dilute polymer additives, and the maximum drag reduction asymptote. *Journal of Fluid Mechanics*, *409*, 149-164.

Rabin, Y., & Zielinska, B. J. (1989). Scale-dependent enhancement and damping of vorticity disturbances by polymers in elongational flow. *Physical review letters*, *63*(5), 512.

Walker, D. T., & Tiederman, W. G. (1990). Turbulent structure in a channel flow with polymer injection at the wall. *Journal of Fluid Mechanics*, *218*, 377-403.

Rudd, M. J. (1972). Velocity measurements made with a laser dopplermeter on the turbulent pipe flow of a dilute polymer solution. *Journal of Fluid Mechanics*, *51*(4), 673-685.

Chung, J. S., & Graebel, W. P. (1972). Laser Anemometer Measurements of Turbulence in Non-Newtonian Pipe Flows. *The physics of fluids*, *15*(4), 546-554.

Logan, S. E. (1972). *LASER VELOCIMETER MEASUREMENT OF REYNOLDS STRESS AND TURBULENCE IN DILUTE POLYMER SOLUTION* (No. GALCIT-Pub-700).

Mizushina, T., & Usui, H. (1977). Reduction of eddy diffusion for momentum and heat in viscoelastic fluid flow in a circular tube. *The physics of fluids*, *20*(10), S100-S108.

Pereira, A. S., & Pinho, F. T. (1994). Turbulent pipe flow characteristics of low molecular weight polymer solutions. *Journal of non-newtonian fluid mechanics*, *55*(3), 321-344.

Willmarth, W. W., Wei, T., & Lee, C. O. (1987). Laser anemometer measurements of Reynolds stress in a turbulent channel flow with drag reducing polymer additives. *The Physics of fluids*, *30*(4), 933-935.

Luchik, T. S., & Tiederman, W. G. (1988). Turbulent structure in low-concentration drag-reducing channel flows. *Journal of Fluid Mechanics*, *190*, 241-263.

Harder, K. J., & Tiederman, W. G. (1991). Drag reduction and turbulent structure in two-dimensional channel flows. *Philosophical Transactions of the Royal Society of London A: Mathematical, Physical and Engineering Sciences*, *336*(1640), 19-34.

Wei, T., & Willmarth, W. W. (1992). Modifying turbulent structure with drag-reducing polymer additives in turbulent channel flows. *Journal of Fluid Mechanics*, *245*, 619-641.

Escudier, P., & Smith, S. (2001, April). Fully developed turbulent flow of non–Newtonian liquids through a square duct. In *Proceedings of the Royal Society of London A: Mathematical, Physical and Engineering Sciences* (Vol. 457, No. 2008, pp. 911-936). The Royal Society.

Somandepalli, V. S. R., White, C. M., & Mungal, M. G. (2003, July). Boundary layer studies on polymer drag reduction using PIV and PLIF. In *Proceedings 4th ASME/JSME Joint Fluids Engineering Conference*.

Gyr, A. (1976). Burst cycle and drag reduction. *Zeitschrift für angewandte Mathematik und Physik ZAMP*, *27*(6), 717-725.

Achia, B. U., & Thompson, D. W. (1977). Structure of the turbulent boundary in drag-reducing pipe flow. *Journal of Fluid Mechanics*, *81*(3), 439-464.

Oldaker, D. K., & Tiederman, W. G. (1977). Spatial structure of the viscous sublayer in drag-reducing channel flows. *The Physics of Fluids*, *20*(10), S133-S144.

Tiederman, W. G., Luchik, T. S., & Bogard, D. G. (1985). Wall-layer structure and drag reduction. *Journal of Fluid Mechanics*, *156*, 419-437.

Walker, D. T., Tiederman, W. G., & Luchik, T. S. (1986). Optimization of the injection process for drag-reducing additives. *Experiments in fluids*, *4*(2), 114-120.

Mohammadtabar, M., Sanders, R. S., & Ghaemi, S. (2017). Turbulent structures of non-Newtonian solutions containing rigid polymers. *Physics of Fluids*, *29*(10), 103101.

Bogard, D. G., & Tiederman, W. G. (1983). Investigation of flow visualization techniques for detecting turbulent bursts. In *Symposium on Turbulence, 7 th, Rolla, MO* (p. 1983).

Bogard, D. G., & Tiederman, W. G. (1986). Burst detection with single-point velocity measurements. *Journal of Fluid Mechanics*, *162*, 389-413.

Caulfield, M. J., Qiao, G. G., & Solomon, D. H. (2002). Some aspects of the properties and degradation of polyacrylamides. *Chemical reviews*, *102*(9), 3067-3084.

Metzner, A. B., & Otto, R. E. (1957). Agitation of non-Newtonian fluids. *AIChE Journal*, *3*(1), 3-10.

Pérez, J. S., Porcel, E. R., López, J. C., Sevilla, J. F., & Chisti, Y. (2006). Shear rate in stirred tank and bubble column bioreactors. *Chemical Engineering Journal*, *124*(1), 1-5.

Tatterson, G. B. (1991). *Fluid mixing and gas dispersion in agitated tanks*. McGraw-Hill Companies.

Paul, E. L., Atiemo-Obeng, V. A., & Kresta, S. M. (Eds.). (2004). *Handbook of industrial mixing: science and practice*. John Wiley & Sons.

Pérez, J. S., Porcel, E. R., López, J. C., Sevilla, J. F., & Chisti, Y. (2006). Shear rate in stirred tank and bubble column bioreactors. *Chemical Engineering Journal*, *124*(1), 1-5.

Stoops, C. E., & Lovell, C. L. (1943). Power Consumption of Propeller-Type Agitators. *Industrial & Engineering Chemistry*, *35*(8), 845-850.

Taylor, G. I. (1923). Stability of a viscous liquid contained between two rotating cylinders. *Philosophical Transactions of the Royal Society of London. Series A, Containing Papers of a Mathematical or Physical Character*, *223*, 289-343.

Entov, V. M., & Hinch, E. J. (1997). Effect of a spectrum of relaxation times on the capillary thinning of a filament of elastic liquid. *Journal of Non-Newtonian Fluid Mechanics*, *72*(1), 31-53.

Miller, E., Clasen, C., & Rothstein, J. P. (2009). The effect of step-stretch parameters on capillary breakup extensional rheology (CaBER) measurements. *Rheologica acta*, *48*(6), 625-639.

Yarin, A. L. (1993). *Free liquid jets and films: hydrodynamics and rheology*. Longman Publishing Group.

Renardy, M. (1995). A numerical study of the asymptotic evolution and breakup of Newtonian and viscoelastic jets. *Journal of non-newtonian fluid mechanics*, *59*(2-3), 267-282.

Anna, S.L., McKinley, G.H. (2001). *J. Rheol***.** 45,115-138.

McKinley, G. H. (2005). Visco-elasto-capillary thinning and break-up of complex fluids.

Kim, N. J., Pipe, C. J., Ahn, K. H., Lee, S. J., & McKinley, G. H. (2010). Capillary breakup extensional rheometry of a wormlike micellar solution. *Korea-Australia Rheology Journal*, *22*(1), 31-41.

Schümmer, P., & Tebel, K. H. (1983). A new elongational rheometer for polymer solutions. *Journal of Non-Newtonian Fluid Mechanics*, *12*(3), 331-347.

Marshall, R. J., & Metzner, A. B. (1966, January). Flow of viscoelastic fluids through porous media. In *Symposium on Mechanics of Rheologically Complex Fluids*. Society of Petroleum Engineers.

Delshad, M., Kim, D. H., Magbagbeola, O. A., Huh, C., Pope, G. A., & Tarahhom, F. (2008, January). Mechanistic interpretation and utilization of viscoelastic behavior of polymer solutions for improved polymer-flood efficiency. In *SPE Symposium on Improved Oil Recovery*. Society of Petroleum Engineers.

McKinley, G. H., & Tripathi, A. (2000). How to extract the Newtonian viscosity from capillary breakup measurements in a filament rheometer. *Journal of Rheology*, *44*(3), 653-670.

Theunissen, R., Scarano, F., & Riethmuller, M. L. (2008). On improvement of PIV image interrogation near stationary interfaces. *Experiments in Fluids*, *45*(4), 557-572.

Meinhart, C. D., Wereley, S. T., & Santiago, J. G. (2000). A PIV algorithm for estimating time-averaged velocity fields. *Journal of Fluids engineering*, *122*(2), 285-289.

Westerweel, J. (1997). Fundamentals of digital particle image velocimetry. *Measurement science and technology*, *8*(12), 1379.

Schanz, D., Gesemann, S., & Schröder, A. (2016). Shake-The-Box: Lagrangian particle tracking at high particle image densities. *Experiments in fluids*, *57*(5), 70.

Savins, J. G. (1964). Drag reduction characteristics of solutions of macromolecules in turbulent pipe flow. *Society of Petroleum Engineers Journal*, *4*(03), 203-214.

Gampert, B., & Wagner, P. (1985). The influence of molecular weight and molecular weight distribution on drag reduction and mechanical degradation in turbulent flow of highly dilute polymer solutions. In *The Influence of Polymer Additives on Velocity and Temperature Fields* (pp. 71-85). Springer, Berlin, Heidelberg.

Berman, N. S. (1986). Velocity fluctuations in non-homogeneous drag reduction. *Chemical Engineering Communications*, *42*(1-3), 37-51.

Hoyer, K., & Gyr, A. (1996). Turbulent velocity field in heterogeneously drag reduced pipe flow. *Journal of non-newtonian fluid mechanics*, *65*(2), 221-240.

Gampert, B., Braemer, T., Eich, T., & Dietmann, T. (2005). Rheo-optical investigations and near-wall turbulence structure of polymer solutions in turbulent channel flow. *Journal of non-newtonian fluid mechanics*, *126*(2), 115-121.

De Gennes, P. G. (1974). Coil-stretch transition of dilute flexible polymers under ultrahigh velocity gradients. *The Journal of Chemical Physics*, *60*(12), 5030-5042.

Babcock, H. P., Smith, D. E., Hur, J. S., Shaqfeh, E. S., & Chu, S. (2000). Relating the microscopic and macroscopic response of a polymeric fluid in a shearing flow. *Physical review letters*, *85*(9), 2018.

Clauser, F. H. (1954). Turbulent boundary layers in adverse pressure gradients. *J. aeronaut. Sci*, *21*(2), 91-108.

Dua, A., & Cherayil, B. J. (2003). Polymer dynamics in linear mixed flow. *The Journal of chemical physics*, *119*(11), 5696-5700.

Dua, A. (2010). Statics and Dynamics of Dilute Polymer Solutions. In *Rheology of Complex Fluids* (pp. 151-169). Springer New York.

Smith, D. E., Babcock, H. P., & Chu, S. (1999). Single-polymer dynamics in steady shear flow. *Science*, *283*(5408), 1724-1727.

Den Toonder, J. M. J., Nieuwstadt, F. T. M., & Kuiken, G. D. C. (1995). The role of elongational viscosity in the mechanism of drag reduction by polymer additives. *Applied scientific research*, *54*(2), 95-123.

Pollard, A., Castillo, L., Danaila, L., & Glauser, M. (Eds.). (2016). *Whither Turbulence and Big Data in the 21st Century?*. Springer.

Weigand, B. (2004) *Analytical methods for heat transfer and fluid flow problems* (Vol. 263). Berlin: Springer.

Raffel, M., Willert, C. E., & Kompenhans, J. (2007). *Particle image velocimetry: a practical guide*. Springer Science & Business Media.

Fu, Z., Otsuki, T., Motozawa, M., Kurosawa, T., Yu, B., & Kawaguchi, Y. (2014). Experimental investigation of polymer diffusion in the drag-reduced turbulent channel flow of inhomogeneous solution. *International Journal of Heat and Mass Transfer*, *77*, 860-873.

Sugioka, H., Fu, Z., Tsukahara, T., & Kawaguchi, Y. (2015, July). PIV-PLIF Experiment on Modification of Turbulent Scalar Diffusion Near the Wall by Uniform Blowing. In *ASME/JSME/KSME 2015 Joint Fluids Engineering Conference* (pp. V01AT25A004-V01AT25A004). American Society of Mechanical Engineers.

Schanz, D., Schröder, A., & Gesemann, S. (2014, July). Shake the box—a 4D PTV algorithm: accurate and ghostless reconstruction of Lagrangian tracks in densely seeded flows. In *17th international symposium on applications of laser techniques to fluid mechanics, Lisbon*.

Schröder, A., Schanz, D., Michaelis, D., Cierpka, C., Scharnowski, S., & Kähler, C. J. (2015). Advances of PIV and 4D-PTV" Shake-The-Box" for Turbulent Flow Analysis–the Flow over Periodic Hills. *Flow, Turbulence and Combustion*, *95*(2-3), 193-209.

Schanz, D., Schröder, A., Gesemann, S., Michaelis, D., & Wieneke, B. (2013). 'Shake The Box': A highly efficient and accurate Tomographic Particle Tracking Velocimetry (TOMO-PTV) method using prediction of particle positions.

Appendix A. Technical specifications

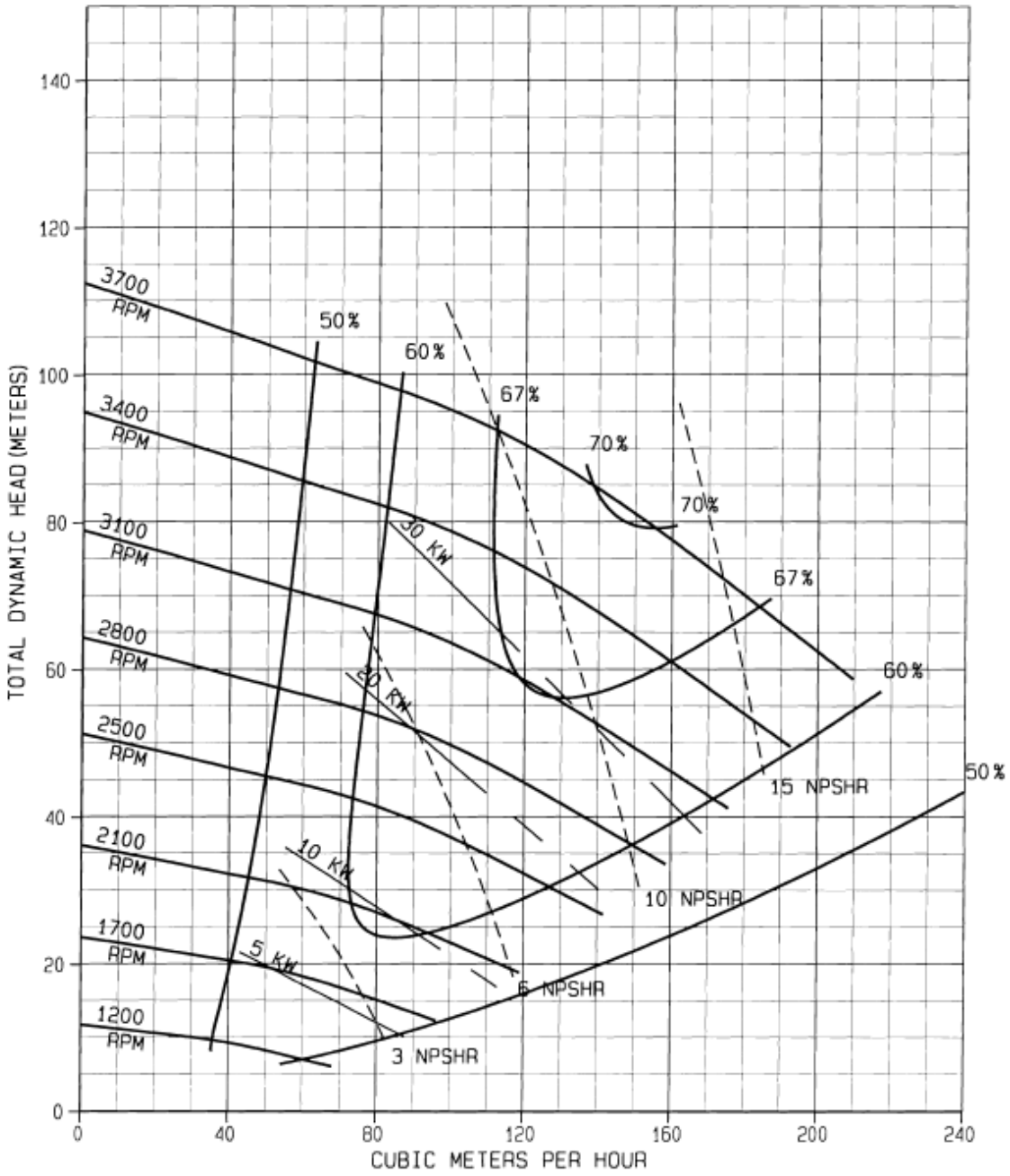

Figure A. 1. Centrifugal pump (LCC-M 50-230) curve. Source: GIW Industries Inc.

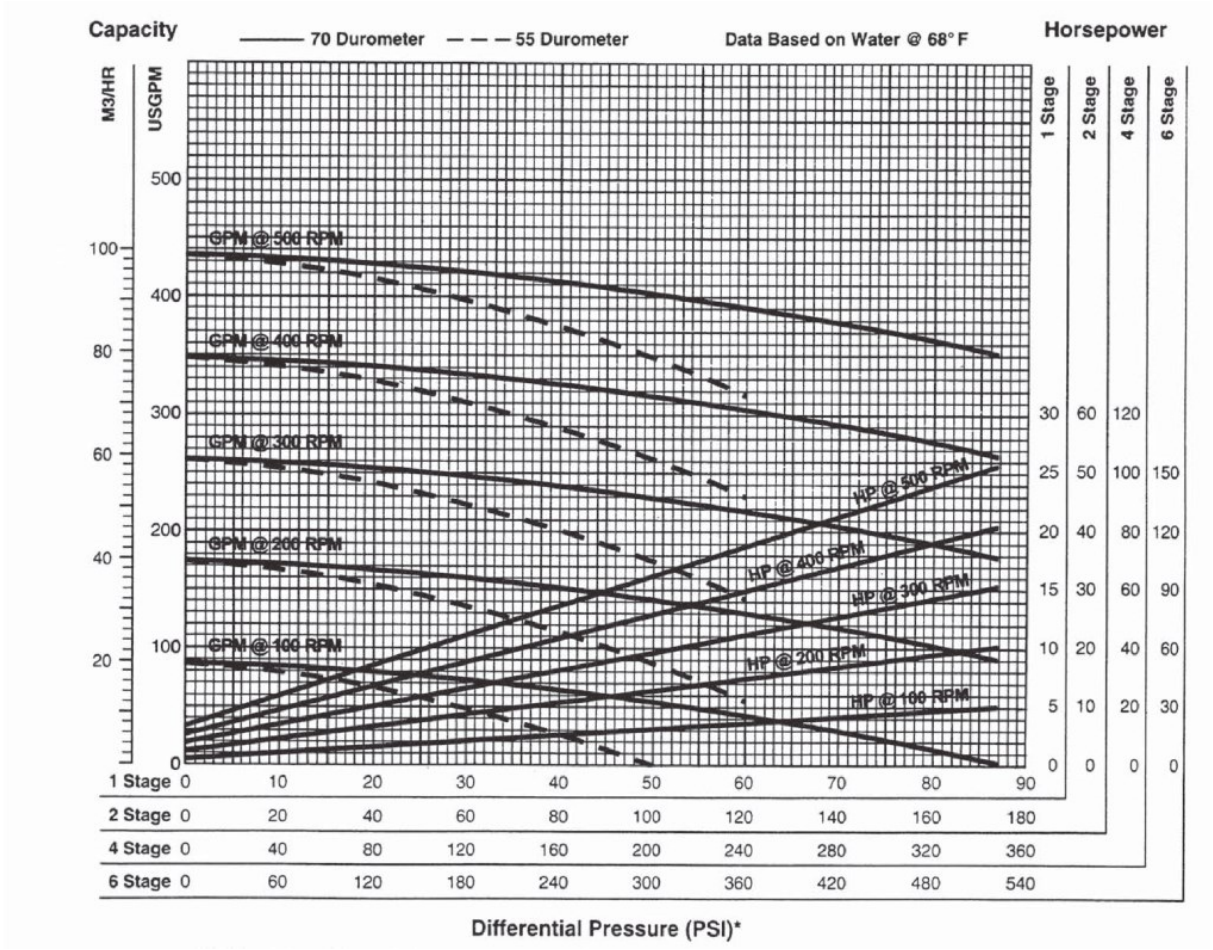

Figure A. 2. Progressive cavity pump (Moyno 2F090G1CDB3SAC). Source: Liberty Process Equipment.

Appendix B. Optimization of STB parameters

In order to perform STB analysis using Davis 8.4, several parameters should be properly set. The purpose of the work is to study the effect of several parameters in calculating particle tracks using STB. This chapter can be broadly divided into the following; default settings of Davis 8.4, adjusted settings and optimum settings. Default STB settings are based on the recommended settings provided by Davis 8.4 software. Adjusted settings are used to investigate the effect of changing parameters. The optimum parameters include the best values of the parameters, and a quadratic regression filter is also applied using Matlab. Each of these settings will be covered in more detail in the following sections. For all data presented in this chapter, the friction Reynolds number of water is calculated to be Re_τ = 507. DNS data at Re_τ = 544 is also provided for comparison (Lee & Moser 2015). The measurement volume is discretized into small bins (bins size = 0.06 mm). All particles of the data located within a bin are averaged.

B.1 Comparison of default with adjusted settings.

The objective of this section is to show the extent to which changing in advanced settings may reduce the noise. The comparison was carried out with Gaussian smoothing filter (3×3 pix) and without sharpening filter for both cases at threshold of 250. The default and adjusted advanced settings are available in Table B.1 and Table B.2, respectively. The comparison between default and adjusted advanced settings is shown in Figure B.1. Around 61 % and 32% reduction with using adjusted settings are observed in wall-normal Reynolds stress at viscous sublayer (y^+=4) and outer layer (y^+=52), respectively while there was a small decrease in streamwise and spanwise Reynolds stresses. These results motivate work to further investigate.

Table B.1. Default advanced setting of Davis 8.4.

Shaking	
Adding particles (outerloop)	4 iterations
Refine particle position and intensity (inner loop)	4 iterations
Shake particle position by	0.1 voxel
Remove particles if closer than	1 voxel
Remove weak particles if intensity <	0.1 of average particle intensity
Particle image shape and intensity	
Make OTF smaller	1.5 times
Residuum computation: increase particle intensity	1.5 times
Residuum computation: OTF radius	±2 pixel
Tracking: acceleration limits	
Maximum absolute change in particle shift	1 voxel
Maximum relative change in particle shift	20 %
Order for polynomial track fit	3
Length for polynomial track fit	11

Table B.2. Adjusted advanced setting.

Shaking	
Adding particles (outerloop)	5 iterations
Refine particle position and intensity (inner loop)	6 iterations
Shake particle position by	0.2 voxel
Remove particles if closer than	2 voxel
Remove weak particles if intensity <	0.8 of average particle intensity
Particle image shape and intensity	
Make OTF smaller	1.8 times
Residuum computation: increase particle intensity	1.8 times
Residuum computation: OTF radius	±5 pixel
Tracking: acceleration limits	
Maximum absolute change in particle shift	2 voxel
Maximum relative change in particle shift	50 %
Order for polynomial track fit	2
Length for polynomial track fit	11

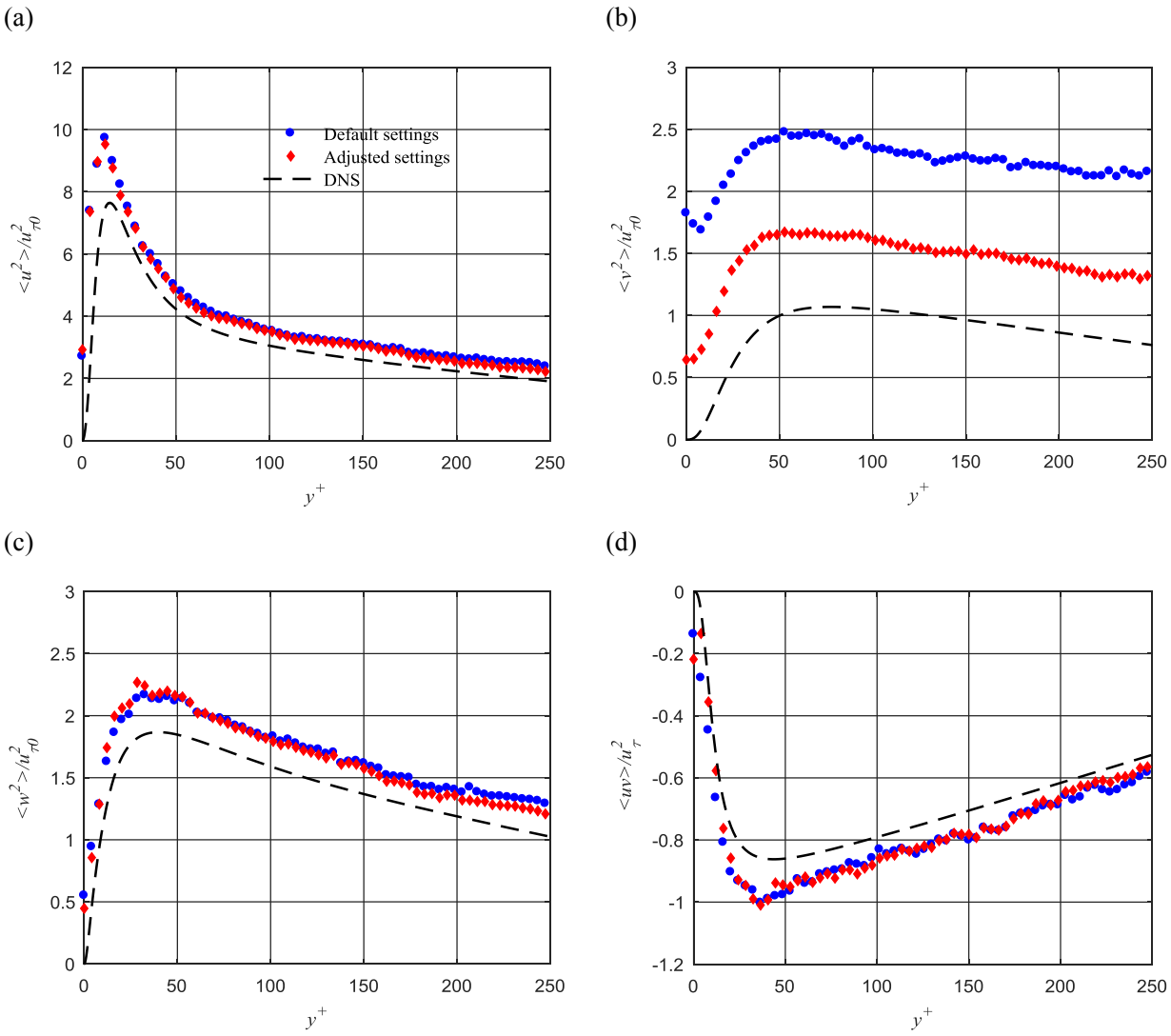

Figure B.1. Comparison between default and adjusted advanced settings at threshold of 250 (a) streamwise Reynolds stress, (b) wall-normal Reynolds stress, (c) spanwise Reynolds stress, (d) Reynolds shear stress.

B.2 Effect of intensity threshold

The intensity threshold for particle detection that is used for Shake-the-Box is an important parameter. In order to detect only true particles, the value of intensity threshold should be higher than noise level. Although a smaller threshold value detects a higher number of tracks, decreasing in the intensity of the threshold leads to an increase in noise peaks that might be considered as new particles and an increase in short tracks due to lost particles that have low intensity. According to track length statistics from Davis 8.4, the difference between the overall number of tracks and continued tracks in 2000 time steps at threshold of 150 or 250 is roughly less than 40 tracks while the difference is around 400 tracks at threshold of 50. In addition, overlapping particles in the Shake-the-Box algorithm is more difficult when the number of particles is high. Figure B.2 shows the effect of values of threshold on Reynolds stresses. A large increase in noise level is observed in wall-normal and spanwise Reynolds stresses at threshold of 50 while difference between threshold of 150 and 250 is small.

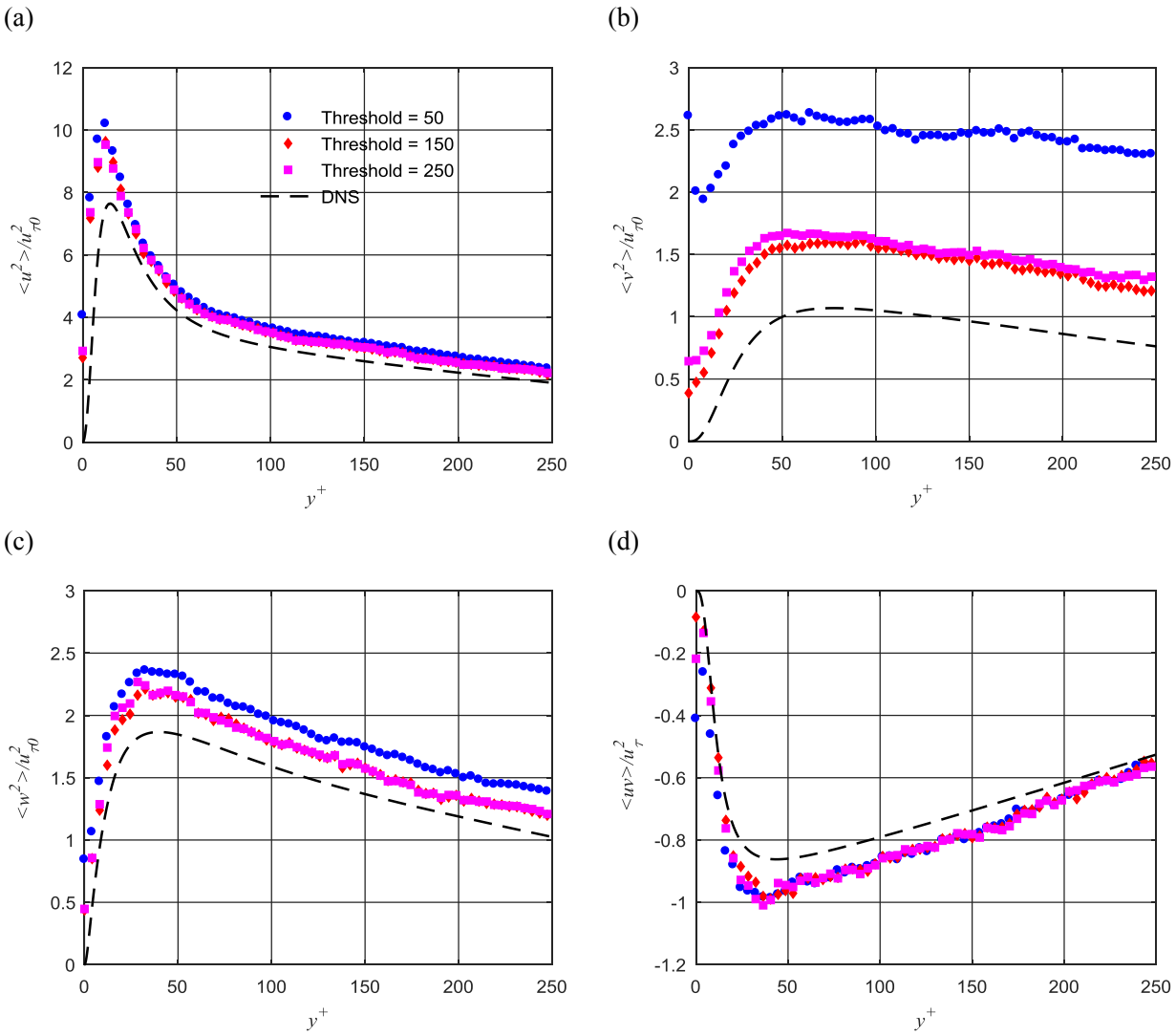

Figure B.2. Effect of threshold based on adjusted settings, (a) streamwise Reynolds stress, (b) wall-normal Reynolds stress, (c) spanwise Reynolds stress, (d) Reynolds shear stress.

B.3 Effect of the length of the polynomial track fit (LPTF)

In order to improve accuracy and allow extracting local velocity and acceleration from the tracks, second order polynomial fit is applied. The purpose of this section is to study the effect of the length of the second order of polynomial track fit on reducing the noise during calculating velocity. Figure B.3 shows the effect of LPTF at different threshold on Reynolds stresses. The results show that noise decreases with increasing LPTF and this effect is more apparent in threshold of 250.

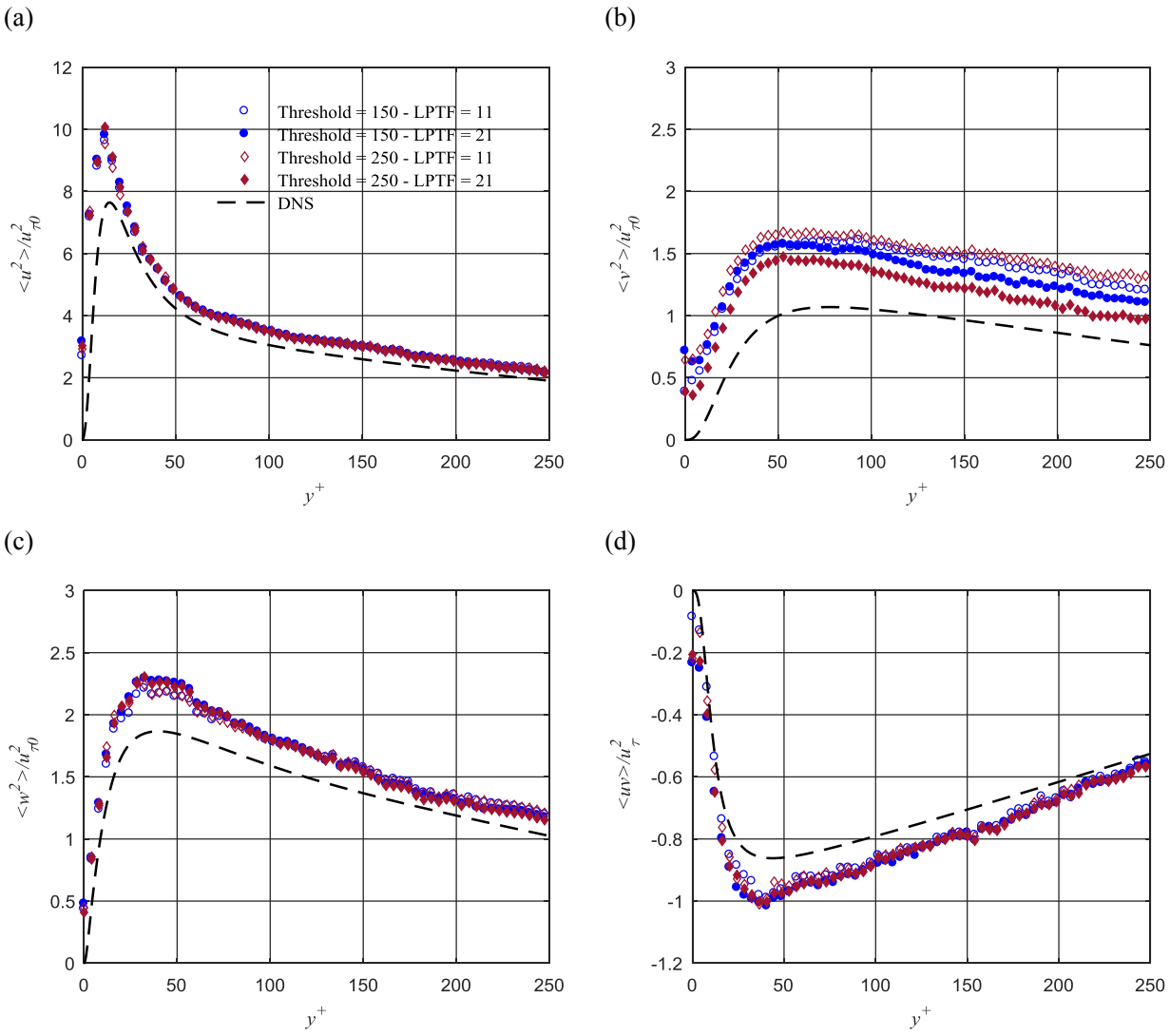

Figure B.3. Effect of the length of the polynomial track fit (LPTF) based on adjusted settings, (a) streamwise Reynolds stress, (b) wall-normal Reynolds stress, (c) spanwise Reynolds stress, (d) Reynolds shear stress.

The effect of LPTF on the instantaneous streamwise velocity at threshold of 250 for 25 tracks is shown in Figure B.4. Although large noise reduction is achieved in wall-normal Reynolds stress, the obvious drawback of using polynomial track fit is that each track starts and ends with tail, which roughly has the length of the polynomial track fit. Figure B.5 shows that LPTF is not applied on the positions.

(a) (b)

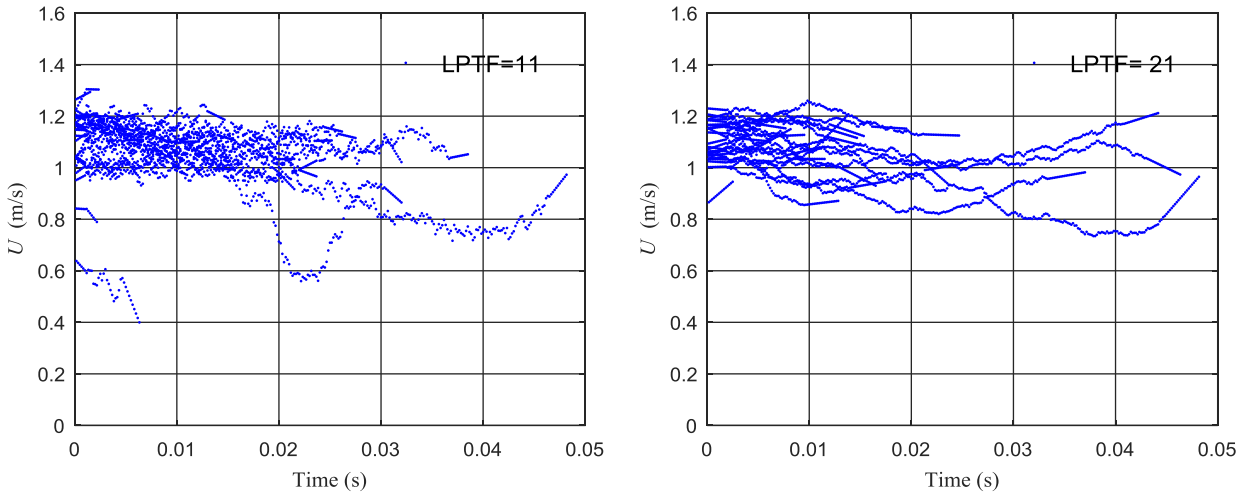

Figure B.4. Effect of the length of the polynomial track fit (LPTF) on instantaneous streamwise velocity based on adjusted settings for 25 tracks (a) LPTF =11, (b) LPTF =21.

(a) (b)

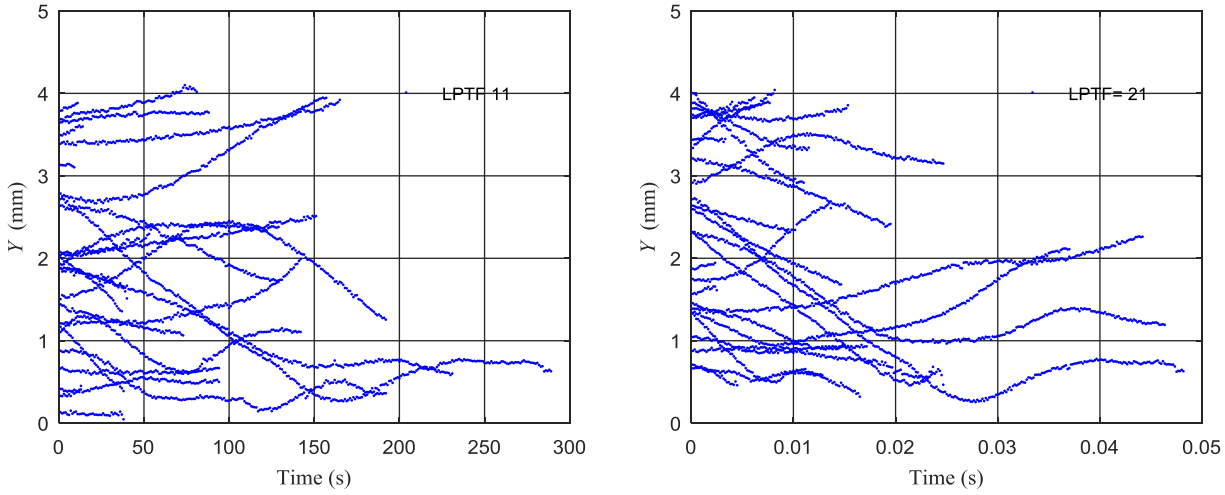

Figure B.5. Effect of the length of the polynomial track fit (LPTF) on wall-normal particle locations on a track based on adjusted settings for 25 tracks (a) LPTF =11, (b) LPTF =21.

B.4 Effect of maximum absolute change in particle shift (MACPS)

To ensure smooth acceleration along the trajectory, this parameter can be used to specify the maximum change from time-step to time-step in voxel (consecutive time-steps). Figure B.6 shows the effect of changing maximum absolute change in particle shift (MACPS) on Reynolds stresses. MACPS with 2 vox shows a small improvement in viscous sublayer and buffer layer in streamwise and spanwise Reynolds stresses and this improvement is more pronounced in wall normal Reynolds stress.

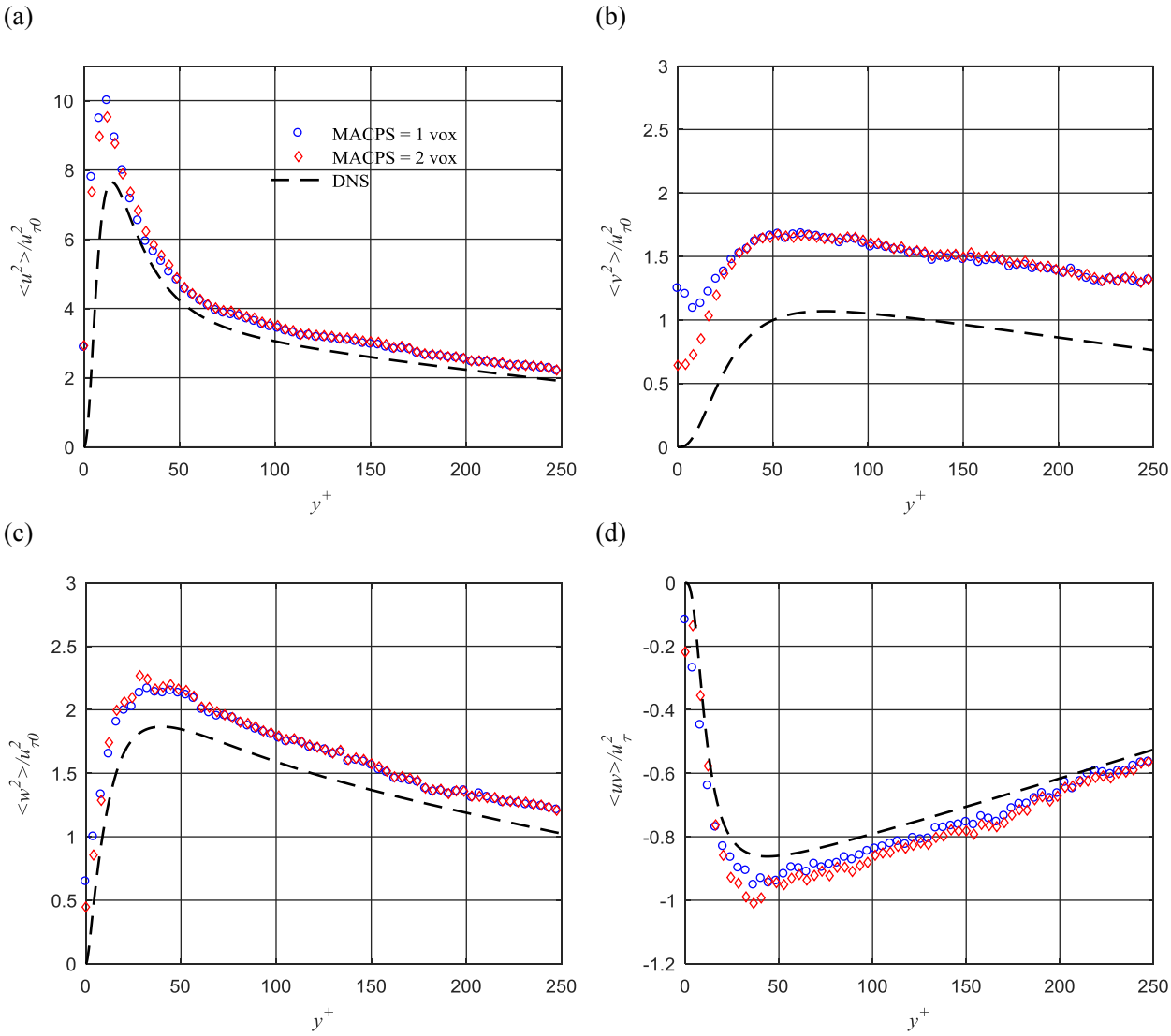

Figure B.6. Effect of maximum absolute change in particle shift (MACPS) based on adjusted settings, (a) streamwise Reynolds stress, (b) wall-normal Reynolds stress, (c) spanwise Reynolds stress, (d) Reynolds shear stress.

B.5 Effect of shake particle position (SPP)

This parameter is used to shake the particle within a certain distance (moving the particle in small distance around the volume) in order to obtain the optimal position. As a result, the reprojection errors are reduced. Figure B.7 shows the comparison between two different SPP values. The results show a slight reduction in spanwise Reynolds stress and Reynolds shear stress near the wall with shake particle position of 0.1. A small increase in streamwise Reynolds stress in buffer layer is noted. Using smaller value of SSP requires an increase in the number of iterations, and therefore needs more time to process.

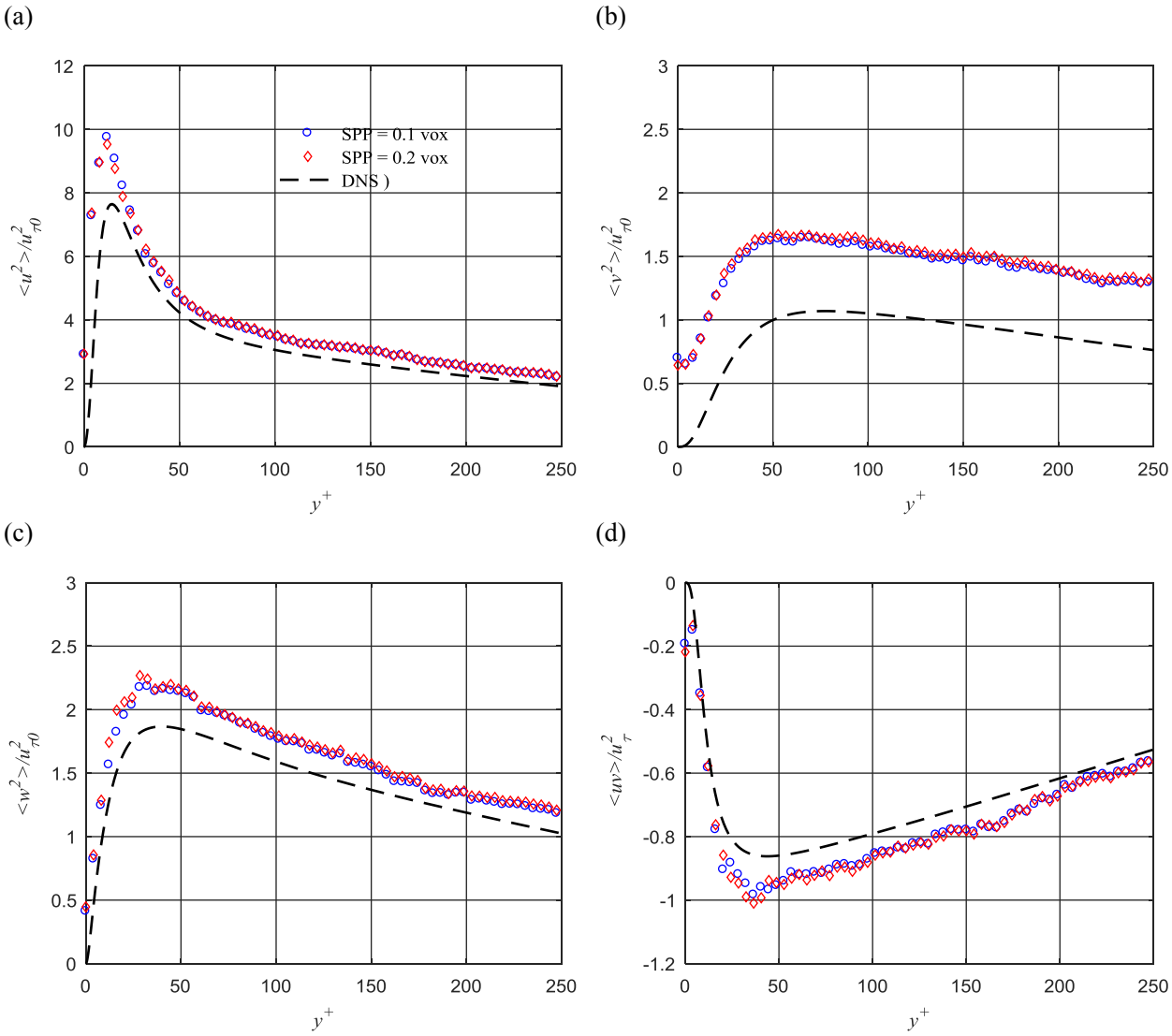

Figure B.7. Effect of shake particle position (SSP) based on adjusted settings, (a) streamwise Reynolds stress, (b) wall-normal Reynolds stress, (c) spanwise Reynolds stress, (d) Reynolds shear stress.

B.6 Effect of sharpening

The influence of image noise can be reduced with appropriate pre-processing. Sharpening filter is recommended to use with Gaussian smoothing to decrease the effective particle size. Therefore, it reduces noise (Manual for DaVis 8.3. 2016).This investigation was at intensity threshold of 250. The noise reduction is observed in wall normal stress as shown in Figure B.8 (b). However, data is not smooth which is more obvious in Reynolds shear stress shown in Figure B.8 (d).

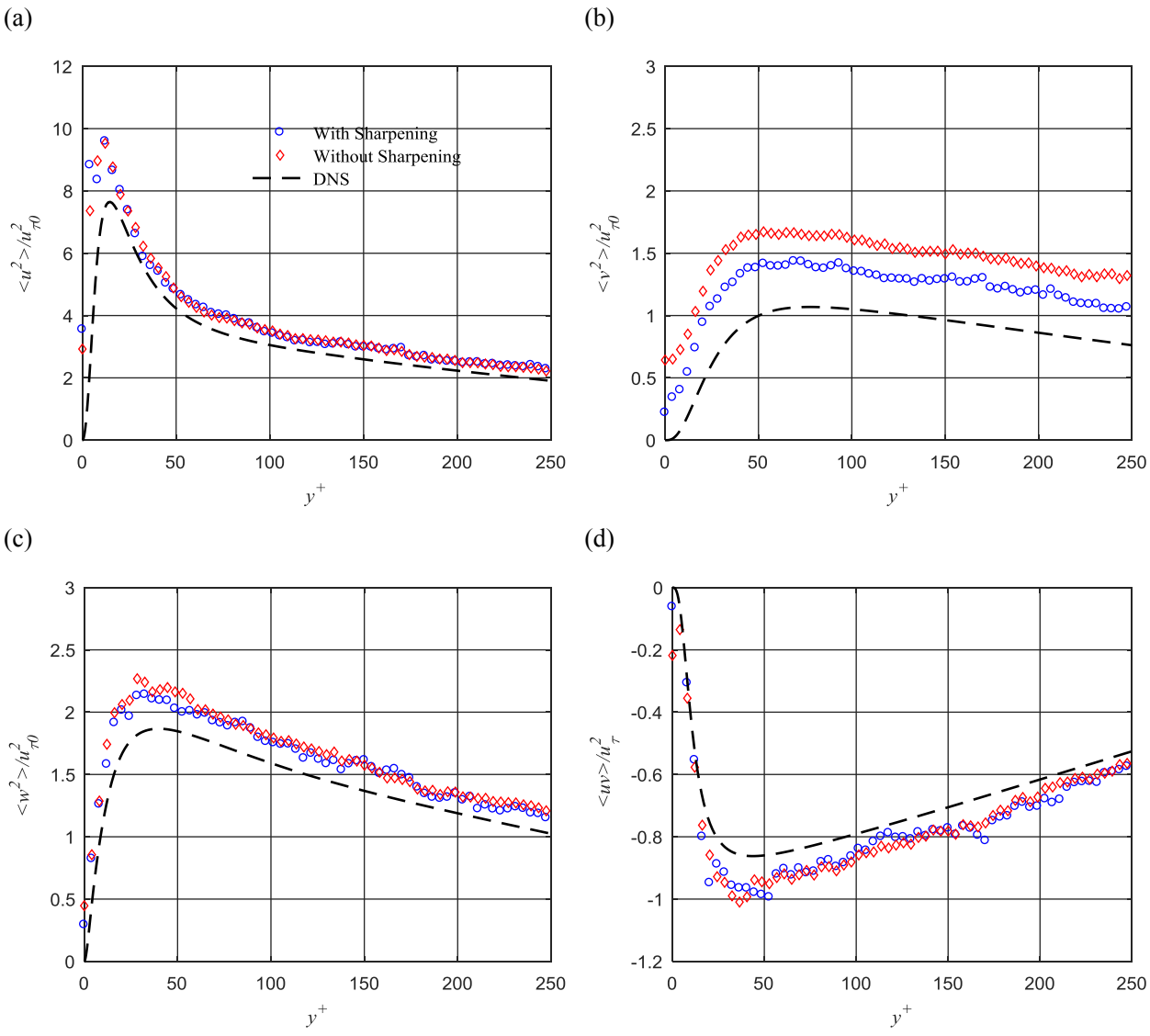

Figure B.8. Effect of Sharpening, (a) streamwise Reynolds stress, (b) wall-normal Reynolds stress, (c) spanwise Reynolds stress, (d) Reynolds shear stress.

B.7 Effect of regression

In order to remove tails are associated with length of polynomial track fit (LPTF) and suppress measurement noise , the quadratic regression filter is carried out in MATLAB This quadratic regression filter is applied on particles locations along a track then instantaneous velocity is extracted as the first derivative. The quadratic regression filter is also applied to instantaneous velocities. Figure B.9 shows a comparison between polynomial track fit (LPTF) with length of 21 and quadratic regression filter with kernal size of 21 (over a period of 3.49 ms) at threshold of 250 for 25 tracks.

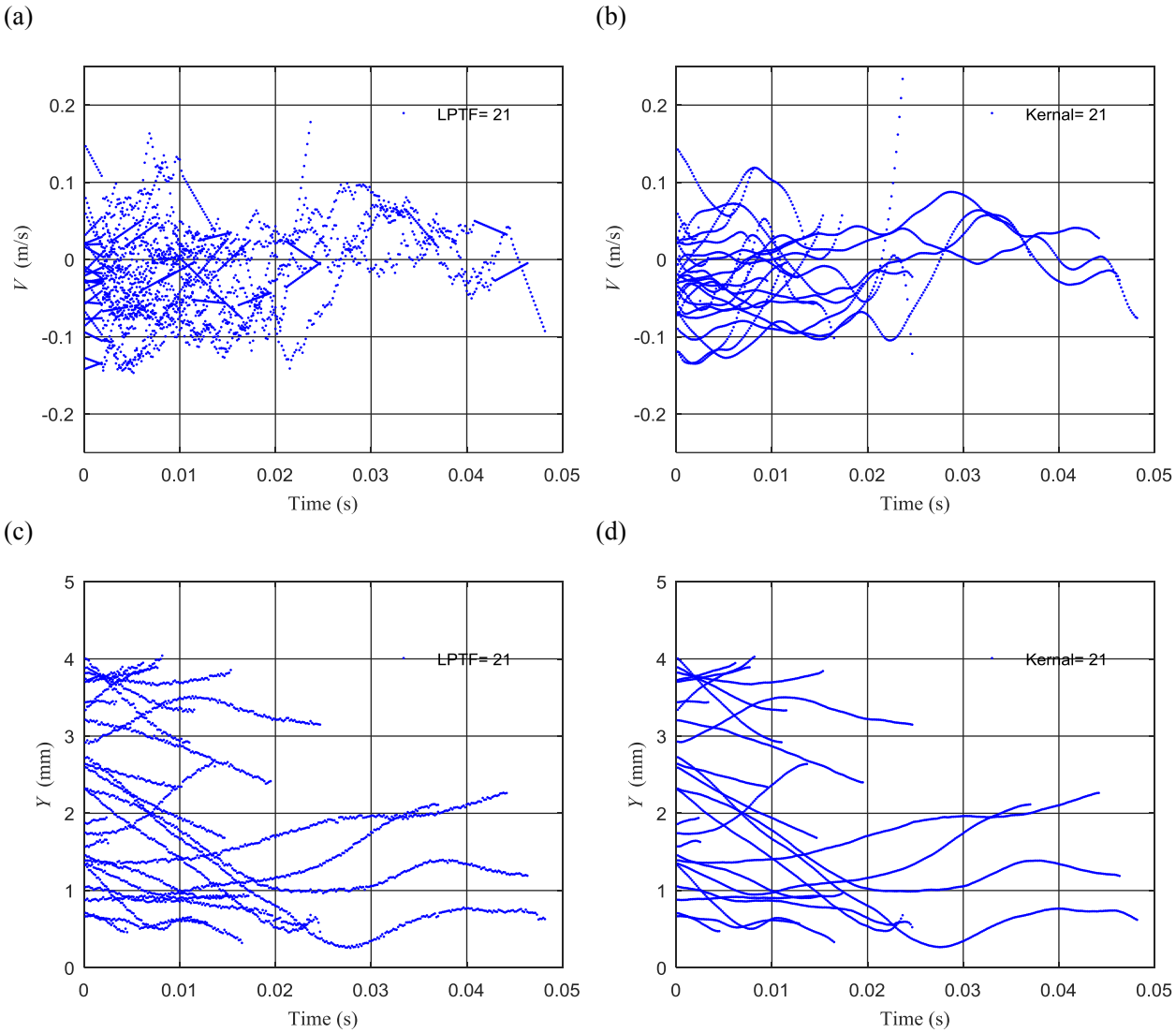

Figure B.9. Comparison between polynomial track fit (LPTF) and quadratic regression filter at threshold of 250 for 25 tracks based on adjusted settings, (a,b) instantaneous wall-normal velocity (c,d) wall-normal particle location.

It is obvious that using quadratic regression filter reduces noise associated with location and velocity. In addition, straight tails at beginning and ending of each track in instantaneous velocity are not created with using quadratic regression filter. Figure B.10 shows the effect of the quadratic regression filter with different kernel size on Reynolds stresses. Large reduction in wall-normal stress is noted. This reduction increases with increasing kernel size. A decrease in streamwise and spanwise stresses and Reynolds stress is also observed.

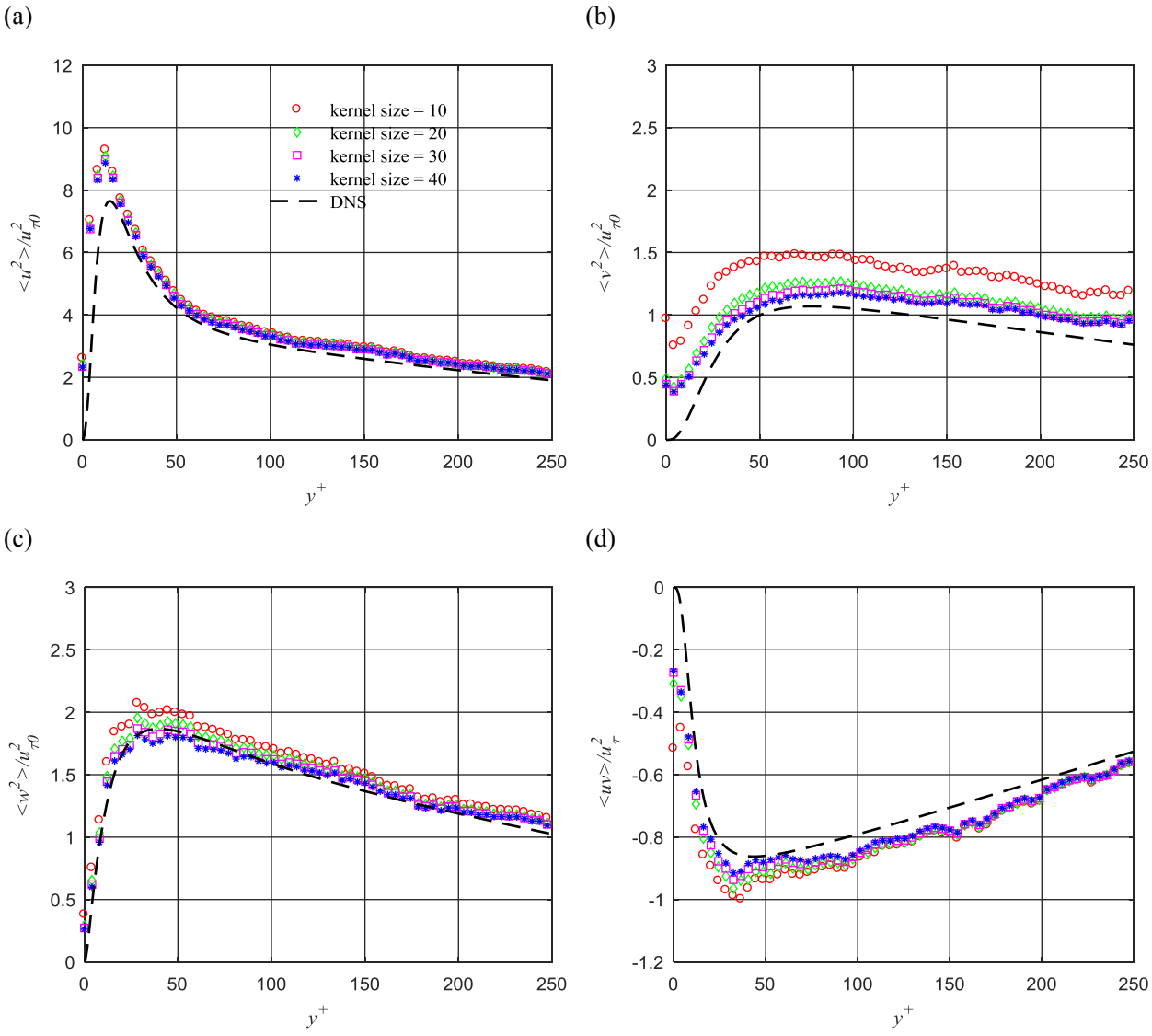

Figure B.10. Effect of quadratic regression filter with different kernel size based on adjusted settings at threshold of 250, (a) streamwise Reynolds stress, (b) wall-normal Reynolds stress, (c) spanwise Reynolds stress, (d) Reynolds shear stress.

B.8 Effect of removing short tracks

Removing short tracks is a significant step in processing shake the box data. As discussed in section B.2 that the number of short tracks is strongly associated with intensity threshold. In this section, the investigation is based on threshold of 250. Short tracks can be originated from two reasons. Particle can be lost when it has very weak intensity. The second reason, noise peaks might be considered as a new particles which made up short false tracks or particle matching is difficult because of many new particles especially at low threshold. In addition, the corrected particle position prediction in a future time-step is more difficult when track is short.

Although shake the box method nearly completely solved the ghost particle problem (Schanz *et al.,* 2014). The effect of tracking of ghost particles can be effectively avoided by removing short particle tracks. The effect of removing tracks with length below 30 time steps on Reynolds stresses is shown in Figure B.11. The noise reduction is associated with short tracks is about 8 % and 2.7% in wall normal Reynolds stress and spanwise Reynolds at y^+=50, respectively.

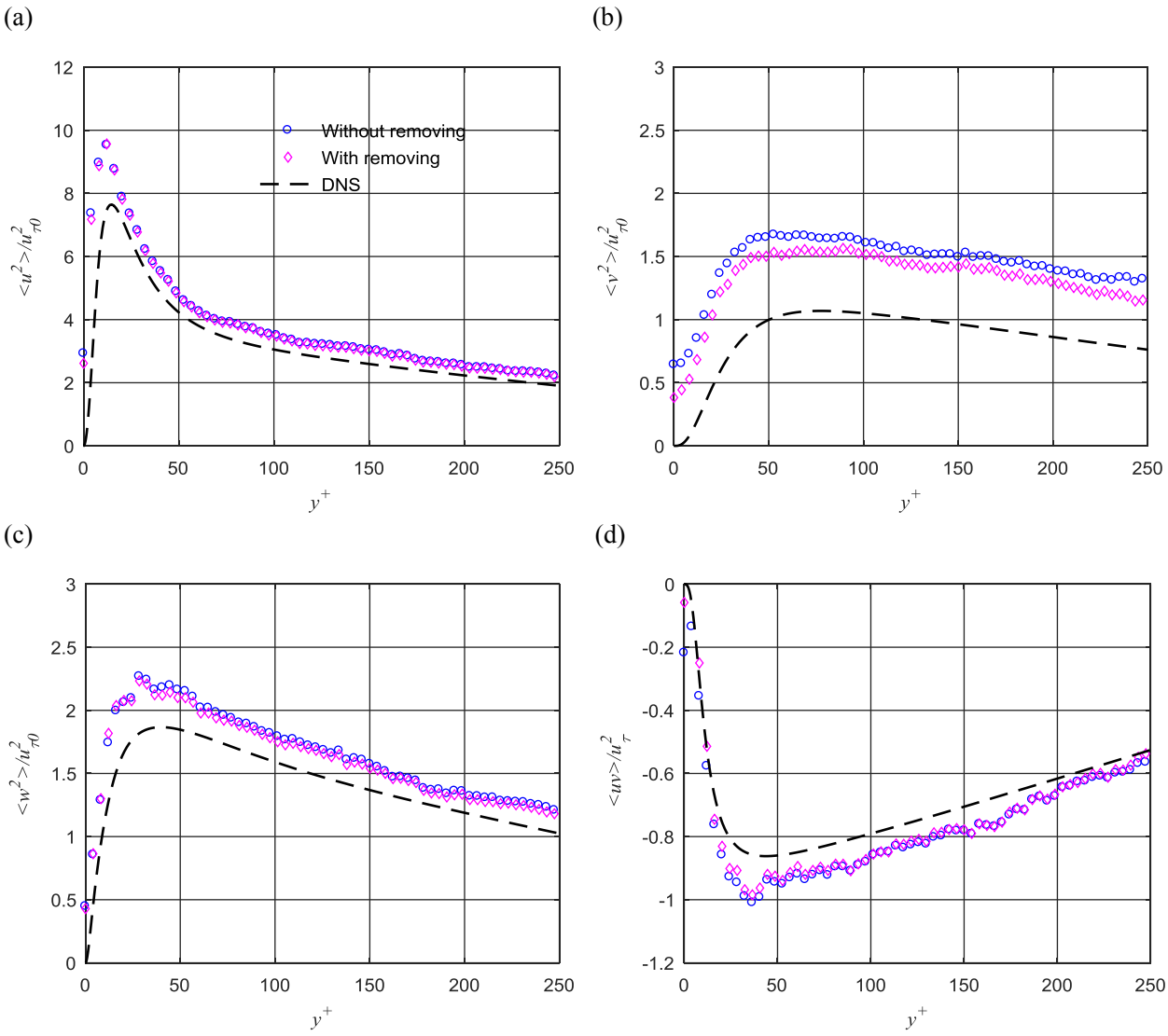

Figure B.11. Effect of removing short tracks with length below 30 time step based on adjusted settings at threshold of 250 , (a) streamwise Reynolds stress, (b) wall-normal Reynolds stress, (c) spanwise Reynolds stress, (d) Reynolds shear stress.

B.9 Comparison between optimum, default and adjusted settings

This section includes the best steps and optimum parameters for processing shake the box data. The next Table presents optimum parameters values obtained in advanced settings using Davis 8.4. The image preprocessing is applied with Gaussian smoothing filter (3×3 pix) and without sharpening filter. The quadratic regression filter with kernel size of 30 (over a period of 5 ms) is applied on particles positions (*x,y* and *z*) and instantaneous velocities using Matlab. The threshold is set at 250. The order and length of polynomial track fit are not important because velocities are extracted as the first derivative (location and time-step) and they are not applied

on particles location along *x*, *y* and *z* on a track. However, it is recommended to use the highest number of length of polynomial track fit which is 301 in Davis 8.4 and second order polynomial track fit in order to reduce processing time. Figure B.12 shows the comparison of using optimum, default and adjusted settings. The results show 60 % reduction in wall-normal stress compared with default settings. About 20 % of reduction in spanwise Reynolds stress and Reynolds shear stress. A slight decrease (9%) in streamwise Reynolds stress is also observed.

Table B. 3. Optimum settings

Shaking	
Adding particles (outerloop)	5 iterations
Refine particle position and intensity (inner loop)	6 iterations
Shake particle position by	0.2 voxel
Remove particles if closer than	2 voxel
Remove weak particles if intensity <	0.8 of average particle intensity
Particle image shape and intensity	
Make OTF smaller	1.8 times
Residuum computation: increase particle intensity	1.8 times
Residuum computation: OTF radius	±5 pixel
Tracking: acceleration limits	
Maximum absolute change in particle shift	2 voxel
Maximum relative change in particle shift	50 %
Order for polynomial track fit	2
Length for polynomial track fit	301

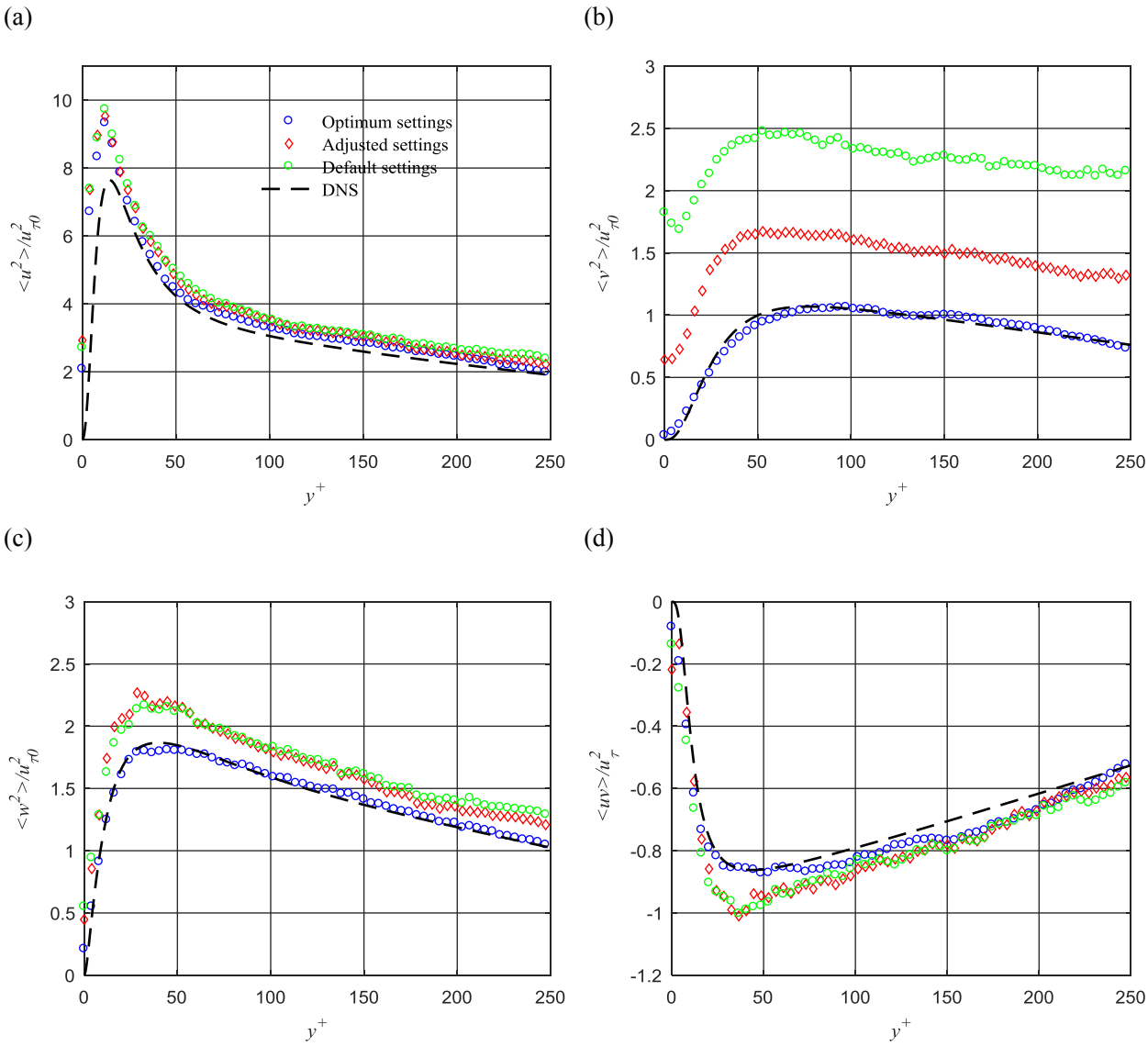

Figure B.12. Comparison of effect of optimum, default and adjusted settings at threshold of 250, (a) streamwise Reynolds stress, (b) wall-normal Reynolds stress, (c) spanwise Reynolds stress, (d) Reynolds shear stress.